

**ORBITAL ANGULAR MOMENTUM IN OPTICAL  
FIBERS**

*NENAD BOŽINOVIĆ*

Dissertation submitted in partial fulfillment  
of the requirements for the degree of  
Doctor of Philosophy

**BOSTON  
UNIVERSITY**



BOSTON UNIVERSITY  
COLLEGE OF ENGINEERING

Dissertation

**ORBITAL ANGULAR MOMENTUM IN OPTICAL  
FIBERS**

by

**NENAD BOŽINOVIC**

B.Sc., Belgrade University, 2004  
M.Sc., Boston University, 2008

Submitted in partial fulfillment of the  
requirements for the degree of  
Doctor of Philosophy

2013

© Copyright by  
Nenad Božinović  
2013

Approved by

First Reader

---

Siddharth Ramachandran, Ph.D.  
Professor of Electrical and Computer Engineering, Boston University

Second Reader

---

Steven Golowich, Ph.D.  
Member of Technical Staff, MIT Lincoln Laboratory

Third Reader

---

Luca Dal Negro, Ph.D.  
Associate Professor of Electrical and Computer Engineering,  
Boston University

Fourth Reader

---

Selim M. Ünlü, Ph.D.  
Professor of Electrical and Computer Engineering, Boston University

*I hear babies cryin' ... I watch them grow  
They'll learn much more ... than I'll ever know  
And I think to myself ... what a wonderful world.*

from a song "What a Wonderful World", written by Bob Thiele and George David Weiss, performed by Louis Armstrong

## Acknowledgments

My graduate school journey would never be possible without the help of so many people around me. First and foremost, I would like to thank my advisor, Professor Siddharth Ramachandran, for excellent guidance and amazing research opportunities throughout the years of my research. From day one when I started working with fibers in the lab, through times when we would fight experimental obstacles together while time zones apart, I felt privileged and truly grateful for the opportunity to be a part of his group.

I want to specially thank my collaborator and committee member Dr. Steven Golowich for all the insightful discussions and collaborative work that have greatly helped my research. I also owe a great deal of my gratitude to my master thesis advisor, Professor Jerome Mertz, for his support during my research in his lab, where I acquired skills that tremendously helped me throughout the later years in the grad school. I also want to thank my committee members Professor Luca Dal Negro and Professor Selim Ünlü for their academic support throughout the years at Boston University.

I want to give my special thanks to my friend and colleague Paul Steinurzel for his wisdom, constructive criticism, best jokes ever and all the good times, especially in the lonely hours late in the lab. Also special thanks to Pat Gregg for being the best brainstomper buddy and for all the memorable long walks back home together to Cambridge. I want to thank all of my friends and coworkers: Faisal, Khwanchai, Masao, Habibe, Michael, Jeff, Boyin, Yuhao, Lu, Debangshu, Damian, Lars, Roman, Chris, Ken, Daryl, Tim, Kyle, Erwin, Aymeric and Cathie who made all these years in grad school extremely fun and enjoyable that I'll cherish for the rest of my life.

I want to thank my collaborators: Poul Kristensen, Martin Pedersen, Misha Brodsky, Yang Yue, Yongxiong Ren, Moshe Tur, Alan Willner, Martin Lavery, Miles Pad-

dget, Nick Fontaine, Rene Essiambre, Ee Leong Lim and David Richardson, that I had pleasure to work with.

I was extremely lucky that I have shared the enjoyments of my life here in Boston, and around the world, with many of my loving friends: Vedran, Tamara, Nebojša, Jenny, Dino, Slobo, Dejan, Ado, Adnan, Anis, Milan, Vladimir, Maxim, Ye, Phil, Doug, Ajay, Gilberto, Giovanni, Rade S., Rade N. and many many many more.

I want to thank my idols for the inspiration and vision that gave me the strength to meet the demands of a grad school life.

Most of all, I want to thank my whole family in Serbia and all over the world, my relatives, my brother Nikola, my mom Olivera and my dad Dušan for their unconditional support and love.

# **ORBITAL ANGULAR MOMENTUM IN OPTICAL FIBERS**

(Order No. )

**NENAD BOŽINOVIC**

Boston University, College of Engineering, 2013

Major Professor: Siddharth Ramachandran, PhD,  
Professor of Electrical and Computer Engineering

## **ABSTRACT**

Internet data traffic capacity is rapidly reaching limits imposed by nonlinear effects of single mode fibers currently used in optical communications. Having almost exhausted available degrees of freedom to orthogonally multiplex data in optical fibers, researchers are now exploring the possibility of using the spatial dimension of fibers, via multicore and multimode fibers, to address the forthcoming capacity crunch. While multicore fibers require complex manufacturing, conventional multimode fibers suffer from mode coupling, caused by random perturbations in fibers and modal (de)multiplexers. Methods that have been developed to address the problem of mode coupling so far, have been dependent on computationally intensive digital signal processing algorithms using adaptive optics feedback or complex multiple-input multiple-output algorithms.

Here we study the possibility of using the orbital angular momentum (OAM), or helicity, of light, as a means of increasing capacity of future optical fiber communication links. We first introduce a class of specialty fibers designed to minimize mode coupling and show their potential for OAM mode generation in fibers using numer-

ical analysis. We then experimentally confirm the existence of OAM states in these fibers using methods based on fiber gratings and spatial light modulators. In order to quantify the purity of created OAM states, we developed two methods based on mode-image analysis, showing purity of OAM states to be 90% after 1km in these fibers. Finally, in order to demonstrate data transmission using OAM states, we developed a 4-mode multiplexing and demultiplexing systems based on free-space optics and spatial light modulators. Using simple coherent detection methods, we successfully transmit data at 400Gbit/s using four OAM modes at a single wavelength, over 1.1 km of fiber. Furthermore, we achieve data transmission at 1.6Tbit/s using 10 wavelengths and two OAM modes.

Our study indicates that OAM light can exist, and be long lived, in a special class of fibers and our data transmission demonstrations show that OAM could be considered an additional degree of freedom for data multiplexing in future optical fiber communication links. Our studies open the doors for other applications such as micro-endoscopy and nanoscale imaging which require fiber based remote delivery of OAM light.

# Contents

<b>1</b>	<b>Introduction</b>	<b>1</b>
1.1	Optical fiber communications and space-division multiplexing . . . . .	1
1.2	Orbital angular momentum (OAM) of light . . . . .	6
<b>2</b>	<b>Multimode Fibers and Mode Stability</b>	<b>10</b>
2.1	Optical fiber waveguide theory . . . . .	10
2.2	OAM fiber modes . . . . .	17
2.3	Fiber mode coupling theory . . . . .	21
<b>3</b>	<b>Vortex Fiber</b>	<b>26</b>
3.1	Introduction . . . . .	27
3.2	Numerical analysis . . . . .	28
3.3	Experimental measurements . . . . .	32
3.3.1	Effective and group indices . . . . .	33
3.3.2	Loss . . . . .	34
3.3.3	Mode imaging . . . . .	35
<b>4</b>	<b>OAM Generation in Vortex Fiber</b>	<b>39</b>
4.1	Fiber Gratings . . . . .	40
4.1.1	Long period grating theory . . . . .	41
4.1.2	Microbend gratings . . . . .	42
4.1.3	$CO_2$ laser induced gratings . . . . .	46
4.1.4	Role of tapers in improving mode conversion . . . . .	50
4.1.5	Group index difference calculation . . . . .	52

4.2	Spatial light modulator approach . . . . .	53
<b>5</b>	<b>OAM Purity Measurements</b>	<b>59</b>
5.1	Ring technique . . . . .	59
5.2	Cutback measurements . . . . .	68
5.3	Regression analysis . . . . .	70
<b>6</b>	<b>OAM Mode-Division-Multiplexing (MDM)</b>	<b>73</b>
6.1	Multiplexing 4-mode system . . . . .	74
6.2	Demultiplexing and imaging . . . . .	76
6.3	Cross-talk and multi-path-interference . . . . .	76
6.4	Alignment procedure for 4-mode setup . . . . .	78
<b>7</b>	<b>OAM Transmission</b>	<b>82</b>
7.1	Brief introduction in communication systems . . . . .	82
7.2	4-mode OAM-MDM . . . . .	87
7.3	2-mode OAM-MDM . . . . .	90
<b>8</b>	<b>Conclusion</b>	<b>95</b>
8.1	Observations . . . . .	96
<b>Appendix</b>		<b>101</b>
A1	Polarization dependence of components . . . . .	101
A2	Transmission of OAM-entangled photons . . . . .	104
A3	Publication list . . . . .	106
<b>References</b>		<b>108</b>
<b>Curriculum Vitae</b>		<b>119</b>

# List of Figures

1.1 (A) North American Internet traffic in Petabytes/month according to several studies, such as Minnesota Internet Traffic Study (MINTS) and Cisco. (Essiambre and Tkach, 2012). (B) Capacity evolution for different communication systems (Sakaguchi et al., 2012). With permission from (Essiambre and Tkach, 2012) and (Sakaguchi et al., 2012), © IEEE.	2
1.2 (A) Simulated results for spectral efficiency vs signal-to-noise ratio using additive-white-Gaussian noise without dispersion compensation. (B) Current state-of-the-art in single-mode fiber transmission (Essiambre and Tkach, 2012). With permission from (Essiambre and Tkach, 2012), © IEEE.	3
1.3 Different types of fibers considered for future communication links in order to increase network capacity (Essiambre and Tkach, 2012). With permission from (Essiambre and Tkach, 2012), © IEEE.	4
1.4 (A) Illustration of a doughnut shaped intensity of Laguerre Gaussian $l = 1$ beam ( $LG_{10}$ ). Due to phase singularity in the center of the beam, OAM beams are also called vortex beams. (B) Circularly polarized $LG_{00}$ beam, that carry spin angular momentum (SAM), can rotate an object upon illumination. (C) Similarly to SAM, an $LG_{10}$ beam can transfer orbital angular momentum (OAM) and rotate an object, potentially at much higher rates. With permission from Wikipedia, © Creative Commons.	7

1.5	Example of conversion between fundamental Laguerre Gaussian ( $LG_{0m}$ ) and higher order ( $LG_{1m}$ ) beam using a spiral phase plate with a phase step equal to $d = 2\pi l \lambda \approx 10\mu m$ (for $l = 1$ and $\lambda = 1550nm$ ). With permission from Wikipedia, © Creative Commons. . . . .	8
1.6	(A) In this dissertation we study the idea of OAM as a new, orthogonal, degree of freedom in addition to wavelength, phase, amplitude and polarization, for multiplexing in the future optical communication systems. (B) OAM mode division multiplexing in fibers concept. . .	9
2.1	Numerical solutions for effective index, $n_{eff}$ , for step index fiber, showing labeling and corresponding values of $l$ and $m$ . . . . .	16
2.2	First six modes ( $l = 0$ and $l = 1$ groups) in a step index fiber. . . . .	16
2.3	Intensity patterns of the first-order mode group in vortex fiber. Arrows show the polarization of the electric field. The top row shows vector modes that are the exact vector solutions of the Eq. 2.18, while the bottom row shows the resultant, unstable $LP_{11}$ modes commonly obtained at a fiber output. Specific linear combinations of pairs of top row of modes, resulting in the variety of $LP_{11}$ modes obtained at a fiber output, are shown by colored lines (Ramachandran et al., 2009). With permission from (Ramachandran et al., 2009). © OSA. . . . .	23
2.4	Concept of effective index separation in the first-order modes (A) Typical step-index MMF does not exhibit effective index separation causing mode coupling. (B) $n_{eff}$ separation caused by desired fiber index profile. . . . .	24
3.1	(A) An optical microscope image of the end facet of the vortex fiber dk11OD100. (B) Measured fiber refractive index for the dk11OD100 and dk11OD160. . . . .	28

3.2	Comparison of the simulated fields using scalar and vector numerical method for the dk11OD105 fiber case. . . . .	29
3.3	Numerically calculated properties of the dk11OD105 vortex fiber. Separation of $n_{eff}$ indicates potential for smaller mode coupling (A-B). Mode profiles in 1D and 2D case (C-D), latter obtained from the 1D profiles assuming circular symmetry. Polarization at certain points can be also obtained assuming azimuthal dependence of the modes (Table 2.3). . . . .	30
3.4	(A) Effective indices for guided modes for the dk11OD160 vortex fiber. (B) Corresponding LP notation designating certain groups of modes.	31
3.5	Effective index difference (also called mode separation) versus fiber OD between different modes. . . . .	32
3.6	Table of guided modes for different OD fibers, at 1550nm. OD105 offers largest diameter fiber for which $l \geq 2$ modes are cuts off. . . .	32
3.7	Numerically calculated properties of the dk11OD105 vortex fiber . . .	33
3.8	Measured and numerically calculated $\Delta n_{eff}$ with respect to the $HE_{11}$ mode for (A) OD100, (B) OD110 and (C) OD115 vortex fibers. . . .	33
3.9	Group index difference among $HE_{11}$ and $HE_{21}$ vortex fiber modes for several different OD. . . . .	34
3.10	Transmission power difference (in dB) between $HE_{21}$ and $HE_{11}$ modes showing linear dependence of the loss in length. Gradient of the fit 0.33 dB/km gives the excess (i.e. differential) loss between the two modes.	35
3.11	Setup for OAM mode imaging. This setup enables us to measure both the intensity and the phase of the beam. . . . .	36

3.12 (A) OAM mode intensity profile and (B) a line profile along the ring. (C,D) Observed interference patterns between the OAM mode and the reference beam when the two beams are (C) collinear or (D) form an angle . (E,F) Simulated interference patterns in the two cases. . .	37
3.13 Comparison of the simulated and imaged mode profiles for OD100 case. . . . .	38
4.1 Microbend gratings. (A) Mode conversion setup. (B) Picture of the microbend grating. (C) Effective indices of modes supported by the vortex fiber (also see 3.8). Microbend grating period can be tuned to allow for mode conversion from $HE_{11}$ to first-order modes (denoted by arrows). . . . .	43
4.2 Microbend resonance characteristic with respect to input polarization, grating length and fiber roll angle. (A) Polarization dependence. (B) $HE_{21}$ resonances for different grating lengths. Longer grating length require less pressure per fiber length, hence, pressure induced splitting is smaller. Note grating bandwidth change with length, in agreement with the theory. (C) Microbend pressure for $HE_{21}^{odd}$ and $HE_{21}^{even}$ reso- nances vs fiber roll angle (i.e. rotation axis is along the fiber). . . .	45
4.3 $CO_2$ laser induced gratings. (A) Setup. Laser beam is focused onto the fiber and point-to-point grating is written onto the vortex fiber. (B) Setup photo (blue line indicates beam path, red line indicates vortex fiber). (C) Microscope image of the grating inscribed in the fiber, indicating periodic mechanical changes. (D) Polarization dependence of the $CO_2$ gratings. In comparison to microbend gratings (Fig. 4.2), $CO_2$ gratings are less polarization sensitive. . . . .	47

4.4 (A) Tension and fiber width profile for a 5-5-5 $\mu$ m taper geometry with 40 $\mu$ m waist. (B) Resonance for dk11OD100 fiber in the case of a taper shown in A. . . . .	51
4.5 Loss transmission spectrum for $HE_{11}$ and $HE_{21}$ phase matched case. Fitting the curve with the expected $sinc^2$ profile gives the group index difference $\Delta n_g$ . . . . .	53
4.6 Phase matching curves $\Lambda(\lambda)$ relate grating period $\Lambda$ with resonant wavelength (particular example is for the case of dk110127OD100 fiber). Respective $\Delta n_{eff}$ and $\Delta n_g$ can be calculated (bottom two graphs). . . . .	54
4.7 (A) SLM mode conversion concept. After reflection off a SLM, an OAM beam is created. (B) The spiral SLM pattern that creates the $LG_{10}$ beam at the same reflection angle as the $LG_{00}$ beam incident angle. (C) The fork SLM pattern that creates the $LG_{10}$ beam at the different reflection angle from the $LG_{00}$ beam incident angle. . . . .	55
4.8 Spatial light modulator based mode conversion. (A) Setup. (B) Photo of the setup. . . . .	56
4.9 Spiral and fork holograms that create $LG_{10}^*$ , showing the effect of tilt in the case of the fork hologram. . . . .	56
4.10 Back-reflection from the mirror installed instead of the fiber for three different axial positions of the coupling stage for a beam free of aberrations: (A,C) defocused $LG_{00}$ (B) focused $LG_{00}$ (D,F) defocused $LG_{10}$ (OAM mode)(E) focused $LG_{10}$ . Symmetric pattern, indicates good alignment between input beam and the fiber. . . . .	57

4.11 Camera image at the CamPos1 for the vortex fiber installed. Donut mode represents back reflection from the fiber end-face (similar to the case of the mirror in the Fig. 4.10). $HE_{11}$ mode represents light coming out of the vortex fiber, when the other fiber end is connected to the light source. Two images here are intentionally misaligned. . . . .	57
4.12 Output of the vortex fiber after OAM mode coupling. <b>(A)</b> Aligned and <b>(B)</b> misaligned case. . . . .	58
5.1 Setup for imaging vortex fiber output. <b>(A)</b> Experimental setup that uses grating for OAM mode generation. <b>(B)</b> Grating resonance spectrum used to deduce $HE_{21}^o$ mode conversion level. <b>(C)</b> Camera image of the four polarization projections of the fiber output. Acronyms: left circular (LC), right circular (RC), vertical (V) and horizontal (H), non-polarizing beam splitter (NPBS), quarter wave plate (QWP), polarizing beam displacing prism (PBDP). Vertical (V) polarization projection was interfered with the reference beam (Ref.) in order to observe the phase of the vortex beam. Showed is the $l = +1$ OAM state that is circularly polarized (spin = 1). . . . .	60
5.2 Camera images for the three positions of the polcon2 paddles, tuned to achieve <b>(A)</b> $l = 1$ , <b>(B)</b> $l = 0$ and <b>(C)</b> $l = -1$ state. . . . .	62
5.3 Ring method analysis for determining modal content of the vortex fiber. <b>(A)</b> Azimuthal intensity profile of LC projection for radius r0. <b>(B)</b> Fourier series coefficients for profile in (A). <b>(C)</b> Extracted modal power contributions. . . . .	64

5.4 Ring method analysis applied in real time. <b>(A)</b> Mode powers in time during continuous adjustment of the paddles of PolCon2 (on the vortex fiber) to obtain desired OAM state superposition. <b>(B)</b> Camera images of the three positions (a-c) . . . . .	66
5.5 Ring method error estimation. <b>(A)</b> Random simulated image created as an weighted average of the six modes $V_{21}^{+,-}$ $V_T^{+,-}$ and $V_{11}^{+,-}$ with randomized phases (dark and shot noise were also accounted for). <b>(B-D)</b> Estimated modal power error with respect to different initial modal powers for (B) $V_{21}^+$ , (C) $V_T^+$ and (D) $V_{11}^+$ modes. We see that errors on average increase as input powers of spurious modes increase, indicating that the assumed 'dominant mode model' is no longer valid. For this reason calculations were only done for powers $< -5dB$ with respect to total power. . . . .	67
5.6 <b>(A)</b> Concept of higher-order Poincaré sphere (taken with permission from (Milione et al., 2011)). <b>(B)</b> Reconstruction of a relative phase between two OAM states for the same case of tuning OAM shown in Fig. 5.4. . . . .	68
5.7 <b>(A-C)</b> Relative mode powers for three different lengths for the case of high purity ( $> 21dB$ ) $OAM^+$ mode excitation at 1550 nm (OAM power refers to combined $OAM^+$ and $OAM^-$ mode powers, and $LP_{01}$ refers to combined powers of the two $LP_{01}^\pm$ states). <b>(D)</b> Measured modal power ratios as a function of fiber length for the same case as in A-C. <b>(E)</b> Relative mode powers with respect to time, showing the temporal stability of the OAM modes. . . . .	70

5.8 (A) Power fraction in the fundamental, transverse, and $HE_{21}$ pairs; (B) Power estimated in the $HE_{11}$ modes by regression analysis (red crosses) and by coupling into a SMF (blue curve). (C) Estimated power fraction of each of the two OAM states; (D) Estimated relative phase of the two OAM states. . . . .	72
6.1 OAM division multiplexing principle. Four modes with distinct values of OAM ( $l$ ) and spin ( $s$ ) values are multiplexed into a specialty fiber, propagated and analyzed at the output using bit-error-rate tester (BERT) and/or imaged using near-IR camera. . . . .	74
6.2 Detailed (de) multiplexing experimental setup: signal from the transmitter (Tx) is split into four individual fiber arms. Two of the arms were converted into OAM modes using LCoS-SLM. Two fundamental modes were added collinearly to the two OAM modes using 3dB-loosy non-polarizing beam-splitter. All four modes are then coupled into vortex fiber, and analyzed at the output after being demultiplexed accordingly. Acronyms: flip mirror (FM), half wave plate (HWP), (non)-polarizing beam-splitter ((N)PBS), polarization beam combiner (PBC), polarization controller (PC), mirror (M), quarter wave plate (QWP). . . . .	75
6.3 NIR camera images of the channel outputs after 1.1km fiber propagation using 50GBaud modulated ECL source (linewidth of 0.4nm). (A-D) Intensity images (E, F) Phase images of $OAM^+$ and $OAM^-$ . (G, H) Intensity and phase of the $OAM^+$ mode after demultiplexing using inverse fork pattern. . . . .	77

6.4 Cross-talk and Multipath interference. <b>(A)</b> Cross-talk measurement example <b>(B)</b> Example of the $LP_{01}^+$ mode power drift (attributed to the cross-talk and free-space optics) and power fluctuations (due to multipath interference - MPI). (Inset) Cross talk and MPI mechanisms; mode A can couple into mode B producing cross-talk, but certain amount of the power can couple back into mode A interfering with the original signal, producing MPI. Both cross-talk and MPI cause higher BER. <b>(C)</b> Table of measured values for cross-talk and MPI for all four modes. . . . .	78
6.5 Drift and MPI of all four modes. . . . .	79
7.1 Basic modulation formats using amplitude and phase od the field. Non-return to zero (NRZ) denotes that signal doesn't go to zero between two bits that both carry '1'. With permission from Wikipedia, © Creative Commons. . . . .	83
7.2 Advanced modulation formats (Winzer and Essiambre, 2006). For us most important formats is differential quadrature phase shift keying (DQPSK) that we use in our systems experiment. For full list of acronyms consult (Winzer and Essiambre, 2006). With permission from (Winzer and Essiambre, 2006), © IEEE. . . . .	84
7.3 Direct (A) vs Coherent (B) modulation formats. With permission from Wikipedia, © Creative Commons. . . . .	84

7.4 Concept of quadrature phase shift keying (QPSK) and eye-diagram for bit-error-rate testing. **(A)** Ideal QPSK constellation. A sender can encode information in a  $\pi/4$ ,  $+3\pi/4$ ,  $5\pi/4$  and  $+7\pi/4$  phase, corresponding to 11, 01, 00 and 11 bit combination. Therefore, a phase can carry 4 possible states. **(B)** Noisy case. A phase of light can suffer changes due to fiber impediments, and in the noisy case, wrong phase can be detected, and errors in transmission can occur. **(C)** Concept of an eye diagram in the case of intensity modulation. Train of pulses carrying bits can be overlapped to create an eye-shaped diagram. **(C)** In a noisy case, distortion can cause "eye-closing" introducing errors in transmission. Similar eye diagram can be observed in the QPSK case.

C and D with permission from Wikipedia, © Creative Commons . . . 86

7.5 Systems experiment setup: signal from the laser or WDM source is modulated, amplified using an erbium doped fiber amplifier (EDFA), filtered using a band pass filter (BPF) and split into four individual fiber arms (two in the case of the WDM experiment). Two of the arms were converted into OAM modes using the input SLM. Two fundamental modes were also collinearly aligned with the two OAM modes using a beam-splitter, and all four modes were coupled into the fiber. After propagation, the modes are demultiplexed sequentially and sent for coherent detection and offline digital signal processing (DSP). Acronyms: ADC - analog digital converter, Att - attenuator, FM - flip mirror, LO - local oscillator, OC - optical coupler, (N)PBS: (non)-polarizing beam-splitter, PBC - polarization beam combiner, PC - polarization controllers, PC-SMF - polarization controller on SMF, PC-VF - polarization controller on vortex fiber. OC: optical coupler, (N)PBS: (non)-polarizing beam-splitter, PBC: polarization beam combiner, PC: polarization controller . . . . .	88
7.6 Constellation diagrams in the case of 4-mode OAM-MDM, with 50 Gbaud NRZ-QPSK, $\lambda = 1550\text{nm}$ , for the single-channel, and all-channel cases. Note the larger distortion of the constellations in the all-channel case. . . . .	90
7.7 Data transmission experiments. <b>(A)</b> Block diagram of $50 \times 2$ Gb/s QPSK signal transmission over a single wavelength carrying 4 modes in the vortex fiber. <b>(B)</b> Measured BER as a function of received power for the single-channel (SC) and all-channels (AC) transmission case. . . . .	91

7.8 (A) Block diagram of $20 \times 4$ Gb/s 16-QAM signal transmission over 10 wavelengths carrying 2 modes in the vortex fiber. (B) Measured crosstalk between $OAM^\pm$ modes as a function of wavelength. (C) BER as a function of wavelength for $OAM^\pm$ modes in the WDM system. . . . .	92
7.9 Additional experimental results of the 2-OAM modes, 10 wavelengths, 16-QAM systems experiments. (A) Spectrum of the modulated signal at the output of the WDM 16-QAM Tx, and spectrum of the $OAM^+$ mode at the receiver after demultiplexing. (B) Constellations of 16-QAM modulation for the demultiplexed $OAM^+$ mode at 1550.64 nm, for several cases (without and with crosstalk). (C) BER as a function of received power at 1550.64 nm, for B2B, and OAM modes without and with XT from WDM channels or the other OAM mode. . . . .	93
7.10 Spiral interference patterns, showing helical phase, of the $OAM^+$ mode at different wavelengths for the same vortex fiber conditions (no polarization controller adjustments). (A-D) Spiral patterns for the wavelengths spaced in 10pm, 100pm, and 1000pm. (E-H) Spirals for the wavelengths spaced in 10nm. . . . .	94
8.1 Setup to measure polarization dependence of a beamsplitter. . . . .	102
8.2 Sample Newport 10BC17MB.1. Measured polarization after reflection for three different positions of a polarizer: a) horizontal, b) vertical and c) $45^\circ$ degrees linearly polarized states, as well as after transmission of a $45^\circ$ degrees linearly polarized state (d). Clearly, phase delay between polarizations is introduced in the case of a $45^\circ$ degrees linearly polarized state, especially in the reflection case. . . . .	103

8.3	Polarization after reflection of a $45^\circ$ angled mirror (Thorlabs, <i>BB1 – E04</i> ) . . . . .	103
8.4	Polarization after reflection from a beam-splitter (Thorlabs BS015) . .	103
8.5	Schematic of experimental setup. Polarization-entangled photons (1550-nm and 1558-nm) are sent in two different channels A and B. 1.1km long channel A used two gratings to convert between fundamental and OAM mode with > 80% efficiency. Channel B consisted of 5km long single mode fiber (SMF); Time delay was tuned to target coincidence of channel A photons (traveled in a fundamental mode) and channel B photons (traveled in the OAM mode). Full quantum tomography measurement was applied at the receivers' end and density matrix of photon pair was measured. . . . .	104
8.6	Resonances for the case of microbend only (right), $CO_2$ only (center) and both (left). . . . .	105
8.7	Measured density matrix, P-parameter, concurrence (C) and S-parameter. . . . .	105

## List of Abbreviations

AOF	.....	adaptive optics feedback
BER	.....	bit-error rate
CCD	.....	charged-coupled device
CW	.....	continuous wave
DSP	.....	digital signal processing
DSF	.....	dispersion shifter fiber
ECL	.....	external cavity laser
EDFA	.....	Erbium-doped fiber amplifier
FDE	.....	frequency domain equalization
FFT	.....	fast Fourier transform
FM	.....	flip-mirror
FWM	.....	four-wave mixing
FWHM	.....	full-width at half maximum
HOM	.....	higher-order-mode
GD	.....	group delay
ITU	.....	International Telecommunications Union
IEEE	.....	Institute of Electrical and Electronics Engineers
LAN	.....	local-area network
LCoS	.....	liquid crystal on silicon
LG	.....	Laguerre-Gaussian
LO	.....	local oscillator
MD	.....	mode dispersion
MCF	.....	multi-core fiber
MDM	.....	mode-division multiplexing
MDL	.....	mode dependant loss
MIMO	.....	multiple-input multiple-output
MMF	.....	multi-mode fiber

OAM	.....	orbital angular momentum
OD	.....	outer diameter
OFDE	.....	orthogonal frequency domain multiplexing
OOK	.....	on-off-keying
OSA	.....	optical spectrum analyzer
PDM	.....	polarization-division-multiplexing
PIC	.....	photonic integrated circuit
PSK	.....	phase-shift-keying
QAM	.....	quadrature-amplitude-modulation
QPSK	.....	quadrature-phase-shift-keying
SE	.....	spectral-efficiency
SDM	.....	space-division-multiplexing
SLM	.....	spatial-light-modulator
SMF	.....	single mode fiber
SNR	.....	signal-to-noise-ratio
TDE	.....	time-domain equalization
TE	.....	transverse electric
TM	.....	transverse magnetic
WDM	.....	wavelength-division-multiplexing
WGA	.....	weakly-guided approximation

## Chapter 1

# Introduction

### 1.1 Optical fiber communications and space-division multiplexing

Optical communication network traffic has been steadily increasing by a factor of 100 every decade, with the capacity of single-mode optical fiber increasing 10'000 times in the last three decades (Essiambre and Tkach, 2012) (Fig. 1·1). Historically, this growth has been sustained by information multiplexing techniques using wavelength, amplitude, phase and polarization of light as means to encode information (Agrawal, 2010). Several major discoveries in the fiber optics domain enabled the today's optical networks. The first one was led by Charles M. Kao ground-breaking work that recognized glass impurities as the major loss mechanism (at the time bulk glass loss was  $\approx 200dB/km$  at  $1\mu m$ ) (Kao and Hockham, 1966). This work gave the birth to optical fibers and led to the first commercial fibers in the 1970 with attenuation low enough for communication purposes ( $\approx 20dB/km$ ). Development of single mode fibers (SMF) in the early 80's reduced pulse dispersion and lead to the first fiber-optic based transatlantic telephone cables. Development of Indium Gallium Arsenide photodiode in the early 90's shifted the focus to the near infrared wavelengths (1550nm), where silica has the lowest loss, enabling extended reach. At roughly the same time, the invention of erbium-doped fiber amplifiers resulted in one of the biggest leaps in fiber capacity in the history of communications, a 1000-fold increase in capacity in 10 years (Fig. 1·1 B). The improvement was mainly due to removed

need for expensive repeaters for signal regeneration, as well as efficient amplification of many wavelengths at the same time, enabling wavelength-division-multiplexing (WDM). Throughout the 2000s, bandwidth increase came mainly from introduction of complex signal modulation formats and coherent detection, allowing information encoding using the phase of light. Most recently, polarization-division-multiplexing (PDM) doubled the channel capacity (Fig. 1.1 A-B).

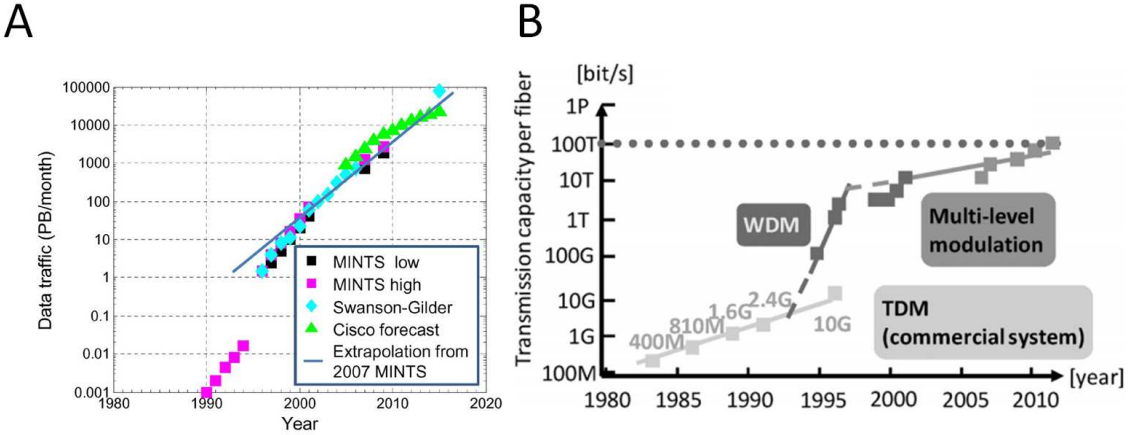


**Figure 1.1:** (A) North American Internet traffic in Petabytes/month according to several studies, such as Minnesota Internet Traffic Study (MINTS) and Cisco. (Essiambre and Tkach, 2012). (B) Capacity evolution for different communication systems (Sakaguchi et al., 2012). With permission from (Essiambre and Tkach, 2012) and (Sakaguchi et al., 2012), © IEEE.

Though fiber communications based on SMFs featured tremendous growth in the last three decades, recent research has indicated SMF limitations. Nonlinear effects in silica play a significant role in long-range transmission, mainly through Kerr effect, where a presence of a channel at one wavelength can change the refractive index of a fiber, causing distortions of other wavelength channels (Marcuse et al., 1991). Recently, a spectral efficiency (SE) (or bandwidth efficiency), referring to the transmitted information rate over a given bandwidth, has been theoretically analyzed assuming nonlinear effects in a noisy fiber channel (Essiambre et al., 2010). This

research indicates a specific SE limit that a fiber of a certain length can reach for any signal-to-noise ratio (SNR) (Fig. 1·2 A). Recently achieved SE results indeed show the proximity to the SE limit (by a factor less than 2), indicating the need for new technologies to address the capacity issue in the future (Fig. 1·2 B).

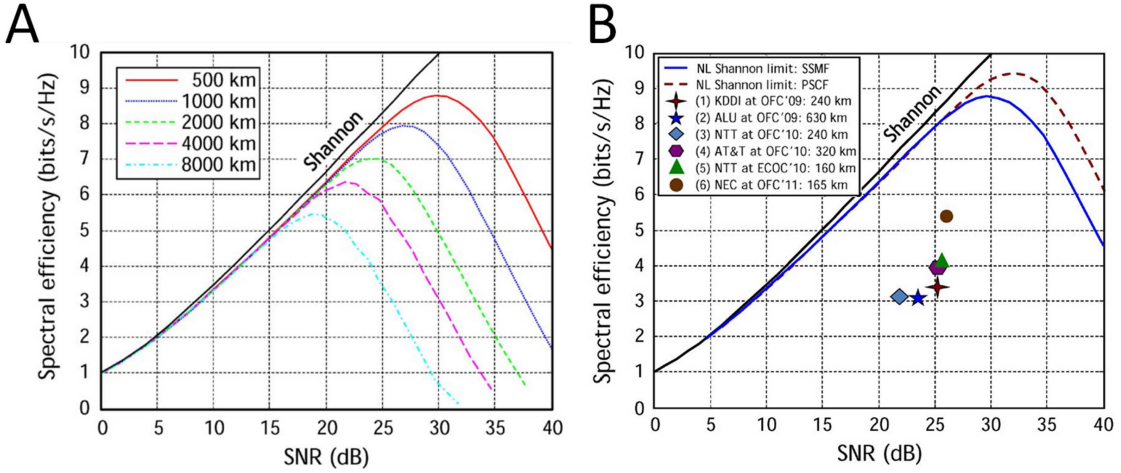


**Figure 1·2:** (A) Simulated results for spectral efficiency vs signal-to-noise ratio using additive-white-Gaussian noise without dispersion compensation. (B) Current state-of-the-art in single-mode fiber transmission (Essiambre and Tkach, 2012). With permission from (Essiambre and Tkach, 2012), © IEEE.

Among several possible directions for optical communications in the future, introduction of new fibers, instead of SMFs, has already shown promising results in recent years (Winzer, 2010; Richardson, 2010). In particular, researchers have focused on a spatial dimension in new fibers, leading to so-called space-division-multiplexing (SDM), where information is transmitted using cores of multicore fibers (MCFs) (Sakaguchi et al., 2012; Lee et al., 2012), or mode-division-multiplexing (MDM), where information is transmitted using modes of a multimode fibres (MMFs) (Berdagué and Facq, 1982; Freund et al., 2010; Ryf et al., 2012; Salsi et al., 2012) (Fig. 1·3). Latest results show SE of 91 bit/s/Hz using 12-core MCF for 52km long fiber (Takara et al., 2012), and 12 bit/s/Hz using 6-mode MMF in 112 km long fiber (Sleiffer et al.,

2012) (compare with Fig. 1·2 A for SMF). Somewhat unconventional transmission at  $2.08 \mu\text{m}$  has also been demonstrated in 290m-long photonic crystal fibers, though still with high losses (4.5 dB/km) (Petrovich et al., 2012).

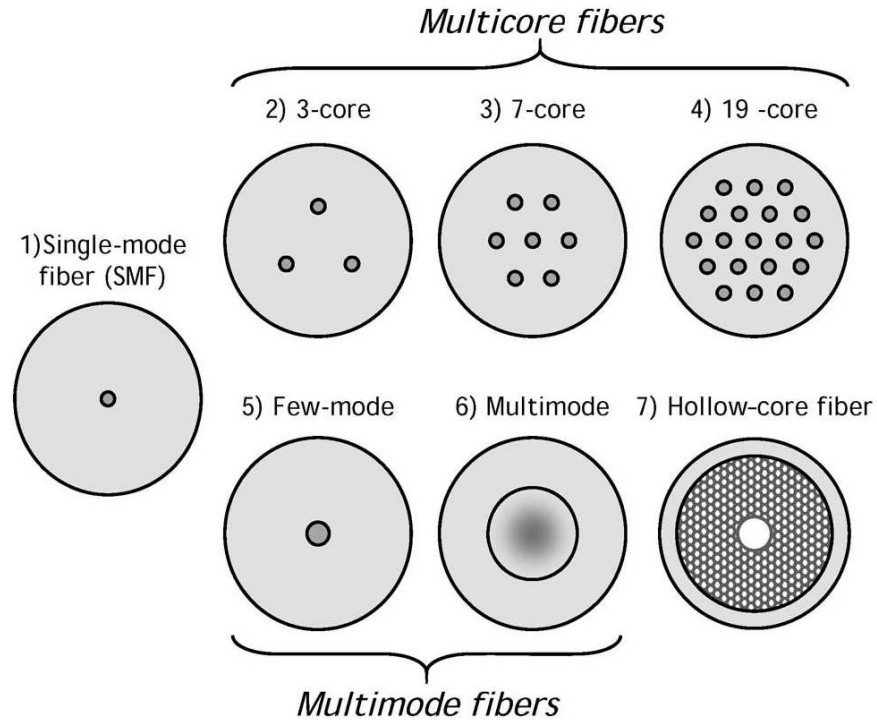


**Figure 1·3:** Different types of fibers considered for future communication links in order to increase network capacity (Essiambre and Tkach, 2012). With permission from (Essiambre and Tkach, 2012), © IEEE.

While offering promising results, these new types of fibers have their own limitations. Being non-circularly symmetric structures, MCFs are known to require more complex, expensive manufacturing. On the other hand, MMFs are easily created using existing technologies (Wang et al., 2006), however, conventional MMF systems are known to suffer from mode coupling caused by both random perturbations in fibers (Gloge, 1972; Marcuse, 1974) and in modal (de)multiplexers (Ryf et al., 2012). Several techniques can be used for mitigating mode coupling. In a strong-coupling regime (typically  $>\text{km}$ ), modal crosstalk must be compensated using computationally inten-

sive multiple-input multiple-output (MIMO) digital signal processing (DSP) (Stuart, 2000; Randel et al., 2011). While MIMO DSP leverages the technique's current success in wireless networks (Foschini and Gans, 1998)<sup>1</sup>, the wireless networks data rates are several orders of magnitude lower than ones required for optical networks. Furthermore, MIMO DSP complexity inevitably increases with an increasing number of modes (Arik et al., 2013) and no MIMO-based data transmission demonstrations have been demonstrated in real time so far. Furthermore, unlike wireless communication systems, optical systems are further complicated because of fiber nonlinear effects (Essiambre and Tkach, 2012). In a weak-coupling regime (typically <km) where cross-talk is smaller, methods that also use computationally intensive adaptive optics feedback algorithms have been demonstrated (Panicker and Kahn, 2009; Carpenter and Wilkinson, 2012b). These methods "reverse" the effect of mode coupling by sending a desired superposition of modes at the input, so that desired output mode can be obtained. This approach is limited however, since mode coupling is a random process that can change on the order of a millisecond in conventional fibers ((Ho and Kahn, 2013) p. 40). Therefore, the adaptation of this method can be problematic in long-haul systems, where the round-trip signal propagation delay can be tens of milliseconds. Though  $2 \times 56Gb/s$  transmission at 8km length has been demonstrated in the case of two higher order modes (Carpenter et al., 2013), none of the adaptive optics MDM methods to date have been demonstrated for more than two modes.

In this dissertation we introduce a new possibility for future network capacity increase, using a special class of MMFs capable of reducing mode coupling. This new type of fibers allows for propagation of so-called orbital angular momentum (OAM) fiber modes. Regarding the MIMO-based MDM and adaptive optics techniques that we mentioned, our approach offers two potential advantages: 1) by using specially designed optical fibers to reduce mode coupling, the computational complexity required

---

<sup>1</sup>MIMO DSP was introduced in 4G wireless networks

on the electronic end can be reduced, and 2) because of the uniqueness of OAM modes over other basis sets (that we'll explore more in details), these modes offer theoretically lossless ways of multiplexing into fibers (Berkhout et al., 2010; Sullivan et al., 2012; Su et al., 2012; Cai et al., 2012). Before we go further into details of the method we propose here, we first introduce the orbital angular momentum of light.

## 1.2 Orbital angular momentum (OAM) of light

Together with energy and momentum, angular momentum is one of the most fundamental physical quantities in classical and quantum electrodynamics (Mandel and Wolf, 1995). In a vacuum, electromagnetic angular momentum is defined as:

$$\vec{\mathcal{M}} \stackrel{\text{def}}{=} \epsilon_0 \vec{r} \times (\vec{\mathcal{E}} \times \vec{\mathcal{B}})$$

where  $\vec{\mathcal{E}}$  and  $\vec{\mathcal{B}}$  are electrical and magnetic fields, and  $\epsilon_0$  is the vacuum electric permittivity. In paraxial beams, angular momentum can be divided into spin angular momentum (SAM) and orbital angular momentum (OAM) (Jackson, 1962). SAM is associated with photon spin and is manifested as circular polarization (Poynting, 1909; Beth, 1936). In contrast, OAM is linked to the spatial distribution of the electric field (Jackson, 1962). In particular, beams with electric field proportional to  $\exp(il\phi)$ , have the OAM of  $l\hbar$  per photon (Allen et al., 1992), where  $l$  is topological charge,  $\phi$  is azimuthal angle, and  $\hbar$  is Planks constant  $h$  divided by  $2\pi$ . Examples of the beams that have non-zero OAM include free-space Laguerre-Gaussian beams ( $LG_{lm}$  modes with  $l \neq 0$ ), as well as Bessel beams, Mathieu beams, and Ince-Gaussian beams (Fig. 1.4 A). Due to their phase singularity in the center of the beam, OAM carrying beams (or simply OAM beams) are also called vortex beams or optical vortices.

Since their first lab demonstration (Allen et al., 1992), OAM beams achieved a widespread scientific and technological interest in the areas of optical tweezers (Cur-

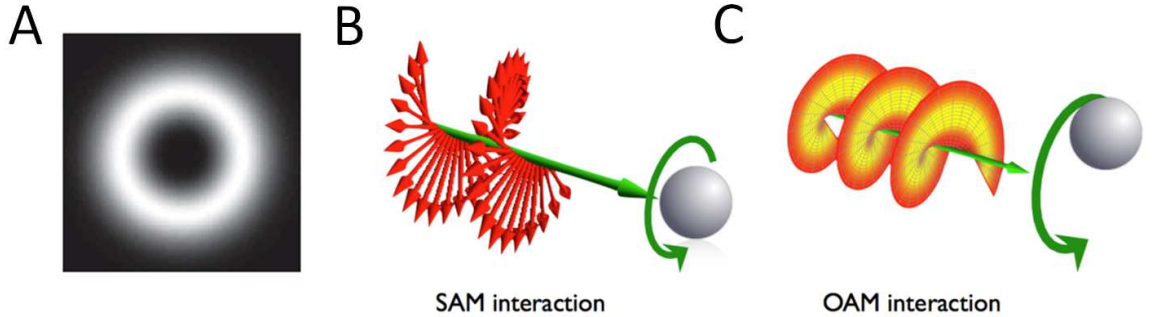


**Figure 1·4:** (A) Illustration of a doughnut shaped intensity of Laguerre Gaussian  $l = 1$  beam ( $LG_{10}$ ). Due to phase singularity in the center of the beam, OAM beams are also called vortex beams. (B) Circularly polarized  $LG_{00}$  beam, that carry spin angular momentum (SAM), can rotate an object upon illumination. (C) Similarly to SAM, an  $LG_{10}$  beam can transfer orbital angular momentum (OAM) and rotate an object, potentially at much higher rates. With permission from Wikipedia, © Creative Commons.

tis and Grier, 2003; Kreysing et al., 2008; Ladavac and Grier, 2004) (Fig. 1·4 B-C), atom manipulation (Tabosa and Petrov, 1999; Andrews, 2008), microscopy (Hell and Wichmann, 1994), free-space classical communications (Yao and Padgett, 2011; Gibson et al., 2004; Wang et al., 2012) and quantum communication links (Gröblacher et al., 2006). There are several known ways to generate OAM beams; the most common methods include free-space mode conversion using phase plates (Khonina et al., 1992) and computer generated holograms (He et al., 1995) (Fig. 1·5). It is of special interest to us, to note the work of several groups on creating OAM modes in fibers. Most notably, Dashti et al. used acoustic gratings to create OAM states in 30cm straight fibers (Dashti et al., 2006), and Volpe and Petrov used holographic phase mask conversion and free-space coupling in 35 cm straight fibers (Volpe and Petrov, 2004). Recently Wong et al. used helically twisted photonic crystal fibers of 6mm length (Wong et al., 2012). We note that in all these cases, fiber length was short, due to the fact that OAM modes are subject to mode coupling. The main goal of

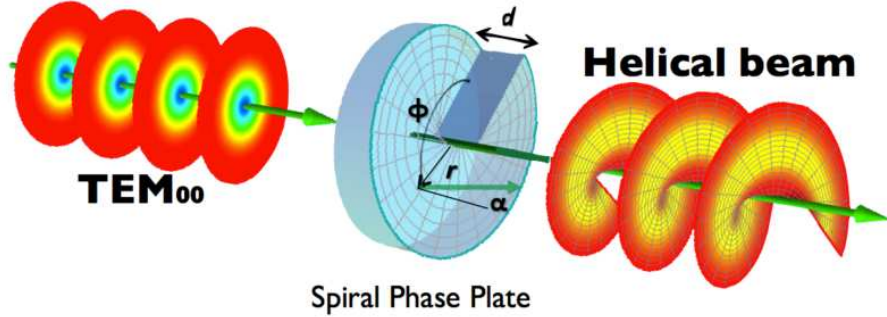


**Figure 1·5:** Example of conversion between fundamental Laguerre Gaussian ( $LG_{0m}$ ) and higher order ( $LG_{1m}$ ) beam using a spiral phase plate with a phase step equal to  $d = 2\pi l \lambda \approx 10\mu m$  (for  $l = 1$  and  $\lambda = 1550nm$ ). With permission from Wikipedia, © Creative Commons.

this dissertation is to study whether a special class of fibers can overcome this problem of mode coupling, allowing OAM mode propagation for longer fiber lengths. If OAM mode stability is feasible in fibers, data streams could be, in principle, sent using independent fiber OAM modes. This concept of OAM mode-division-multiplexing (OAM-MDM) has been previously used in free-space where several classical and quantum communications experiments have exploited this inherent orthogonality of OAM modes (Gibson et al., 2004; Gröblacher et al., 2006; Wang et al., 2012). This dissertation aims to address the possibility of fiber-based OAM-MDM, as a way of capacity increase in future fiber based systems (Fig. 1·6).

We start this study by mathematical description of MMFs using electromagnetic theory (Ch. 2). We introduce OAM fiber modes and discuss the parameters necessary for their stability. In chapter 3, we study the properties of a special type of fibers, called vortex fibers, using numerical and experimental methods. We observe that vortex fibers indicate reduce mode coupling and we verify the existence of OAM modes qualitatively. In chapter 4, we address OAM mode generation in vortex fibers using methods based on fiber gratings and spatial light modulators (SLMs), both methods used for results presented in subsequent chapters. In chapter 5 we study two meth-

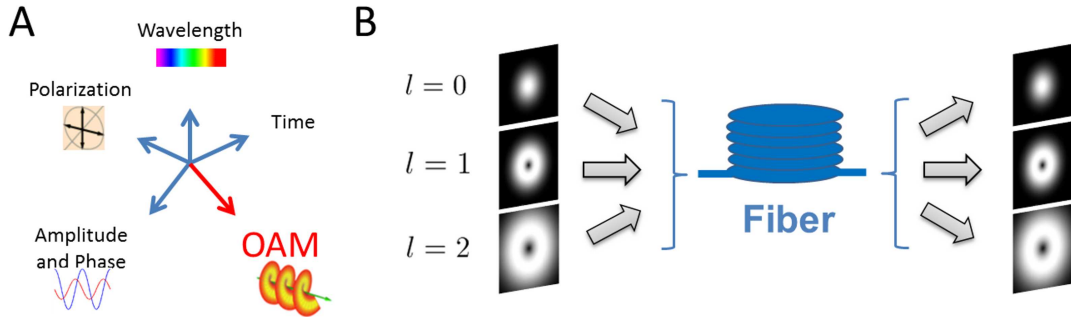


**Figure 1.6:** (A) In this dissertation we study the idea of OAM as a new, orthogonal, degree of freedom in addition to wavelength, phase, amplitude and polarization, for multiplexing in the future optical communication systems. (B) OAM mode division multiplexing in fibers concept.

ods for determining purity of OAM modes: the ring technique and the regression method. Using these methods we address the OAM mode evolution for different fiber lengths. In Chapter 6 we study how to excite several OAM modes simultaneously to achieve OAM-MDM. We describe a 4-mode multiplexing and demultiplexing system of two fundamental and two  $l = \pm 1$  modes using free space optics and spatial light modulators. Finally, in chapter 7 we present the results of data transmission experiments using four aforementioned modes to achieve data transmission at 400 Gbit/s using four OAM modes, at a single wavelength, and 1.6Tbit/s using two OAM modes and 10 wavelengths. In chapter 8, we discuss some of the limitations of OAM-MDM method, and speculate future directions.

## Chapter 2

# Multimode Fibers and Mode Stability

In this chapter we first use electromagnetic theory to derive solutions for multimode fiber waveguides (also called modes) in a weakly guided approximation. We then shown that certain fiber modes have non-zero OAM of topological charge  $l$  (hence the name OAM modes). Similarly to the free-space  $LG_{lm}$  modes, these OAM modes have a helical phase of electric field proportional to  $\exp(il\phi)$  and as we will see, the crucial factor for this is an existence of non-zero azimuthal component of a Poynting vector. At the end of the chapter, we discuss the necessary conditions for these OAM states to be stable in fibers, and the role of fiber mode coupling which in general case restricts a long-range OAM mode fiber propagation.

### 2.1 Optical fiber waveguide theory

Optical fibers waveguide theory has been well studied in literature (Saleh and Teich, 2007; Iizuka, 2002; Snyder and Love, 1983). In an ideal case, optical fibers are 2D cylindrical waveguides comprising one (or several) cores surrounded by a cladding having slightly lower refractive index (we assume no changes across longitudinal dimension of a fiber). A fiber mode is a solution (also known as eigenstate) of a waveguide equation describing the field distribution that propagates in a fiber without changing, except for the scaling factor. All fibers have a limit on the number of modes that they can be propagating (denoted as  $N$ ), and we include both spatial and polarization degree of freedom. SMFs support propagation of two orthogonal

polarizations of the fundamental mode only ( $N=2$ ), while for sufficiently large core radius and/or the core-cladding difference, a fiber is multimoded ( $N > 2$ ). Here, we are mostly interested in a subset of multimode fibers that are weakly guided, meaning that the core-cladding refractive index difference can be considered to be very small. Most glass fibers made today are weakly guided with the exception of some photonic crystal fibers and air-core fibers. We'll show that a step-index fibers guide modes in groups, where within each group modes typically have similar properties in terms of effective index. Within a group the modes are said to be degenerate. However, as we'll see, these degeneracies can be broken in a certain fiber profile design.

We now look into mathematical description of the modes. In our derivation we follow (Snyder and Love, 1983). We start by describing translationally invariant waveguide with refractive index  $n = n(x, y)$ , with  $n_{co}$  being maximum refractive index (typically in the "core" of a waveguide), and  $n_{cl}$  being refractive index of the uniform cladding, and  $\rho$  represents the maximum radius of the refractive index  $n$ . Due to translational invariance the solutions (or modes) for this waveguide, that we are looking to find, can be written as:

$$\mathbf{E}_j(x, y, z) = \mathbf{e}_j(x, y)e^{i\beta_j z}, \quad (2.1)$$

$$\mathbf{H}_j(x, y, z) = \mathbf{h}_j(x, y)e^{i\beta_j z}, \quad (2.2)$$

where  $\beta_j$  is called propagation constant of the  $j$ -th mode. Vector wave equation for source free Maxwell's equation can be written in this case as:

$$(\nabla_t^2 + n^2 k^2 - \beta_j^2) \mathbf{e}_j = -(\nabla_{\mathbf{t}} + i\beta_j \hat{\mathbf{z}})(\mathbf{e}_{tj} \cdot \nabla_{\mathbf{t}} \ln(n^2)), \quad (2.3)$$

$$(\nabla_t^2 + n^2 k^2 - \beta_j^2) \mathbf{h}_j = -(\nabla_{\mathbf{t}} \ln(n^2)) \times ((\nabla_{\mathbf{t}} + i\beta_j \hat{\mathbf{z}}) \times \mathbf{h}_j), \quad (2.4)$$

where  $k = 2\pi/\lambda$  is the free-space wavenumber,  $\lambda$  is a free-space wavelength,  $\mathbf{e}_t = e_x \hat{\mathbf{x}} + e_y \hat{\mathbf{y}}$  is a transverse part of the electric field,  $\nabla_t^2$  is a transverse Laplacian and

$\nabla_t$  transverse vector gradient operator. Waveguide polarization properties are built into the wave equation through the  $\nabla_t \ln(n^2)$  terms and ignoring them would lead to the scalar wave equation, with linearly polarized modes. We define profile height parameter  $\Delta$ , waveguide or fiber parameter  $V$  and modal parameters  $U_j$  and  $W_j$  as:

$$\Delta \stackrel{\text{def}}{=} \frac{1}{2} \left( 1 - \frac{n_{cl}^2}{n_{co}^2} \right), \quad (2.5)$$

$$V \stackrel{\text{def}}{=} \frac{2\pi\rho}{\lambda} (n_{co}^2 - n_{cl}^2)^{1/2}, \quad (2.6)$$

$$U_j \stackrel{\text{def}}{=} \rho(k^2 n_{co}^2 - b_j^2)^{1/2}, \quad (2.7)$$

$$W_j \stackrel{\text{def}}{=} \rho(b_j^2 - k^2 n_{cl}^2)^{1/2}, \quad (2.8)$$

where  $V^2 = U_j^2 + W_j^2$ .

While previous equations satisfy arbitrary waveguide profile  $n(x, y)$ , in most cases of interest, profile height parameter  $\Delta$  can be considered small  $\Delta \ll 1$ , in which case waveguide is said to be weakly guided, or that weakly guided approximation (WGA) holds. If this is the case, a perturbation theory can be applied to approximate the solutions (Eq. 2.1) as:

$$\mathbf{E}(x, y, z) = \mathbf{e}(x, y) e^{i(\beta + \tilde{\beta})z} = (\mathbf{e}_t + \hat{\mathbf{z}} e_z) e^{i(\beta + \tilde{\beta})z} \quad (2.9)$$

$$\mathbf{H}(x, y, z) = \mathbf{h}(x, y) e^{i(\beta + \tilde{\beta})z} = (\mathbf{h}_t + \hat{\mathbf{z}} h_z) e^{i(\beta + \tilde{\beta})z}, \quad (2.10)$$

where subscripts t and z denote transverse and longitudinal components respectively. Longitudinal components can be considered much smaller in WGA and we can approximate (but not neglect) them as:

$$e_z = \frac{i(2\Delta)^{1/2}}{V} (\rho \nabla_t \cdot \mathbf{e}_t) \quad (2.11)$$

$$h_z = \frac{i(2\Delta)^{1/2}}{V} (\rho \nabla_t \cdot \mathbf{h}_t) \quad (2.12)$$

and transversal components satisfy the simplified wave equation:

$$(\nabla_t^2 + n^2 k^2 - \tilde{\beta}_j^2) \mathbf{e}_j = 0, \quad (2.13)$$

$$\mathbf{h}_t = n_{co} \left( \frac{\epsilon_0}{\mu_0} \right)^{1/2} \hat{\mathbf{z}} \times \mathbf{e}_t. \quad (2.14)$$

We can write the polarization correction  $\delta\beta$  as:

$$\delta\beta = \frac{(2\Delta)^{3/2}}{2\rho V} \frac{\int_A (\rho \nabla_t \cdot \mathbf{e}_t) \mathbf{e}_t \cdot \rho \nabla_t f dA}{\int_A \mathbf{e}_t^2 dA}, \quad (2.15)$$

and delta can be approximated as  $\Delta \cong \frac{n_{co} - n_{cl}}{n_{co}}$ , and V parameter as:

$$V = k\rho n_{co} \sqrt{n_{co}^2 - n_{cl}^2} = k\rho n_{co} (2\Delta)^{1/2}. \quad (2.16)$$

Though WGA simplified the waveguide equation, further simplification can be obtained by assuming circularly symmetric waveguide (such as ideal fiber). If this is the case refractive index that can be written as:

$$n(r) = n_{co}^2 (1 - 2f(R)\Delta) \quad (2.17)$$

where  $f(R) \geq 0$  is our small arbitrary profile variation.

For a circularly symmetric waveguide, solving Eq. 2.13 can be simplified by the separation of variables and the solutions (Eq. 2.9 and Eq. 2.10) will have propagation constants  $\beta_{lm}$  that are classified using azimuthal ( $l$ ) and radial ( $m$ ) numbers. Another classification uses effective indices  $n_{lm}$  (sometimes noted as  $n_{lm}^{eff}$  or simply  $n_{eff}$ , that are related to propagation constant as:  $\beta_{lm} = kn_{lm}^{eff}$ ). For the case of  $l = 0$ , the solutions can be separated into two classes that have either transverse electric ( $TE_{0m}$ ) or transverse magnetic ( $TM_{0m}$ ) fields (so called *meridional* modes). In the case of  $l \neq 0$ , both electric and magnetic field have z-component, and depending on which one is more dominant, so-called *hybrid modes* are denoted as:  $HE_{lm}$  and  $EH_{lm}$ . Complex

amplitudes for the two cases ( $l = 0, l \geq 1$ ), are given in the tables 2.1 - 2.3 (Snyder and Love, 1983), where  $F_l$  represents solution of the Bessel equation:

$$\left[ \frac{d^2}{dR^2} + \frac{1}{R} \frac{d}{dR} - \frac{l^2}{R^2} + \tilde{U}^2 - V^2 f(R) \right] F_l(R) = 0, \quad (2.18)$$

and  $\tilde{U}$ ,  $\tilde{\beta}$  (approximated  $U$  and  $\beta$ ), and  $G_l^\pm$  are defined as:

$$\tilde{U}^2 \stackrel{\text{def}}{=} \rho(k^2 n_{co}^2 - \tilde{\beta}^2)^{1/2}, \quad (2.19)$$

$$\tilde{\beta} \stackrel{\text{def}}{=} \beta + \delta\beta, \quad (2.20)$$

$$G_l^\pm \stackrel{\text{def}}{=} \frac{dF_l}{dR} \pm \frac{l}{R} F_l, \quad (2.21)$$

where  $R = r/\rho$  is the normalized radius. We can also write simplified polarization correction  $\delta\beta$  in terms of two constituents, defined as (Snyder and Love, 1983):

$$I_1 \stackrel{\text{def}}{=} \frac{(2\Delta)^{3/2}}{4\rho V} \frac{\int_0^\infty RF_l(dF_l/dR)(df/dR)dR}{\int_0^\infty RF_l^2 dR} \quad (2.22)$$

$$I_2 \stackrel{\text{def}}{=} \frac{l(2\Delta)^{3/2}}{4\rho V} \frac{\int_0^\infty F_l^2(df/dR)dR}{\int_0^\infty RF_l^2 dR}. \quad (2.23)$$

Note that polarization correction  $\delta\beta$  has different values within the same group of modes with the same orbital number ( $l$ ), even in the circularly symmetric fiber (column  $\delta\beta$  in 2.3). This is an important observation that led to development of a special type of fiber that we discuss in Ch. 3.

Mode	$\mathbf{e}_t$	$\mathbf{h}_t$	$e_z$	$h_z$	$\delta\beta$
Even $HE_{1m}$	$\hat{\mathbf{x}}F_0$	$n_{co} \left( \frac{\epsilon_0}{\mu_0} \right)^{1/2} \hat{\mathbf{y}}F_0$	$i \frac{(2\Delta)^{1/2}}{V} G_0 \cos\phi$	$in_{co} \left( \frac{\epsilon_0}{\mu_0} \right)^{1/2} \frac{(2\Delta)^{1/2}}{V} G_0 \sin\phi$	$I_1$
Odd $HE_{1m}$	$\hat{\mathbf{y}}F_0$	$-n_{co} \left( \frac{\epsilon_0}{\mu_0} \right)^{1/2} \hat{\mathbf{x}}F_0$	$i \frac{(2\Delta)^{1/2}}{V} G_0 \sin\phi$	$-in_{co} \left( \frac{\epsilon_0}{\mu_0} \right)^{1/2} \frac{(2\Delta)^{1/2}}{V} G_0 \cos\phi$	$I_1$

**Table 2.1:** Fundamental  $HE_{11}$  and  $HE_{1m}$  modes ( $l = 0$ ). With permission from (Snyder and Love, 1983) © Chapman and Hall.

Mode	$\mathbf{e}_t$	$\mathbf{h}_t$
Even $HE_{l+1,m}$	$(\hat{\mathbf{x}} \cos l\phi - \hat{\mathbf{y}} \sin l\phi) F_l$	$n_{co} \left( \frac{\epsilon_0}{\mu_0} \right)^{1/2} (\hat{\mathbf{x}} \sin l\phi + \hat{\mathbf{y}} \cos l\phi) F_l$
$TM_{0m}(l = 1)$	$(\hat{\mathbf{x}} \cos l\phi + \hat{\mathbf{y}} \sin l\phi) F_l$	$-n_{co} \left( \frac{\epsilon_0}{\mu_0} \right)^{1/2} (\hat{\mathbf{x}} \sin l\phi - \hat{\mathbf{y}} \cos l\phi) F_l$
Even $EH_{l-1,m}(l > 1)$	$(\hat{\mathbf{x}} \cos l\phi + \hat{\mathbf{y}} \sin l\phi) F_l$	$-n_{co} \left( \frac{\epsilon_0}{\mu_0} \right)^{1/2} (\hat{\mathbf{x}} \sin l\phi - \hat{\mathbf{y}} \cos l\phi) F_l$
Odd $HE_{l+1,m}$	$(\hat{\mathbf{x}} \sin l\phi + \hat{\mathbf{y}} \cos l\phi) F_l$	$-n_{co} \left( \frac{\epsilon_0}{\mu_0} \right)^{1/2} (\hat{\mathbf{x}} \cos l\phi - \hat{\mathbf{y}} \sin l\phi) F_l$
$TE_{0m}(l = 1)$	$(\hat{\mathbf{x}} \sin l\phi - \hat{\mathbf{y}} \cos l\phi) F_l$	$n_{co} \left( \frac{\epsilon_0}{\mu_0} \right)^{1/2} (\hat{\mathbf{x}} \cos l\phi + \hat{\mathbf{y}} \sin l\phi) F_l$
Odd $EH_{l-1,m}(l \geq 1)$	$(\hat{\mathbf{x}} \sin l\phi - \hat{\mathbf{y}} \cos l\phi) F_l$	$n_{co} \left( \frac{\epsilon_0}{\mu_0} \right)^{1/2} (\hat{\mathbf{x}} \cos l\phi + \hat{\mathbf{y}} \sin l\phi) F_l$

**Table 2.2:** Transversal components for higher-order modes (HOMs) ( $l \geq 1$  modes). With permission from (Snyder and Love, 1983) © Chapman and Hall.

Mode	$e_z$	$h_z$	$\delta\beta$
Even $HE_{l+1,m}$	$i \frac{(2\Delta)^{1/2}}{V} G_l^- \cos(l+1)\phi$	$in_{co} \left( \frac{\epsilon_0}{\mu_0} \right)^{1/2} \frac{(2\Delta)^{1/2}}{V} G_l^- \sin(l+1)\phi$	$I_1 - I_2$
$TM_{0m}(l = 1)$	$i \frac{(2\Delta)^{1/2}}{V} G_1^+$	0	$2(I_1 + I_2)$
Even $EH_{l-1,m}(l > 1)$	$i \frac{(2\Delta)^{1/2}}{V} G_l^+ \cos(l-1)\phi$	$-in_{co} \left( \frac{\epsilon_0}{\mu_0} \right)^{1/2} \frac{(2\Delta)^{1/2}}{V} G_l^+ \sin(l-1)\phi$	$I_1 + I_2$
Odd $HE_{l+1,m}$	$i \frac{(2\Delta)^{1/2}}{V} G_l^- \sin(l+1)\phi$	$-in_{co} \left( \frac{\epsilon_0}{\mu_0} \right)^{1/2} \frac{(2\Delta)^{1/2}}{V} G_l^- \cos(l+1)\phi$	$I_1 - I_2$
$TE_{0m}(l = 1)$	0	$in_{co} \left( \frac{\epsilon_0}{\mu_0} \right)^{1/2} \frac{(2\Delta)^{1/2}}{V} G_1^+$	0
Odd $EH_{l-1,m}(l \geq 1)$	$i \frac{(2\Delta)^{1/2}}{V} G_l^+ \sin(l-1)\phi$	$in_{co} \left( \frac{\epsilon_0}{\mu_0} \right)^{1/2} \frac{(2\Delta)^{1/2}}{V} G_l^+ \cos(l-1)\phi$	$I_1 + I_2$

**Table 2.3:** Longitudinal components for higher-order modes ( $l \geq 1$  modes). With permission from (Snyder and Love, 1983) © Chapman and Hall.

In order to look more closely into mode properties, we choose step-index fiber as an example, for which refractive index can be written as:

$$n(R) = \begin{cases} n_{co}, 0 \leq R \leq 1, \text{core region} \\ n_{cl}, 1 < R < \infty, \text{cladding region} \end{cases} \quad (2.24)$$

In this case, solutions to the Eq. 2.18 are the Bessel functions of the first kind,  $J_l(r)$ , in the core region, and modified Bessel functions of the second kind,  $K_l(r)$ , in the cladding region. Solutions for  $n_{eff}$  in the step-index case are shown on the Fig. 2.1.

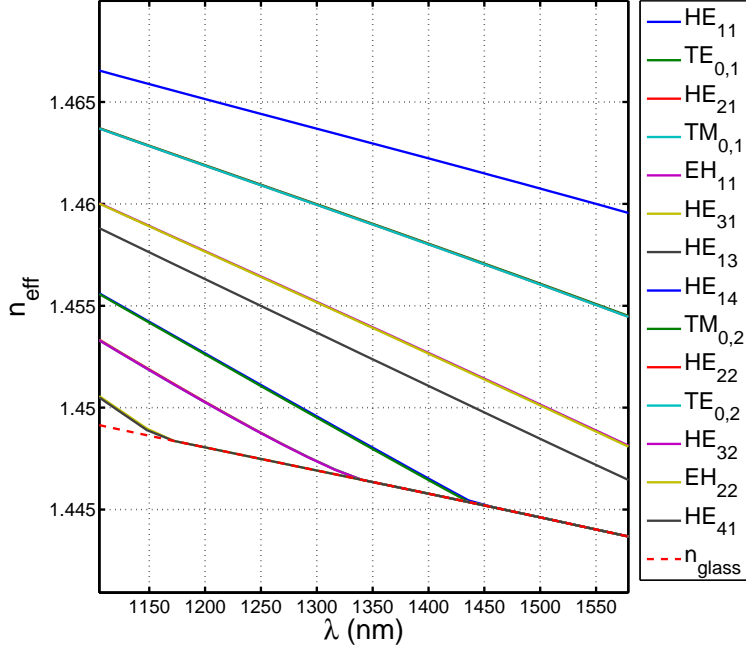


**Figure 2.1:** Numerical solutions for effective index,  $n_{eff}$ , for step index fiber, showing labeling and corresponding values of  $l$  and  $m$ .

In the case of step-index fiber the groups of modes are almost degenerate, also meaning that the polarization correction  $\delta\beta$  can be considered very small. Unlike  $HE_{11}$  modes, higher order modes (HOMs) can have elaborate polarizations, and first six modes ( $l = 0$  and  $l = 1$  groups) in a step index fiber are shown in Fig. 2.2. We note that in the case of circularly symmetric fiber, the odd and even modes (for example  $HE_{lm}^{odd}$  and  $HE_{lm}^{even}$  modes) are always degenerate (i.e. have equal  $n_{eff}$ ),

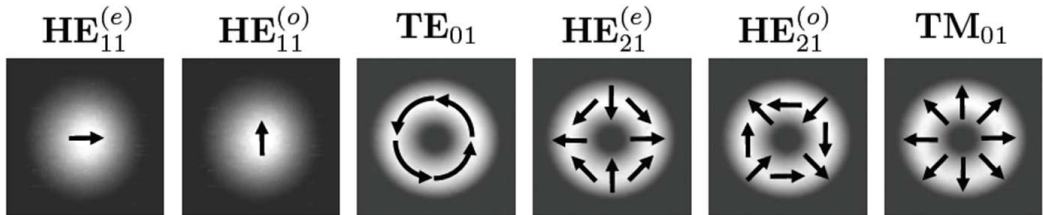


**Figure 2.2:** First six modes ( $l = 0$  and  $l = 1$  groups) in a step index fiber.

regardless of the index profile (see the  $\delta\beta$  column in the Table 2.3). These modes will be non-degenerate only in the case of circularly asymmetric index profiles; an example is polarization maintaining fiber (Rogers, 2008).

## 2.2 OAM fiber modes

Using Abraham definition (Barnett, 2010), angular momentum density ( $\mathcal{M}$ ) of light in a medium is defined as:

$$\mathcal{M} \stackrel{\text{def}}{=} \frac{1}{c^2} \mathbf{r} \times (\mathcal{E} \times \mathcal{H}) = \mathbf{r} \times \mathcal{P} = \frac{1}{c^2} \mathbf{r} \times \mathcal{S}, \quad (2.25)$$

with  $\mathbf{r}$  as position,  $\mathcal{E}$  electric field,  $\mathcal{H}$  magnetic field,  $\mathcal{P}$  linear momentum density and  $\mathcal{S}$  Poynting vector.

The total angular momentum ( $\mathcal{J}$ ), and angular momentum flux ( $\Phi_{\mathcal{M}}$ ) can be defined as:

$$\mathcal{J} \stackrel{\text{def}}{=} \iiint \mathcal{M} dV \quad (2.26)$$

$$\Phi_{\mathcal{M}} \stackrel{\text{def}}{=} \iint \mathcal{M} dA, \quad (2.27)$$

In order to verify whether certain mode has an OAM let us look at the time averages of the angular momentum flux  $\Phi_{\mathcal{M}}$ :

$$\langle \Phi_{\mathcal{M}} \rangle = \iint \langle \mathcal{M} \rangle dA \quad (2.28)$$

as well as the time average of the energy flux:

$$\langle \Phi_{\mathcal{W}} \rangle = \iint \frac{\langle \mathcal{S}_z \rangle}{c} dA. \quad (2.29)$$

Because of the symmetry of radial and axial components about the fiber axis, we note that the integration in Eq. 2.27 will leave only z-component of the angular

momentum density non zero. Hence:

$$\langle \mathcal{M} \rangle = \langle \mathcal{M} \rangle_z = \frac{1}{c^2} \vec{r} \times \langle \vec{\mathcal{E}} \times \vec{\mathcal{H}} \rangle_z. \quad (2.30)$$

Using Eq. 2.25 we derive:

$$\mathcal{M}_z = \frac{r}{c^2} \mathcal{S}_\phi, \quad (2.31)$$

and knowing  $\langle \mathcal{S} \rangle = \text{Re}\{\vec{S}\}$  and  $\mathbf{S} = \frac{1}{2}\mathbf{E} \times \mathbf{H}^*$  leads to:

$$S_\phi = \frac{1}{2}(-E_r H_z^* + E_z H_r^*), \quad (2.32)$$

$$S_z = \frac{1}{2}(E_x H_y^* - E_y H_x^*). \quad (2.33)$$

Let us now focus on a specific linear combination of the  $HE_{l+1,m}^{even}$  and  $HE_{l+1,m}^{odd}$  modes with  $\pi/2$  phase shift among them:

$$V_{lm}^+ = HE_{l+1,m}^{even} + iHE_{l+1,m}^{odd} \quad (2.34)$$

The idea for this linear combination comes from observing azimuthal dependence of the  $HE_{l+1,m}^{even}$  and  $HE_{l+1,m}^{odd}$  modes comprising  $\cos(\phi)$  and  $\sin(\phi)$ . If we denote the electric field of  $HE_{l+1,m}^{even}$  and  $HE_{l+1,m}^{odd}$  modes as  $\mathbf{e}_1$  and  $\mathbf{e}_2$ , respectively, and similarly, denote their magnetic fields as  $\mathbf{h}_1$  and  $\mathbf{h}_2$ , the expression for this new mode can be written as:

$$\mathbf{e} = \mathbf{e}_1 + i\mathbf{e}_2, \quad (2.35)$$

$$\mathbf{h} = \mathbf{h}_1 + i\mathbf{h}_2. \quad (2.36)$$

Using Eq. 5.3 - 5.6 for WGA, and expressions for  $HE_{l+1,m}^{even}$  and  $HE_{l+1,m}^{odd}$  modes in

Tables 2.1 - 2.3, we derive:

$$e_r = e^{i(l+1)\phi} F_l(R), \quad (2.37)$$

$$h_z = n_{co} \left( \frac{\epsilon_0}{\mu_0} \right)^{1/2} \frac{(2\Delta)^{1/2}}{V} G_l^- e^{i(l+1)\phi}, \quad (2.38)$$

$$e_z = i \frac{(2\Delta)^{1/2}}{V} G_l^- e^{i(l+1)\phi}, \quad (2.39)$$

$$h_r = -in_{co} \left( \frac{\epsilon_0}{\mu_0} \right)^{1/2} e^{i(l+1)\phi} F_l(R), \quad (2.40)$$

(note that  $\mathbf{e}$  and  $\mathbf{E}$  electric fields are related through Eq. 2.9). We note that all the quantities have  $\exp^{i(l+1)\phi}$  dependence that indicates these modes might have OAM, similarly to the free space case. Using Eq. 2.32 we derive azimuthal and the longitudinal component of the Poynting vector:

$$\mathcal{S}_\phi = -n_{co} \left( \frac{\epsilon_0}{\mu_0} \right)^{1/2} \frac{(2\Delta)^{1/2}}{V} \operatorname{Re}\{F_l^* G_l^-\}, \quad (2.41)$$

$$\mathcal{S}_z = n_{co} \left( \frac{\epsilon_0}{\mu_0} \right)^{1/2} |F_l|^2. \quad (2.42)$$

Using identities:

$$\frac{(2\Delta)^{1/2}}{V} = (\tilde{\beta}\rho)^{-1} \quad (2.43)$$

$$\operatorname{Re}\{F_l^* G_l^-\} = \frac{1}{2} \left( \frac{d|F_l|^2}{dR} \right) - \frac{l}{R} |F_l|^2 \quad (2.44)$$

the time-averaged angular momentum density becomes:

$$\langle \mathcal{M}_z \rangle = \frac{r}{c^2} \langle \mathcal{S}_\phi \rangle = -\frac{n_{co}}{c^2 \tilde{\beta}} \left( \frac{\epsilon_0}{\mu_0} \right)^{1/2} \left( \frac{R}{2} \frac{d|F_l|^2}{dR} - l |F_l|^2 \right). \quad (2.45)$$

Using integration by parts, and the fact that  $|F_l|^2 r^2 = 0$  at the beam's center ( $r = 0$ ), as well as  $\lim_{r \rightarrow 0} |F_l|r = 0$  for  $l \geq 1$  as a Bessel equation (2.18) solution (Watson,

1995), we write:

$$\iint \frac{R}{2} \frac{d|F_l|^2}{dR} dA = - \iint |F_l|^2 dA, \quad (2.46)$$

so the flux of angular momentum across the beam fiber profile can we written as:

$$\Phi_{\mathcal{M}} = \iint \langle \mathcal{M}_z \rangle dA = (l+1)n_{co} \left( \frac{\epsilon_0}{\mu_0} \right)^{1/2} \frac{1}{c^2 \tilde{\beta}} \iint |F_l|^2 dA, \quad (2.47)$$

and energy flux can be expressed as:

$$\Phi_{\mathcal{W}} = \int \frac{\langle \mathcal{S}_z \rangle}{c} dA = \frac{1}{c} n_{co} \left( \frac{\epsilon_0}{\mu_0} \right)^{1/2} \iint |F_l|^2 dA, \quad (2.48)$$

The ratio of the angular momentum flux to the energy flux therefore becomes:

$$\frac{\Phi_{\mathcal{M}}}{\Phi_{\mathcal{W}}} = \frac{l+1}{\omega}. \quad (2.49)$$

We note that in the free-space case, as derived by (Allen et al., 1992), this ratio is similar:

$$\frac{\Phi_{\mathcal{M}}}{\Phi_{\mathcal{W}}} = \frac{l+\sigma}{\omega}, \quad (2.50)$$

where  $\sigma$  represents the polarization of the beam and is bounded to be  $-1 < \sigma < 1$ . In our case, it can be easily shown that SAM of the  $V_{lm}^+$  state (Eq. 2.34), is 1, leading to important conclusion, that the OAM of the  $V_{lm}^+$  state is  $l$ . Hence, this concludes the proof that, in an ideal fiber, OAM mode exists.

Before discussing the conditions for the OAM mode stability, we note that  $V_{lm}^- = HE_{l+1,m}^{even} - iHE_{l+1,m}^{odd}$  state carries opposite SAM of  $s = -1$  and topological charge of  $l = -l$ . In addition, it can be shown that the linear combination of the  $EH_{l-1,m}^{even,odd}$  modes gives the similar results as Eq. 2.49, except the OAM and the SAM of these states are of the opposite signs. Finally, we note that the state comprised as a linear

combination of  $V_{lm}^+$  and  $V_{lm}^-$  states can have any value of topological charge between  $-l$  and  $+l$ , where  $l$  is not bounded, which in principle means that the OAM can be much larger than the SAM (that has boundary of  $\pm 1$ ). This fact has been used in several aspects in optical tweezers to impart a large torque on a particle (Curtis and Grier, 2003; Ladavac and Grier, 2004; Schmitz et al., 2006; Andrews, 2008).

### 2.3 Fiber mode coupling theory

Up to this point, we have analytically study an ideal scenario of perfectly symmetric fibers, assuming no longitudinal changes in the fiber profile. In a real fiber, random perturbations can induce coupling between spatial and/or polarization modes causing propagating fields to evolve randomly throughout the fiber. The random perturbations can be divided into two classes (Gloge, 1972): the first class is intrinsic and may include static and dynamic fluctuations throughout the longitudinal direction, such as the density and concentration fluctuations natural to random glassy polymer materials such are fibers; the second class contains extrinsic variations such as microscopic random bends caused by stress, diameter variations, and fiber core defects such as microvoids, cracks, or dust particles.

While mode coupling effects were first studied in the 70s when MMFs were predominantly used for optical communications (Marcuse, 1974; Gloge, 1972; Olshansky, 1975), recent developments in MDM optical communication systems (Sec. 1.1) revived their study. Mode coupling can be described by field coupling models (Ch.3 in (Marcuse, 1974)), which account for complex-valued modal electric field amplitudes, or by power coupling models (Ch.5 in (Marcuse, 1974)), which is a simplified description that accounts only for real-valued modal powers. Early MMF systems used incoherent light emitting diode sources, and power coupling models were used widely to describe several properties including steady-state modal power distributions and

fiber impulse responses (Raddatz et al., 1998; Pepeljugoski et al., 2003; Patel and Ralph, 2002). Though recent MMF systems use coherent sources, power coupling models are still used to describe effects such as reduced differential group delays in plastic MMFs (Garito et al., 1998).

By contrast, practical SMF systems have been using laser sources. The study of random birefringence and mode coupling in SMF, which leads to polarization-mode dispersion (PMD), uses field coupling models, which predict the existence of principal states of polarization (PSPs) (Gordon and Kogelnik, 2000; Poole and Wagner, 1986). PSPs are polarization states shown to undergo minimal dispersion, and are used for optical compensation of PMD in direct-detection SMF systems (Noe et al., 1999). In recent years, field coupling models have been applied to MMF, predicting principal modes (PMs) (Shemirani et al., 2009; Fan and Kahn, 2005), which are the basis for optical compensation of modal dispersion in direct-detection MMF systems (Chen et al., 2011). Statistical models that investigate influence of modal dispersion and mode dependant loss and gain, on MDM systems have been also extensively studied (Ho and Kahn, 2011; Ho and Kahn, 2012; Shemirani and Kahn, 2009).

Mode coupling can be classified as weak or strong, depending on whether the total system length is comparable to, or much longer than, a length scale over which propagating fields remain correlated (Ho and Kahn, 2012). Depending on the detection format, communication systems can be divided into direct and coherent detection systems. In direct-detection systems, mode coupling must either be avoided by careful design of fibers and modal de(multiplexers) (Ryf et al., 2012), and/or mitigated by adaptive optical signal processing (Carpenter and Wilkinson, 2012a). In systems using coherent detection, any linear crosstalk between modes can be compensated by multiple-input multiple-output (MIMO) digital signal processing (DSP) (Randel et al., 2011), but DSP complexity increases with an increasing number of modes.

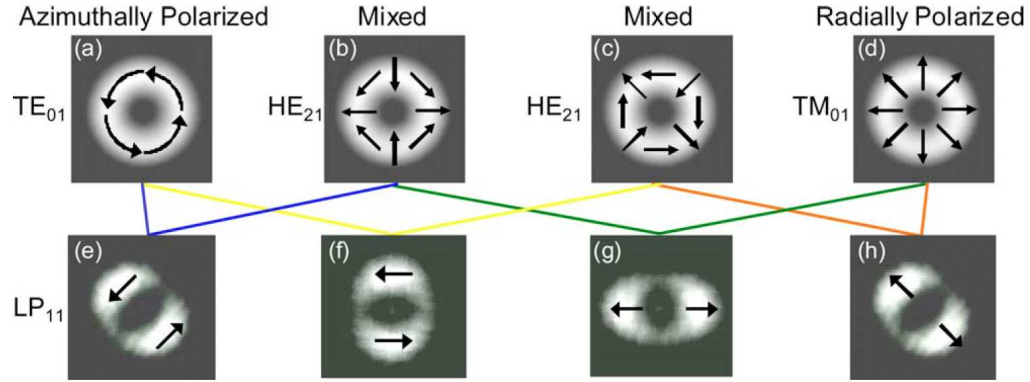


**Figure 2.3:** Intensity patterns of the first-order mode group in vortex fiber. Arrows show the polarization of the electric field. The top row shows vector modes that are the exact vector solutions of the Eq. 2.18, while the bottom row shows the resultant, unstable  $LP_{11}$  modes commonly obtained at a fiber output. Specific linear combinations of pairs of top row of modes, resulting in the variety of  $LP_{11}$  modes obtained at a fiber output, are shown by colored lines (Ramachandran et al., 2009). With permission from (Ramachandran et al., 2009). © OSA.

The idea of reducing DSP complexity by using MIMO only within mode groups that have nearly degenerate propagation constants exist, but have so far failed to produce results (Ryf et al., 2012).

Typical index separation of the two polarizations in SMF is on the order of  $10^{-7}$  (Galtarossa et al., 2000). While this small separation lowers the PMD of the fiber, external perturbations can easily couple one mode into another, and indeed, in SMF, arbitrary polarization is typically observed at the output. Simple fiber polarization controller, that uses stress induced birefringence, can be used to achieve any desired polarization at the output of the fiber.

By the origin, mode coupling can be classified as distributed (caused by random perturbations in fibers), or discrete (caused at the modal couplers and (de)multiplexers). Most importantly for us, it has been shown by (Gloge and Marcatili, 1973) that small effective index separation among higher order modes, is the main reason for

mode coupling and mode instabilities. In particular, the distributed mode coupling has been phenomenologically shown to be inversely proportional to  $\Delta n_{eff}^{-p}$ , with  $p > 4$  depending on coupling conditions (Olshansky, 1975). As we saw in the Sec. 2.1, modes within one group are degenerate (Fig. 2·1). For this reason, in most MMFs, modes that are observed at the fiber output are in fact the linear combinations of the vector modes, and are linearly polarized (*LP*) states (Fig. 2·3). Hence, OAM modes, that are the linear combination of the  $HE_{21}^{even,odd}$  modes, can not coexist in these fibers due to coupling to degenerate  $TE_{01}$  and  $TM_{01}$  states. On the other side, the phenomenological law above (Olshansky, 1975), indicates that strong, exponential reduction in mode coupling can be obtained with  $\Delta n_{eff}$  increase among modes (an example of the desired solution is shown on Fig. 2·4 B).

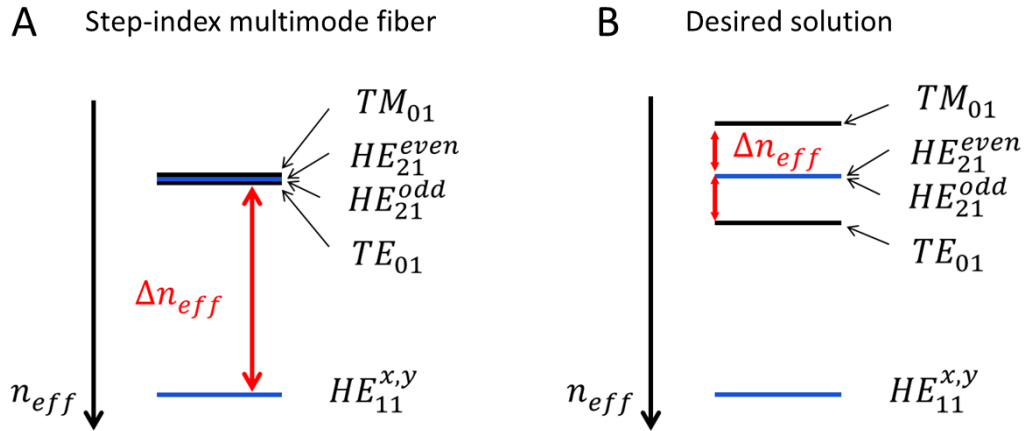


**Figure 2·4:** Concept of effective index separation in the first-order modes. (A) Typical step-index MMF does not exhibit effective index separation causing mode coupling. (B)  $n_{eff}$  separation caused by desired fiber index profile.

In addition to effective index separation, mode coupling also depend on the strength of the perturbation. Increase in cladding diameter can help reduce the bend-induced perturbations in the fiber (Blake et al., 1986; Blake et al., 1987). Special fiber design that includes the trench region can achieve so-called bend insensitivity, which

is a predominant fiber-to-the-home today. The design. Fiber design that demonstrates reduced bend insensitivity of higher order Bessel modes for high power lasers have been demonstrated (Ramachandran et al., 2008). Most importantly, and we'll see in the next chapter, a special fiber design can remove the degeneracy of the first-order modes, hence, reducing the mode coupling, end enabling the OAM modes to propagate in these fibers.

## Chapter 3

# Vortex Fiber

As we mentioned in Sec. 2.3, coupling between modes in MMFs restricts OAM mode (Eq. 2.34) propagation to short fiber length on the order of tens of centimeters (McGloin et al., 1998; Wong et al., 2012; Dashti et al., 2006). The main reason for the mode instabilities is the small effective index separation among higher order modes (Olshansky, 1975; Ramachandran et al., 2009). In this chapter we describe a class of specialty fibers, introduced by Ramachandran et al. (Ramachandran et al., 2009), that we study in detail in this and all subsequent chapters. We first briefly introduce the reasoning behind untypical refractive index profiles in these fibers, called vortex fibers henceforth. We then numerically solve the vector wave equation (Eq. 2.3) to obtain fiber modal properties such as effective and group indices, dispersion and effective area. We then present experimental findings for effective and group indices indicating good agreement with numerical solutions. Both of these findings show large mode separation, several orders of magnitude higher than in conventional fibers, indicating reduced mode coupling according to the theory (Sec. 2.3). At the end of this chapter, using developed imaging setup, we indeed show that OAM states can be created in vortex fibers, and our qualitative analysis indicate high purity of these states.

### 3.1 Introduction

As a few-mode fiber, vortex fiber was first introduced to create cylindrical vector beams represented by  $TE_{01}$  and  $TM_{01}$  modes (also known as polarization vortices) (Ramachandran et al., 2009). Unlike step-index few mode fibers, where groups of higher order modes are degenerate i.e. have the same effective indices (Sec. 2.1), the vortex fiber removes the degeneracy within a family of higher order modes (HOMs). This is achieved by recognizing the refractive index profile that increases polarization correction coefficients  $\delta\beta$  (Table 2.3) and Eq. 2.22). In particular, if we focus on the first order ( $l = 1$ ) HOM family, comprising  $TE_{01}$ ,  $HE_{21}^{even}$ ,  $HE_{21}^{odd}$  and  $TM_{01}$ , we note that  $\delta\beta$  of these modes are 0,  $I_1 - I_2$  and  $2(I_1 + I_2)$  for the  $TE_{01}$ ,  $HE_{21}^{even,odd}$  and  $TM_{01}$ , respectively. In essence, the design of the vortex fiber aims to maximize the separation of these modes by maximizing both fields and field gradients (( $F_l(R)$  and  $\frac{dF_l(R)}{dR}$  in Eq. 2.22)). As we discussed in Sec. 2.3, this separation reduces mode coupling exponentially, and indicates that the two  $l = \pm 1$  OAM modes, will exist in a more stable manner than in conventional step-index multimode fibers, as the coupling to  $TE_{01}$  and  $TM_{01}$  modes will be reduced.

Having described the idea behind the vortex fiber, we briefly introduce the nomenclature used. Vortex fibers with cladding diameters from  $80\mu m$  to  $160\mu m$  in  $5\mu m$  steps were available for our experiment. These fibers were all drawn from the same preform with the ID 'dk110127' (where 'dk' is short for Denmark and '110127' indicates the date the preform was made). Since we have been dealing with mostly one preform, sometimes we will use shorter notation 'dk11'). The preform was made using an industry standard modified chemical vapor deposition (MCVD) method, which is then used to create fibers with different cladding diameters. For a review on fiber manufacturing techniques, we recommend (Wang et al., 2006). Since the fibers were drawn from the same preform, different cladding sizes correspond to the different core sizes

too. The nomenclature we use for different sizes is, for example, OD100, where 'OD' stands for the outer (cladding) diameter of  $100\mu\text{m}$ .

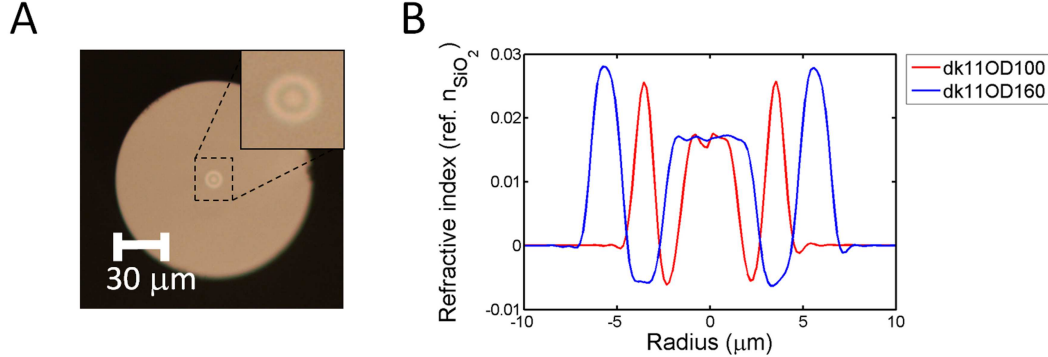


**Figure 3.1:** (A) An optical microscope image of the end facet of the vortex fiber dk11OD100. (B) Measured fiber refractive index for the dk11OD100 and dk11OD160.

An optical microscope image (Fig. 3.1 A) shows a qualitative image of the cleaved end-face of a dk11OD100 vortex fiber. The figure inset shows the fiber core region surrounded by a ring region. Figure 3.1B shows the measured refractive index profile (Interfiber Analysis IFA-100) of the vortex fibers dk11OD100 and dk11OD160. We note that the measured refractive index profiles for different vortex fiber diameters have similar values, approximately scaled by the ratio of OD, indicating that drawing the preform at different speeds had little impact on the index profile.

### 3.2 Numerical analysis

In order to study the modal properties of vortex fibers, we use a finite difference method based software (Pedersen et al., 2011) (courtesy of Martin Pedersen) to numerically solve vector wave equation (Eq. 2.3) for the vortex fiber OD105 profile we have measured. In addition, we used another finite difference method to solve the scalar wave equation (Eq. 2.13) for the same vortex fiber. The results for the fundamental and one of the higher order modes were compared in the both cases (Fig.

3·2). We note that the mode profiles are almost identical, leading to conclusion that vortex fiber satisfies the WGA.

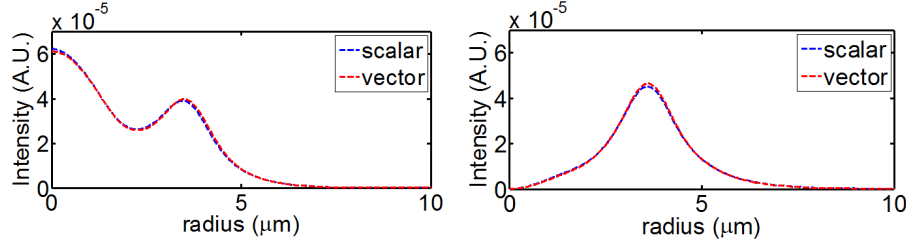


**Figure 3·2:** Comparison of the simulated fields using scalar and vector numerical method for the dk11OD105 fiber case.

Finite difference method we used, in essence, assumes circular symmetry of a waveguide and samples differential vector wave equation for magnetic field (Eq. 2.3) at desired number of equally spaced points,  $N$ , (in our case  $N > 1000$  gives consistent result). This produces difference equations tractable for computation. For a given fiber profile input, the solutions in terms of effective indices and 1D field profiles of the modes are obtained. Example simulation results for dk11OD105 are shown in Fig. 3·3. The vortex fiber property of mode separation can be clearly seen in Fig. 3·3 B. Separation of  $\approx 3 \times 10^{-3}$  (at 1550nm) with respect to the fundamental ( $HE_{11}$ ) mode was calculated, as well as separation of  $\approx 1.1 \times 10^{-4}$  between nearest neighbor first order modes. Numerically calculated mode profiles are shown in Fig. 3·3 C-D. Note that fundamental mode does not have a typical profile as in the case of the step-index fiber; instead its Gaussian-like. The  $HE_{21}$  mode intensity profile resembles a doughnut-shape due to refractive index ring structure. In addition to OD105, we show that dk11OD160 also guides  $l \leq 3$  modes (Fig. 3·4).

Let us examine the properties of all fiber ODs, concentrating on the significant telecom wavelength of 1550nm. Figure 3·6 shows which modes are guided with effective index differences ( $\Delta n_{eff}$ ) calculated for first higher order modes (Fig. 3·5). These figures reveal two important observations. First, we note that the difference

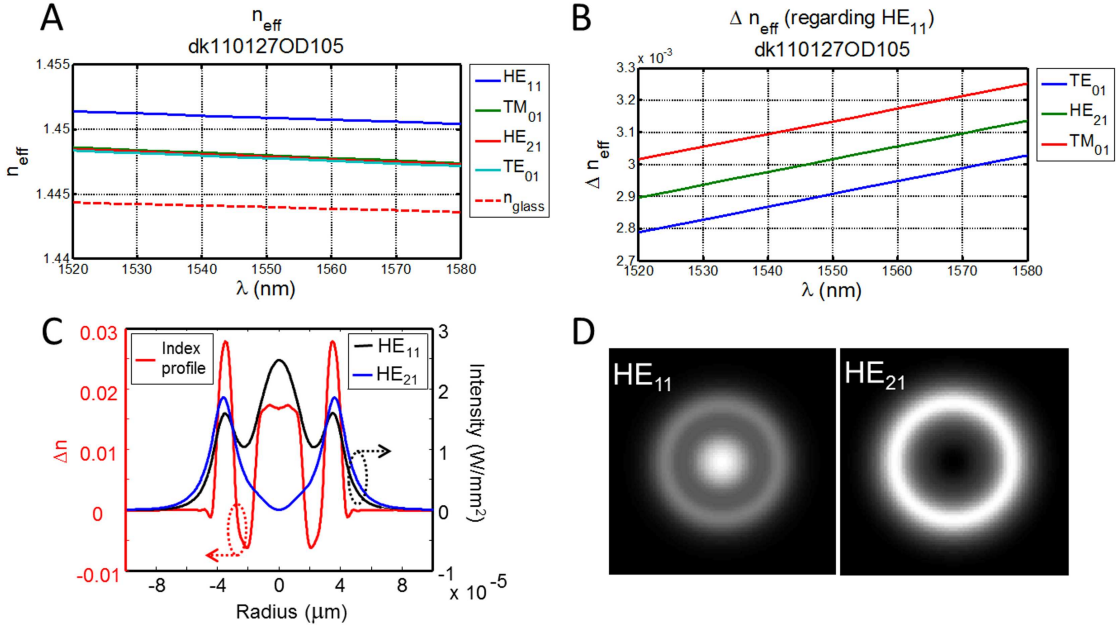


**Figure 3.3:** Numerically calculated properties of the dk11OD105 vortex fiber. Separation of  $n_{\text{eff}}$  indicates potential for smaller mode coupling (A-B). Mode profiles in 1D and 2D case (C-D), latter obtained from the 1D profiles assuming circular symmetry. Polarization at certain points can be also obtained assuming azimuthal dependence of the modes (Table 2.3).

between  $l = 0$  and  $l = 1$  modes decreases with OD, implying more mode mixing between these two modes with OD increase (Sec. 2.3) (Fig. 3.5 A). Second, we see that the  $\Delta n_{\text{eff}}$  among first-order modes follows the opposite trend (Fig. 3.5 B-C) and  $\Delta n_{\text{eff}}$  increases with OD increase (with maximum around OD130-140). This qualitatively implies a trade-off among coupling to fundamental mode and coupling to TE/TM modes (also note a scale differences in the two graphs). However, table of guided modes for all ODs indicate the existence of higher order modes for fibers with  $OD > 105\mu\text{m}$  (Fig. 3.6). Therefore, it is reasonable for now to speculate that the mode coupling will be statistically higher in larger ODs as the number of available states becomes larger. We note that no decisive conclusion can be made yet however based on these simulations.

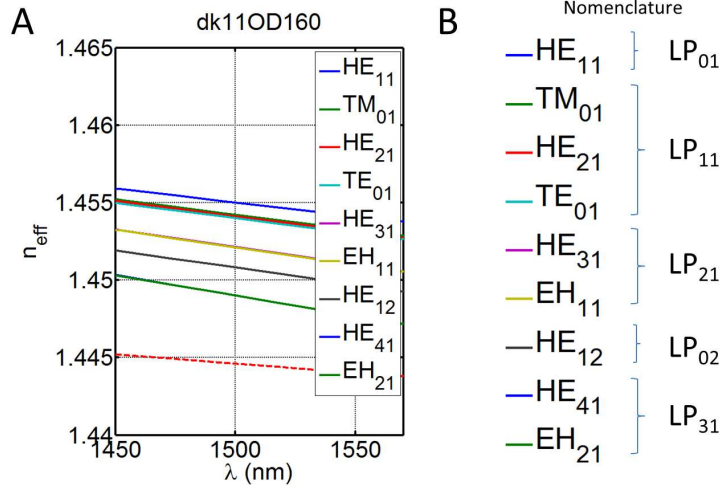


**Figure 3.4:** (A) Effective indices for guided modes for the dk11OD160 vortex fiber. (B) Corresponding LP notation designating certain groups of modes.

Before we move onto the experimental part, we briefly want to note few physical quantities that can be derived using the calculated effective indices, namely group index ( $n_g$ ), group velocity dispersion (GVD) and effective area ( $A_{\text{eff}}$ ) (Agrawal, 2010):

$$n_g \stackrel{\text{def}}{=} n_{\text{eff}} - \lambda \frac{dn_{\text{eff}}}{d\lambda}, \quad (3.1)$$

$$GVD \stackrel{\text{def}}{=} -\frac{\lambda}{c} \frac{d^2 n_{\text{eff}}}{d\lambda^2}, \quad (3.2)$$

$$A_{\text{eff}} \stackrel{\text{def}}{=} \frac{\left( \int |E|^2 dA \right)^2}{\int |E|^4 dA} = \frac{\left( \int I dA \right)^2}{\int I^2 dA}, \quad (3.3)$$

where  $c$  is the speed of light in vacuum,  $\lambda$  is wavelength,  $E$  is 2D electrical field profile and the integral in Eq. 3.3 is over the fiber cross-section area. The wavelength dependance of the three quantities for dk11OD105 is given in Fig. 3.7. We note that GVD and  $A_{\text{eff}}$  of the  $HE_{11}$  mode in vortex fiber are similar to the properties of its SMF counterpart (typical SMFs used for optical communications have  $A_{\text{eff}}$  of the order of  $100 \mu\text{m}^2$ , some large mode area fibers above  $1000 \mu\text{m}^2$  and some photonic crystal fibers below  $10 \mu\text{m}^2$ ).

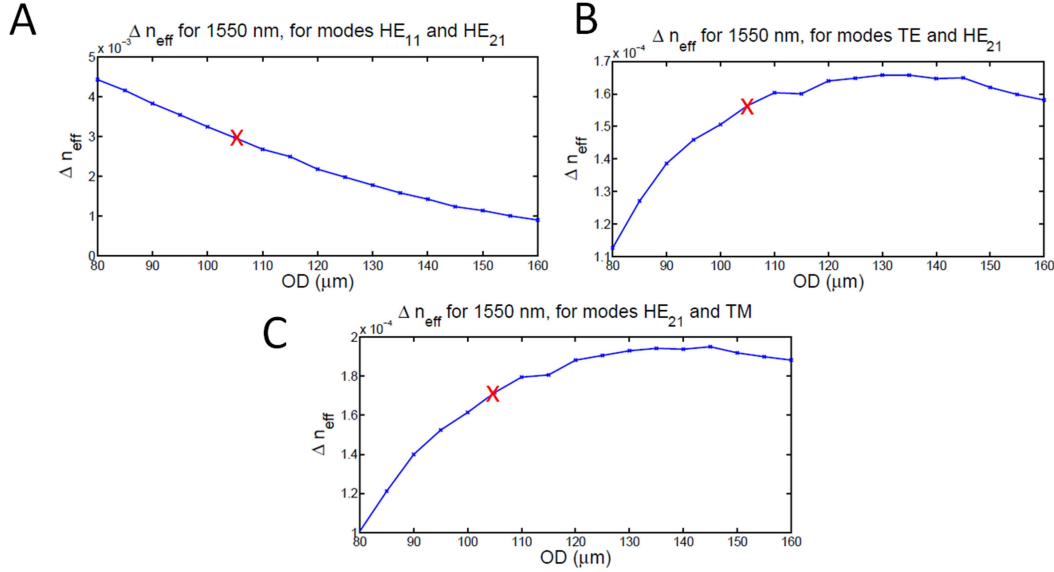


**Figure 3.5:** Effective index difference (also called mode separation) versus fiber OD between different modes.

	OD	80	85	90	95	100	105	110	115	120	125	130	135	140	145	150	155	160
$\text{LP}_{11}$																		
$\text{LP}_{21}$																		
$\text{LP}_{02}$																		
$\text{LP}_{31}$																		

**Figure 3.6:** Table of guided modes for different OD fibers, at 1550nm. OD105 offers largest diameter fiber for which  $l \geq 2$  modes are cut off.

### 3.3 Experimental measurements

In this section we experimentally measure some of the vortex fiber properties that we numerically calculated in the previous section. Our experimental setup and methods will be explained in detail in Ch. 4, and here we focus only on results.

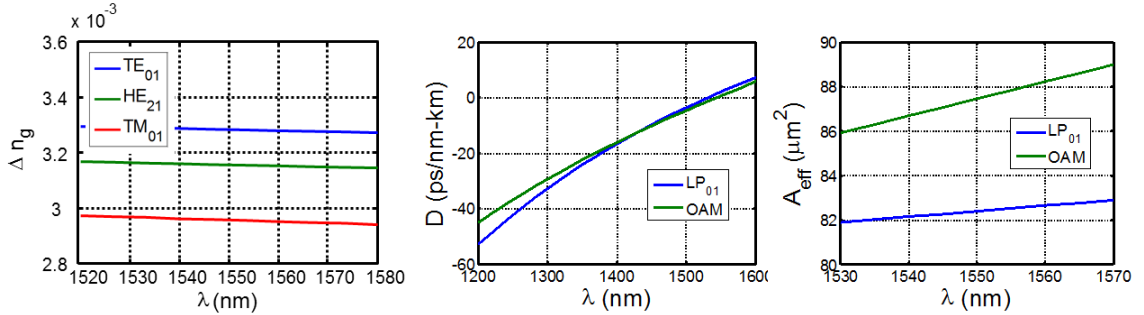


**Figure 3.7:** Numerically calculated properties of the dk11OD105 vortex fiber

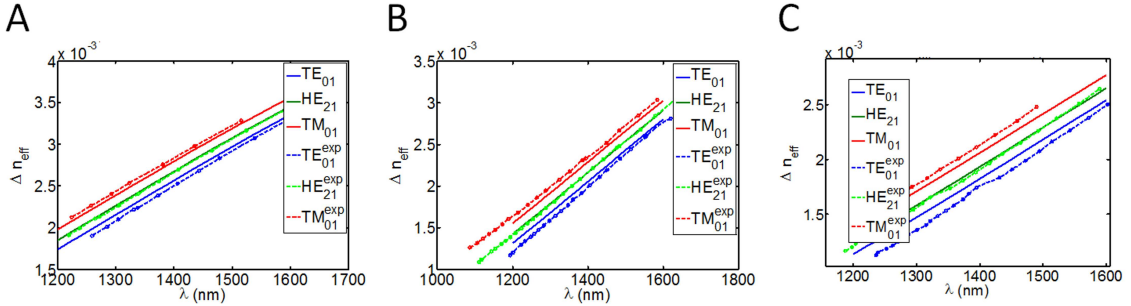


**Figure 3.8:** Measured and numerically calculated  $\Delta n_{eff}$  with respect to the  $HE_{11}$  mode for (A) OD100, (B) OD110 and (C) OD115 vortex fibers.

### 3.3.1 Effective and group indices

The results of the measured effective indices for the three different ODs are shown in Fig. 3.8, and are in relative good agreement with numerical results (juxtaposed on the graph). We do note some difference between two results (on the order of 10 – 20%) especially as we go to the higher ODs (Fig. 3.8 A-C). To understand this, we'll need the knowledge of mode conversion methods that we use (4.1). Namely, our mode conversion method requires that stress is applied onto the vortex fiber, on the order of 1kg. We believe that this stress, which increases with ODs as measured, induces geometrical changes in the fiber that break down the cylindrical symmetry

assumption under which numerical results have been obtained (Smith, 1980; Golowich and Ramachandran, 2005).

In addition to  $\Delta n_{eff}$ , group index difference ( $\Delta n_g$ ) has also shown a good agreement between the numerically calculated and measured values (Fig. 3.9) (see Sec. 4.1 for measurement details).

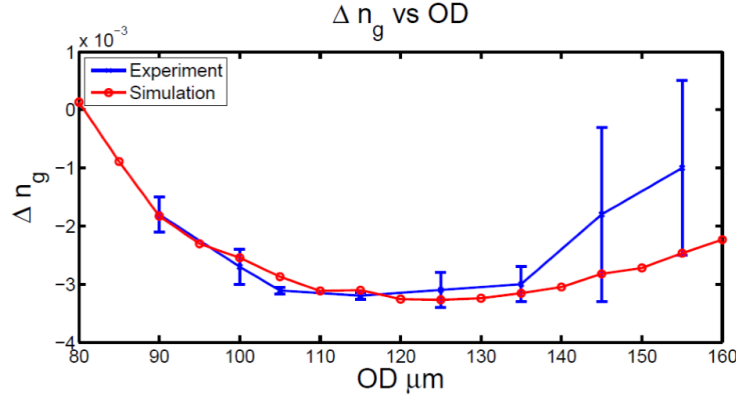


**Figure 3.9:** Group index difference among  $HE_{11}$  and  $HE_{21}$  vortex fiber modes for several different OD.

### 3.3.2 Loss

Power loss in fibers can be caused by material absorption, linear and nonlinear scattering, macrobend and microbend losses (Smink et al., 2007). The measurement procedure compared transmission power readings for different fiber lengths. Small insertion loss (<0.1dB) can typically occur at the splices, especially for large ODs, due to modal mismatch. In the case of dk11OD105 we measured loss of  $1.3 \pm 0.1$  dB/km for  $HE_{11}$  mode, and  $1.6 \pm 0.1$  dB/km for  $HE_{21}$  (similar losses were observed for different fiber ODs). The estimated 0.1dB/km error in the measurements comes from power oscillations caused by distributed mode coupling (using bubble wrap to thermally isolate helps stability timewise). Loss between  $HE_{11}$  and  $HE_{21}$  modes (also called modal differential loss or excess loss (Olshansky and Nolan, 1976)) was measured to be  $0.33 \pm 0.1$  dB/km (Fig. 3.10. This effect is predicted theoretically and can

be explained by mode coupling theory where perturbations have longitudinal spatial frequencies below the range required for mode coupling (Olshansky and Nolan, 1976). We leave the detailed study of this effect for the future work.

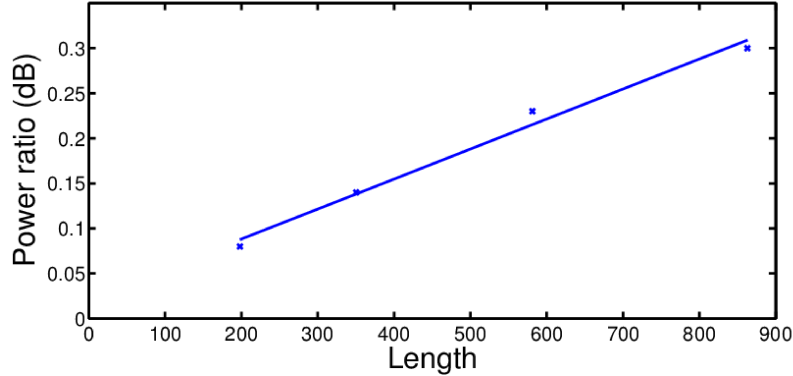


**Figure 3.10:** Transmission power difference (in dB) between  $HE_{21}$  and  $HE_{11}$  modes showing linear dependence of the loss in length. Gradient of the fit 0.33 dB/km gives the excess (i.e. differential) loss between the two modes.

### 3.3.3 Mode imaging

So far we have presented properties of the vortex fiber that show, numerically and experimentally, the effective index separation of the modes. These results suggest that OAM modes can exist in a vortex fiber. In order to verify that this is indeed the case, we designed a setup for imaging both the intensity and the phase of the output of the vortex fiber (Bozinovic et al., 2011b) (Fig. 3.11). A typical intensity image is shown in Fig. 3.12 A, along with the OAM mode intensity profile along the ring (Fig. 3.12 B). We note some intensity variations, that indicate interference between multiple modes 3.12A. In Ch. 5 we explain a method that quantifies these variations to find the relative mode contributions. In order to observe the phase of the beam, a reference beam was introduced 3.11, and interference was observed in the case of: slightly diverging fundamental ( $LG_{01} \sim e^{i\rho^2}$ ) mode (Fig. 3.12 C) and

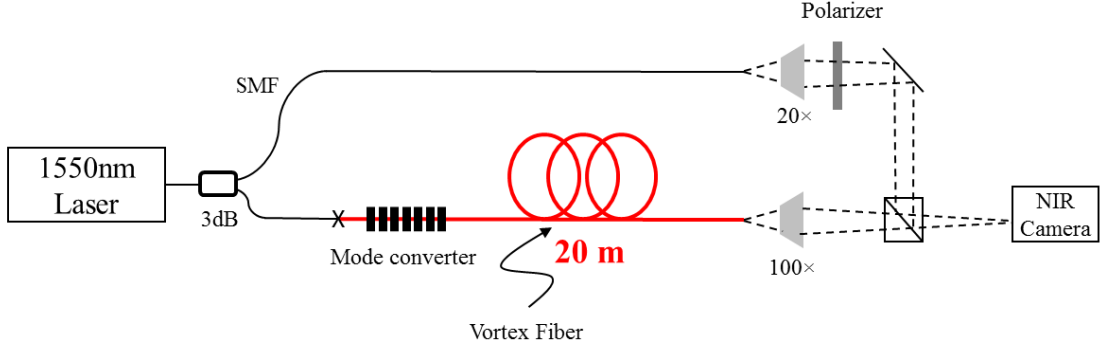


**Figure 3·11:** Setup for OAM mode imaging. This setup enables us to measure both the intensity and the phase of the beam.

a tilted plane wave  $E = e^{ik_xx}$  (Fig. 3·12 D). As we showed previously (Ch. 2), the OAM modes have distinct  $\exp(il\phi)$  phase. Using simple calculations for these two interference cases, the intensity distribution in the image plane can then be written simply as:

$$I_1(\rho, \phi) \sim |e^{il\phi} + e^{i\rho^2}|^2 = 2 + 2\cos(l\phi + \rho^2), \quad (3.4)$$

$$I_2(\rho, \phi) \sim |e^{il\phi} + e^{ik_xx}|^2 = 2 + 2\cos(l\phi + k_xx). \quad (3.5)$$

The two patterns are plotted in Fig. 3·12 E-F are called spiral and fork patterns respectively (and have been ubiquitous in OAM related literature (Andrews, 2008)). The features of the simulated and measured patterns match well, confirming the existence of the OAM modes at the fiber output (Fig. 3·12).

Finally, we compare the observed and numerically calculated mode profiles and observe good agreement (Fig. 3·13 shows the case of OD100). This observation indicates that numerical model that we used is to the great extent good approximation of the measured values, and allows easy scaling to other OD values.

With this we proceed in the next chapter with the detailed explanation of the mode conversion methods that we used in Fig. 3·11, as well as with the explanation

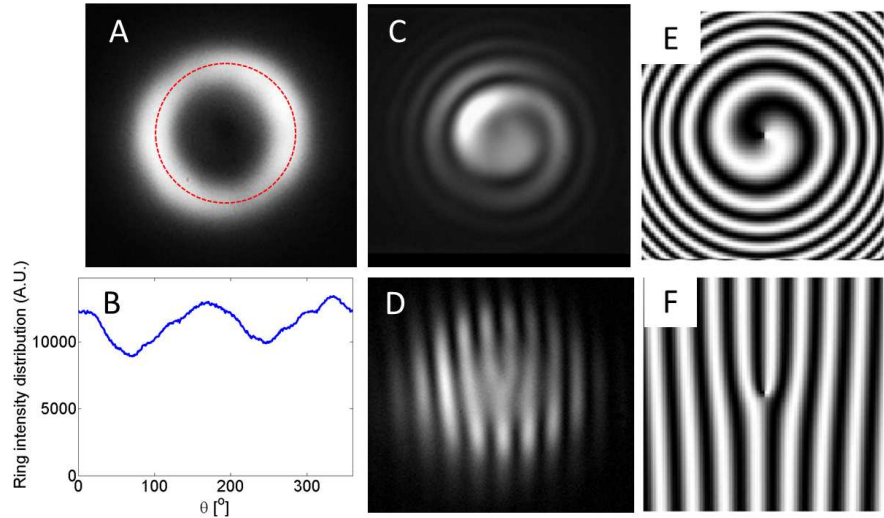


**Figure 3.12:** (A) OAM mode intensity profile and (B) a line profile along the ring. (C,D) Observed interference patterns between the OAM mode and the reference beam when the two beams are (C) collinear or (D) form an angle . (E,F) Simulated interference patterns in the two cases.

of the effective and group index measurements (Fig. 3.8 and 3.9). Later in Ch. 5 we develop methods for quantifying the modal purity that will give us better insight into the vortex fiber properties.

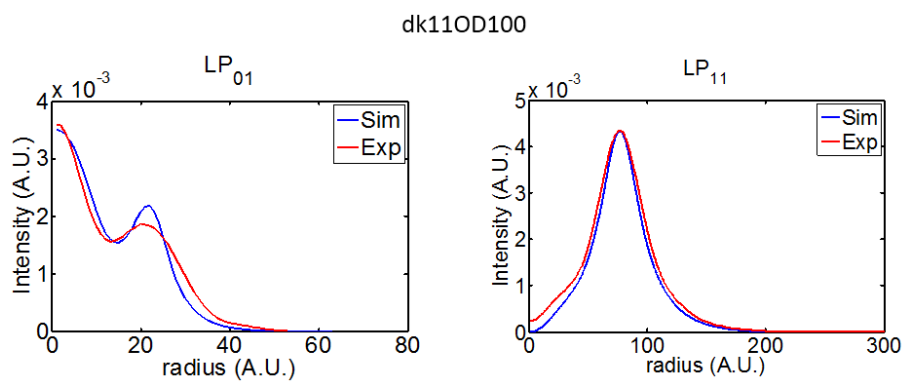


**Figure 3.13:** Comparison of the simulated and imaged mode profiles for OD100 case.

## Chapter 4

# OAM Generation in Vortex Fiber

Most of the conventional light sources, coherent or incoherent, emit light in a fundamental mode ( $LG_{00}$ ) and conversion to HOM is needed in order to create an OAM beam. Methods that use phase plates (Khonina et al., 1992), cylindrical lenses (Padgett et al., 1996), computer generated holograms (He et al., 1995), fiber gratings (McGloin et al., 1998), q-plates (Karimi et al., 2012), specialty phase plates (Berkhout et al., 2010) and photonic integrated structures (Cai et al., 2012) have been proposed.

In this chapter, we study two of these methods for OAM generation, based on:

- fiber gratings, specifically:
  - microbend gratings (Hill et al., 1978),
  - carbon-dioxide ( $CO_2$ ) laser induced gratings (Poole and Presby, 1995), and
- computer generated holograms, using liquid-crystal-on-silicon (LCoS) spatial-light-modulators (SLM) (Ebihara et al., 1992).

While fiber grating methods have the advantage of mode conversion inside the fiber, allowing easier device packaging and flexibility, hologram-based free-space coupling methods have the advantage of allowing multiplexing, i.e. simultaneous coupling of several beams.

## 4.1 Fiber Gratings

Following the success of diffraction gratings for distributed feedback lasers (Kogelnik and Shank, 1972), first fiber gratings were introduced in 1978 (Hill et al., 1978). Fiber gratings were used as mirrors, in which a forward-propagating mode guided by the fiber core couples to a backward-propagating mode of the same type (Meltz et al., 1989), and as mode converters, in which one type of guided core mode couples to a different type (Hill et al., 1990; Poole et al., 1990). The fiber gratings were also used as loss filters, by enabling the guided core mode to couple to radiation modes (Mizrahi and Sipe, 1993) or for creating cladding modes, in the case where cladding is surrounded by a medium with a refractive index lower than that of the glass, such as air (Vengsarkar et al., 1996).

Applications of few-mode fiber gratings include dispersion control, signal power management, switching and routing, polarization control and sensing (Ramachandran, 2005). Based on the mode of operation, namely reflection or transmission mode, fiber gratings can be classified into Bragg gratings and long-period gratings (LPGs), respectively. In practice, LPG grating periods are usually on the order of a millimeter (with typical lengths on the order of tens of millimeters), while Bragg gratings have periods on the order of micron (Kashyap, 2008). Since we are interested in mode conversion in transmission mode, here we focus on studying LPGs only.

Several methods to generate fiber gratings include photosensitive methods such as UV-laser illumination in Ge-doped fibers (Meltz et al., 1989), microbend gratings (Blake et al., 1986) and  $CO_2$  laser induced gratings (Poole and Presby, 1995; Davis et al., 1998; Abrishamian et al., 2012)). Here, we focus on microbend and  $CO_2$  gratings as these produce anti-symmetric gratings (defined in the next section). The biggest difference between these two methods is that microbend gratings are not permanent and are easily tunable (on the order of seconds) in terms of their period

and length, while  $CO_2$  laser gratings are permanent and therefore non-tunable (mainly offering much easier packaging and deployment).

#### 4.1.1 Long period grating theory

The theory of fiber LPGs has been extensively studied (Hill et al., 1990; Poole et al., 1990; Vengsarkar et al., 1996; Erdogan, 1997b; Erdogan, 1997a; Hwang et al., 1999; Savin et al., 2000; Li et al., 2001) and relies on a coupled-mode theory (Marcuse, 1974), applied in cylindrically symmetric waveguides (such as fibers). In the general case (also called asynchronous coupling), two co-propagating modes with the propagation constants  $\beta$  will have the powers  $P_1$  and  $P_2$  after the grating of length  $L_g$  and period  $\Lambda$ :

$$\frac{P_2}{P_1} = (\kappa_g L_g)^2 \operatorname{sinc}^2(\sqrt{\kappa_g^2 + \delta^2} L_g), \quad (4.1)$$

where  $\delta$  is a detuning parameter:

$$\delta(\lambda) = \frac{1}{2}(\beta_1 - \beta_2) - \frac{\pi}{\Lambda}, \quad (4.2)$$

and  $\kappa_g$  defines the grating strength through a perturbation overlap integral:

$$\kappa_g = \int \vec{E}_1(\vec{r}) P(\vec{r}) \vec{E}_2^*(\vec{r}) d\vec{r}, \quad (4.3)$$

where  $P(\vec{r})$  represents the perturbation and  $E(\vec{r})$  electric fields of the two modes. In the special case when  $\delta = 0$  (the so-called phase-matching condition), complete (100%) mode conversion is theoretically achievable:

$$\beta_2 - \beta_1 = \frac{2\pi}{\Lambda}, \quad (4.4)$$

Note that detuning parameter  $\delta$  depends on the wavelength, hence grating mode conversion described by Eq. 4.1 is also wavelength dependant (we'll verify this ex-

perimentally in the next section).

In the case of the vortex fiber, we are interested in a perturbation that can couple fundamental  $HE_{11}$  modes into OAM modes (comprising  $HE_{21}^{even,odd}$  modes as we saw in Ch. 2). For this mode conversion, an antisymmetric grating i.e. the one for which perturbation that has a functional form of  $P(\vec{r}) \propto \cos(\phi)$ , needs to be used (an example of these gratings are microbend (Blake et al., 1986) and  $CO_2$  laser induced gratings (Davis et al., 1998)). By looking at the functional form of the  $HE_{21}^{even,odd}$  modes (Tables 2.1-2.3), we note that they have  $\cos(\phi)$  and  $\sin(\phi)$  dependance. Using following identities:

$$\int_0^{2\pi} \cos^2(\phi) d\phi = \pi \quad \int_0^{2\pi} \cos(\phi) \sin(\phi) d\phi = 0, \quad \int_0^{2\pi} \sin^2(\phi) d\phi = \pi,$$

it can be shown that overlap integral Eq. 4.3 is non-zero only for pairs of modes:  $(HE_{11}^x, HE_{21}^{even})$  and  $(HE_{11}^y, HE_{21}^{odd})$ . This reveals that for the phase matching condition  $\delta = 0$  and  $\kappa_g L_g = \pi/2$ , the  $HE_{11}^x$  mode will convert into  $HE_{21}^{even}$  and  $HE_{11}^y$  into  $HE_{21}^{odd}$ . Hence, a circular polarization at the grating input ( $HE_{11}^x + iHE_{11}^y$ ) will convert into OAM mode at the grating output ( $OAM_{11}^+ = HE_{21}^{even} + iHE_{21}^{odd}$ ), and that can be achieved using a simple polarization controller. We note that Eq. 4.1 describes power immediately after the grating, and considers only the ideal case. As we mentioned in Sec. 2.3, real fiber twists and bends can cause perturbations that couple one OAM state to the other OAM state of opposite helicity.

#### 4.1.2 Microbend gratings

As we mentioned, in the case of the microbend grating, the perturbation is created by geometrical changes of the fiber. A convenient realization of microbend LPGs uses a metallic block with grooves, that is pressed against the fiber (pressure lies in the range of equivalent to a mass of 500g to 3kg (Savin et al., 2000). In our case, several

specially designed metallic blocks with various groove periods  $\Lambda_0$  (ranging  $300\mu m$  to  $1000\mu m$ ) were built, with a stress measuring gauge. In order to achieve different grating periods it is then sufficient to rotate the block with respect to the fiber, in which case the grooves form a certain angle,  $\theta$ , with the straight-held fiber, and the period becomes  $\Lambda = \Lambda_0/\cos(\theta)$ .

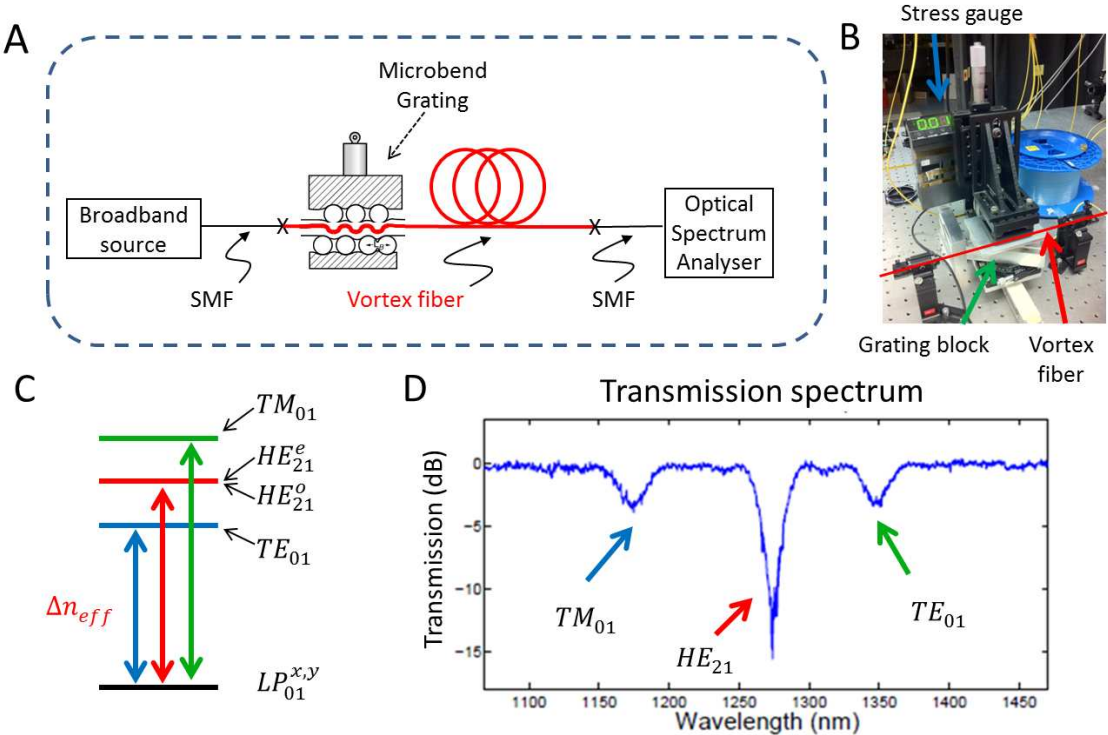


**Figure 4.1:** Microbend gratings. **(A)** Mode conversion setup. **(B)** Picture of the microbend grating. **(C)** Effective indices of modes supported by the vortex fiber (also see 3.8). Microbend grating period can be tuned to allow for mode conversion from  $HE_{11}$  to first-order modes (denoted by arrows).

A transmission setup that can monitor mode conversion across a wide range of wavelengths was built (Fig. 4.1 A). In the setup, the light from the broadband source (tungsten-halogen lamp) is guided through a single mode fiber (SMF) into the vortex fiber onto which grating was applied. The vortex fiber is then spliced onto

a second SMF whose output is connected to an optical spectrum analyzer (OSA). If the phase matching condition is satisfied at the grating, any higher order mode that is created in the vortex fiber will not be guided into the second SMF, and a dip in intensity transmission will occur in the OSA spectrum (also called resonance, or loss transmission spectrum). A typical spectrum acquired in the case of vortex fiber is shown in Fig. 4·1 D. Knowing that the vortex fiber splits the effective indices of the first-order modes (Fig. 4·1 C), we observe three resonant dips that satisfy phase matching conditions for the  $TM$ ,  $HE_{21}$  and  $TE$  modes. The maximum conversion is achieved when  $\Lambda = \frac{\lambda}{\Delta n_{eff}}$  for desired modes, where  $\Delta n_{eff}$  corresponds to difference between  $HE_{11}$  and  $TM_{01}$ ,  $HE_{21}$  and  $TE_{01}$  modes. This measurement was the basis for the  $\Delta n_{eff}$  measurement presented in Fig. 3·8. Note that the bandwidth of the incoherent broad band source that we use is so large ( $> 500nm$ ) that the light at the grating input is unpolarized (for the same reason the light from incandescent sources is unpolarized) . This means that one polarization, which contributes to the half of the beam, converts to the  $TM_{01}$  and  $TE_{01}$  modes, while the other half stays unconverted. This reasoning explains why the  $TM_{01}$  and  $TE_{01}$  resonances appear only 3dB strong. In the case of the  $HE_{21}$  resonance, both polarizations will undergo conversion into the degenerate  $HE_{21}^{even,odd}$ , and these mode conversion resonances overlap to create stronger mode conversion ( $\approx -15dB$  or 97%).

In order to further study the properties of microbend gratings, we focus further on the  $HE_{21}^{even,odd}$  resonances using a 1550nm LED source (bandwidth of  $\approx 40nm$ , enabling a higher degree of polarization). In addition, a polarization controller was installed onto the SMF (Fig. 4·2 A). We observed that microbend gratings are highly polarization sensitive devices (Fig. 4·2 B), with conversion oscillating from weak  $-9dB$  ( $= 87.4\%$ ) under-coupling, to strong  $-25dB$  ( $= 99.7\%$ ) conversion. The reason behind this lies in the fact that any stress on fiber inherently introduces asymme-

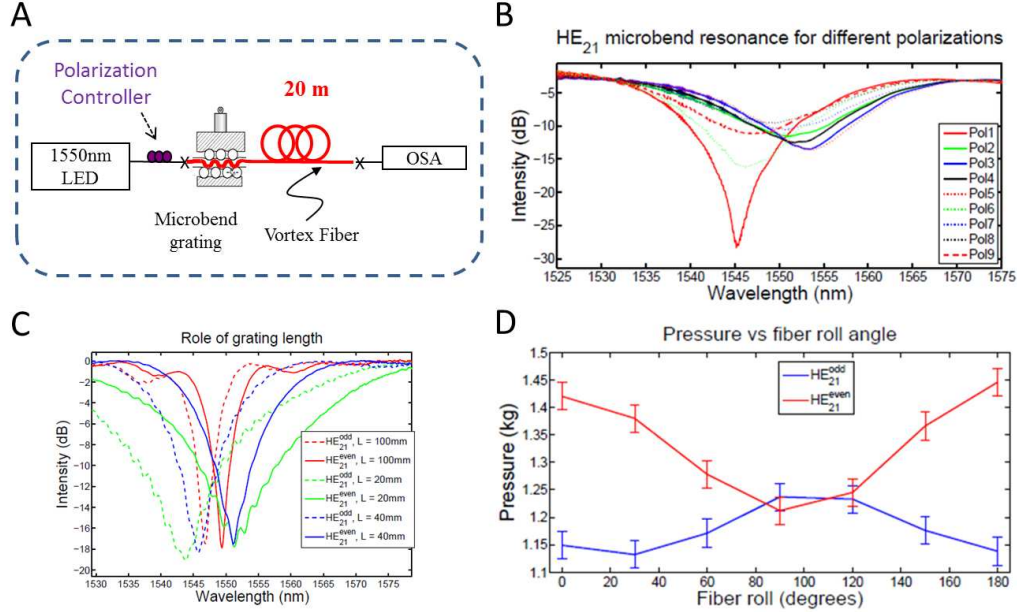


**Figure 4.2:** Microbend resonance characteristic with respect to input polarization, grating length and fiber roll angle. **(A)** Polarization dependence. **(B)**  $HE_{21}$  resonances for different grating lengths. Longer grating length require less pressure per fiber length, hence, pressure induced splitting is smaller. Note grating bandwidth change with length, in agreement with the theory. **(C)** Microbend pressure for  $HE_{21}^{odd}$  and  $HE_{21}^{even}$  resonances vs fiber roll angle (i.e. rotation axis is along the fiber).

try in the otherwise circularly symmetric fiber. This asymmetry (that manifests in non-zero ellipticity) introduces birefringence for the two polarization modes, resulting in a shifted resonance. In addition to induced birefringence (observed through resonance shift), we note a change in the grating strength ( $\kappa_g$  in Eq. 4.3) for different polarizations, leading to conclusion that  $\kappa_g L_g \neq \pi/2$  for all the polarizations. We further observe the role of the grating length (Fig. 4.2 C). As the length of the gratings changes, the grating pressure per length changes in a sense that shorter gratings ( $L_g = 20$  mm), exhibit more pressure per length than 100mm long grating. Therefore, shorter grating induce more birefringence and larger separation among the two

$HE_{21}^{even,odd}$  mode resonances.

At the end of the microbend grating study, we study the effect of the fiber roll angle (rotation around the fiber axes). We note that for certain fiber orientation (in this case at  $100^\circ$  angle) the same pressure can be used for both  $HE_{21}^{even,odd}$  resonance so  $\kappa_g^x = \kappa_g^y$ , however the induced birefringence (i.e. resonance splitting) is still unavoidable. Nevertheless, this points to the important fact that vortex fiber is essentially not perfectly cylindrically symmetric but instead exhibits some degree of ovality. Measuring the degree of ovality is left for future work.

#### 4.1.3 $CO_2$ laser induced gratings

$CO_2$  laser-induced gratings are compact device that offer reduced sensitivity to the environment and convenience for deployment (Poole and Presby, 1995). It has been shown that  $CO_2$  laser gratings change both the geometry of a fiber as well as the refractive index of the core and cladding in such a way as to achieve anti-symmetric perturbation (Abrishamian et al., 2012).  $CO_2$  lasers operate at a  $10.2\mu m$  wavelength and typically have high powers (in our case  $\approx 10W$ ), which can easily create permanent glass deformations. In order to test the feasibility of  $CO_2$  gratings for future device deployment, a setup capable of point-by-point LPG writing was built (Fig. 4·3 A). The laser beam was first expanded to the size of  $D \approx 20mm$ , and then focused onto the vortex fiber using  $f = 60mm$  lens, producing spot size of  $\Phi_{spot} = \frac{4\lambda f}{\pi D} \approx 40\mu m$ . Using a powermeter that was placed behind the fiber, one was able to measure whether the beam would hit the fiber, in which case most of the power would be absorbed by the glass and a small portion of the beam would be transmitted. After several setup iterations, a relatively repeatable procedure was developed for grating manufacturing (see next section for detailed step-by step instructions). The microscope image of the fiber, after the grating has been inscribed, clearly indicates periodic changes (Fig. 4·3 C). Unlike in the microbend case, the  $CO_2$  grating exhibited smaller polarization

sensitivity (Fig. 4.3 D), however, the current technique allowed for  $> 10\text{dB} (= 90\%)$  mode conversion. The ripples in the resonances are typical for multi-path interference (MPI) and are an indicator of incomplete mode conversion. We discuss this effect in more details in Sec. 4.1.4.

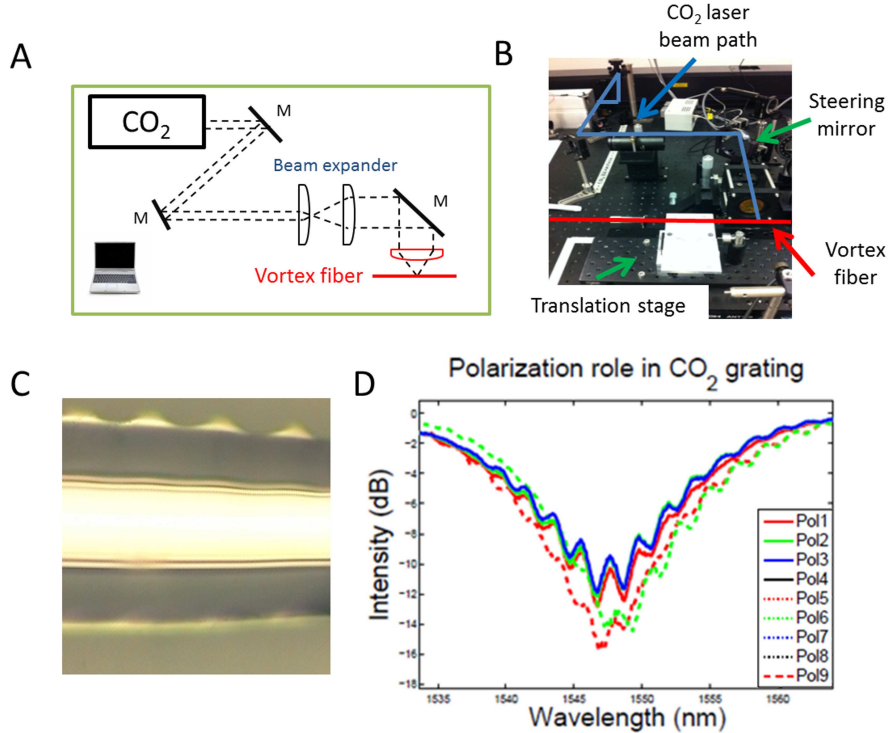


**Figure 4.3:**  $\text{CO}_2$  laser induced gratings. **(A)** Setup. Laser beam is focused onto the fiber and point-to-point grating is written onto the vortex fiber. **(B)** Setup photo (blue line indicates beam path, red line indicates vortex fiber). **(C)** Microscope image of the grating inscribed in the fiber, indicating periodic mechanical changes. **(D)** Polarization dependence of the  $\text{CO}_2$  gratings. In comparison to microbend gratings (Fig. 4.2),  $\text{CO}_2$  gratings are less polarization sensitive.

### $\text{CO}_2$ laser grating writing procedure

Described below is the detailed procedure for point-by-point  $\text{CO}_2$  laser grating writing for a setup in the NFNO lab (concluding by January 5<sup>th</sup> 2012). The goal of this procedure is to describe the current technique (admittedly there is a room for im-

provement). Before describing the procedure, we note few causes for common fiber breaks and grating failures: 1) bad fiber clamping can cause fiber to snap or allow tension to change during writing process, 2) fiber from which the coating is stripped down can be scratched when in contact with the hard surface (beakers, optical table, etc.), causing the fiber to break, 3) placing heavy objects (fiber spool for example) on a fiber at any time should be avoided, 4) sudden yanks of the fiber during handling can likely break the fiber, so slow fiber movements are suggested. The procedure for grating writing goes as follows.

- Turn on a water pump and check if the water flow is 2 - 2.5 GPM. Set the acid heater to 300°C. Turn on the  $CO_2$  laser controlled by a function generator (Agilent E4420B), with the the following LF out settings: LF Out Amplitude: 5.0 Vp, LF Out Source: Func Generator, LF Out Waveform: Pulse, LF Out Period: 200.0 sec (do not change this value), LF out Width: 8.0-200.0 s (this number can be used to adjusted  $CO_2$  power, and is calibrated in the control software below; 20-30 s might already be very powerful for writing!). Turn on HeNe laser (provide 5V from DC power supplier HP E3632A), OSA, electronic polcon and computer. Software used for writing is located here:

```
\eng_research_fibers\_programs\CO2 grating Labview software Nenad
```

- Measure the beam spot size of a laser one time only using a translating blade procedure. The spot size should be almost diffraction limited, i.e.  $1.22\lambda/NA$  for  $1/e^2$ -diameter waist.
- Strip off small amount ( $\approx 50mm$ ) amount of coating in the Sulfuric acid (93%  $H_2SO_4$ and 7%  $N_2H_3$ ; common proportion is 200ml:15ml). Be careful not to touch beakers or any other hard surfaces as they can create a microscopic crack in the fiber glass. Dip the fiber into IPA and then methanol to wash off the excess acid. Use pen marker to mark the stripped fiber area. Clamp the fiber into a translation stage. Be aware of the stage limit points.

- Set the tension of the fiber to approx. 200 grams. Use LF on/off on the function generator to turn  $CO_2$  laser on/off. Focus the laser onto fiber with low power ( $\approx 0.1W$ ), and place the power meter behind the fiber. Minimize the power by moving the lens in the longitudinal (z) direction, so the fiber absorbs most of the laser power, indicating that the fiber is close to the beam waist. Keep the aperture before the focusing lens closed as lower NA is easier to work with. Only the aperture after the beam expander should be used, the one after the mirror should stay open. Minimize the power by moving the mirror in the vertical direction only. Write down the name of the grating starting by date, increase power ( $\approx 5.5W$ ). Make sure you have enough space for translation ( $\approx 50mm$ ). Acquire reference with the OSA. Enter the grating period in the software. Start writing the grating.
- As the resonance is growing, tune the polcon to maximize it. At some point the deepest resonance will stop growing and start over-coupling. Observe the second resonance that sits on the other side of the Poincare sphere. These two polarizations have different coupling strengths (a.k.a.  $\kappa_g$ ). As  $\kappa_{g1}L$  is dropping the  $\kappa_{g2}L$  will be increasing. The goal is to stop writing when  $\kappa_{g1}L = \kappa_{g2}L$ . It is possible to follow resonances one grating line at a time in real time. Stop writing the grating. Skillfully remove the fiber and put it in the foam holders. Acquire spectra.
- Shut down the lasers (function generator for  $CO_2$  and DC power supplier for He-Ne, turn off the interlock, power supplier, and He-Ne button in the black homemade controller box, unplug laser power cable). After 10 minutes turn off the water pump chiller (check distilled water status). Turn off the acid heater.
- Depending on the phase matching conditions of the fiber,  $CO_2$  gratings have

showed that the grating resonance can be shifted by approximately a few nanometers if heated. This shift is not permanent.

#### 4.1.4 Role of tapers in improving mode conversion

In a general sense, a fiber taper is a in-fiber device on the order of tens of millimeters in size, created in a multimode or few-mode fiber, that in our case enables small fiber segment to become single-moded (Birks and Li, 1992). In this section we discuss how this fact can improve the OAM mode quality and we experimentally verify improved mode conversion.

So far, all the resonance measurements (Fig. 4·2 B, 4·3 D) required a splice between i) a SMF and ii) a vortex fiber that supports few modes (Fig. 4·2 A). However, in the case of an imperfect splice (offset and angle splice), the fundamental mode originating from the SMF can have a non-zero overlap integral with the vortex fiber HOM, therefore making the splice itself act as a mode converter. This property, however, negates the mode conversion created by the subsequent fiber grating since gratings are reciprocal devices. If all of the  $HE_{11}$  mode converts to  $HE_{21}$ , by reciprocity, an imperfect splice will create several modes to co-exist in fiber. Since these modes have different propagation constants, mode beating (or MPI) will occur, which can be observed as ripples in a resonance (Fig. 4·3 D).

A relatively easy solution for this problem lies in tapers, that can be used to make near-perfect devices that do not allow mode coupling. Essentially, taper on a multimode fiber acts as a mode stripper, coupling all the unwanted HOM modes (that could have been created in the imperfect splice) into radiation modes that disappear from the fiber after short propagation length. An important observation is that the taper needs to exist in a medium that has a refractive index larger or equal to that of the cladding refractive index (for this purpose index-matching gel or oil is used). If this step is omitted, rather than to radiative modes, fundamental mode will convert

into cladding modes that can still have a detrimental effect on mode purity.

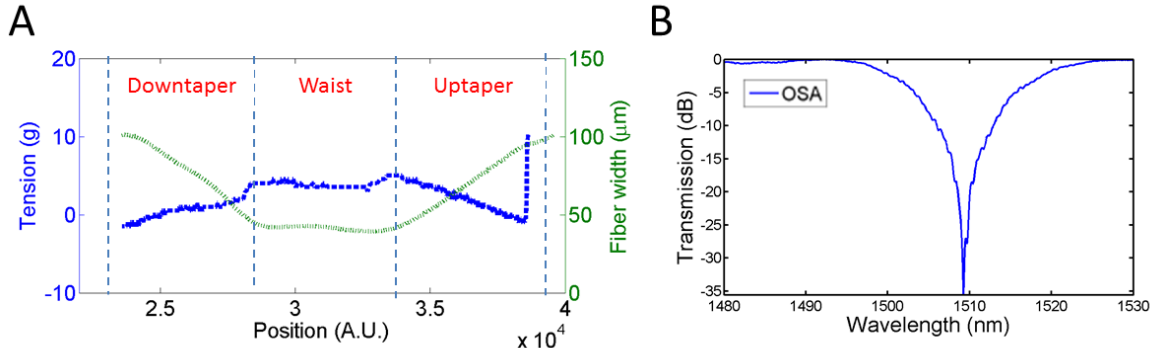


**Figure 4·4:** (A) Tension and fiber width profile for a 5-5-5 $\mu\text{m}$  taper geometry with 40 $\mu\text{m}$  waist. (B) Resonance for dk11OD100 fiber in the case of a taper shown in A.

Tapers in vortex fibers were formed by stretching the fiber in a heat source using a tapering station (Ring of Fire, 3SAE Technologies). The shape of the taper for this case has been previously studied (Birks and Li, 1992). We used 5-5-5mm geometry (where 5mm refers to the length of each of the three taper regions: downtaper region, waist and uptaper region) and a 40 $\mu\text{m}$  waist size (Fig. 4·4 A). The three tuning parameters were arc powers for the 1) downtaper region, 2) waist and 3) uptaper region. The basic principle was to develop a procedure that will keep a very low tension, though always larger than zero so the fiber is kept straight, with the starting point at about 10 grams. The tension typically drops when the tapering process starts and goes up at the end of the process (typical tension profile is plotted in Fig. 4·4 A). The heat arcs should be adjusted so the tension stays as low as possible, optimally less than 10g (tensions of >30g did not perform well). Using the developed tapering procedure, mode conversion of  $35\text{dB} = 99.97\%$  can be achieved (Fig. 4·4) with fairly good repeatability of several devices in a row. The power numbers did however vary for different fiber ODs, and at this level, only an empirical procedure

has been developed. The taper procedure is unidirectional in nature, meaning the heat arc will sweep the fiber only in one direction as the fiber is being pulled.

#### 4.1.5 Group index difference calculation

In this short segment we describe two methods to calculate group index difference between the  $HE_{11}$  mode and a desired mode (Ramachandran, 2005). The first method is based on a resonance parameter fitting. As we previously mentioned, the resonance can be described as a *sinc* function Eq. 4.1, where we again rewrite equation for detuning parameter  $\delta$ :

$$\delta(\lambda) = \frac{1}{2}(\beta_1(\lambda) - \beta_2(\lambda)) - \frac{\pi}{\Lambda}. \quad (4.5)$$

If we now Taylor expand this equation around the resonant wavelength  $\lambda_{res}$ , and use the fact that detuning parameter becomes zero for  $\lambda_{res}$  (i.e.  $\Delta n_{eff} = \lambda_{res}/\Lambda$ ) we can write:

$$\delta(\Delta\lambda) = -\frac{\pi\Delta\lambda\Delta n_g(\lambda_{res})}{\lambda_{res}^2} = D_0\Delta\lambda, \quad (4.6)$$

where  $\Delta n_g$  is a group index difference (that we are looking to determine), and we define  $D_0 \stackrel{def}{=} -\frac{\pi\Delta n_g(\lambda_{res})}{\lambda_{res}^2}$ , which represents the slope of  $\delta(\lambda)$  curve.

In practice, in order to calculate the group index difference ( $\Delta n_g$ ), the resonance is fitted using Eq. 4.1 (see Fig. 4.5) which would then provide the slope of the detuning parameter function  $D_0 = \delta'(\lambda)$ . Knowing this, simple operations lead to estimating  $\Delta n_{g, HE_{11}-HE_{21}} @ 1550nm = -\frac{\lambda_{res}^2 D_0}{\pi} = -(2.7 \pm 0.1) \times 10^{-3}$ , in the case of dk110127OD100 fiber.

The second method to measure the group index difference is by observing several resonant wavelengths for different microbend gratings (Fig. 4.6). Grating period  $\Lambda$ , resonant wavelength and effective index difference  $\Delta n_{eff}$  are related by  $\Delta n_{eff}(\lambda) =$

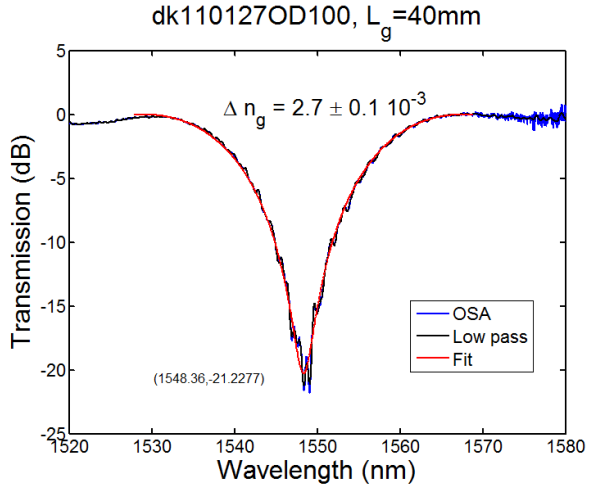


**Figure 4.5:** Loss transmission spectrum for  $HE_{11}$  and  $HE_{21}$  phase matched case. Fitting the curve with the expected  $\text{sinc}^2$  profile gives the group index difference  $\Delta n_g$ .

$\lambda/\Lambda(\lambda)$ . Taking the derivative of this equation with respect to wavelength, one finds:

$$\Delta n_g(\lambda) = \Delta n_{eff}^2(\lambda) \frac{d\Lambda}{d\lambda} = \left( \frac{\lambda}{\Lambda(\lambda)} \right)^2 \frac{d\Lambda}{d\lambda}. \quad (4.7)$$

Using this method for the example of the dk110127OD100 fiber, we experimentally obtained a  $\Delta n_g$  value between the  $HE_{11}$  and  $HE_{21}$  modes at 1550nm to be  $\Delta n_g = -2.8 \times 10^{-3}$ , which is in agreement with the value obtained previously. Plots of  $\Delta n_{eff}$  and  $\Delta n_g$  at different wavelengths are shown in Fig. 4.6.

## 4.2 Spatial light modulator approach

The LCoS SLM is a device that can very precisely control a phase front of beam (He et al., 1995). Application of SLMs include optical beam pattern forming (Matsumoto et al., 2008) and aberration correction (Friberg and Dandliker, 2008) (Fig. 4.7). In our case, an SLM is used to create a free-space OAM mode which is then coupled into a cleaved vortex fiber. This method, unlike fiber gratings, allows for multiplexing

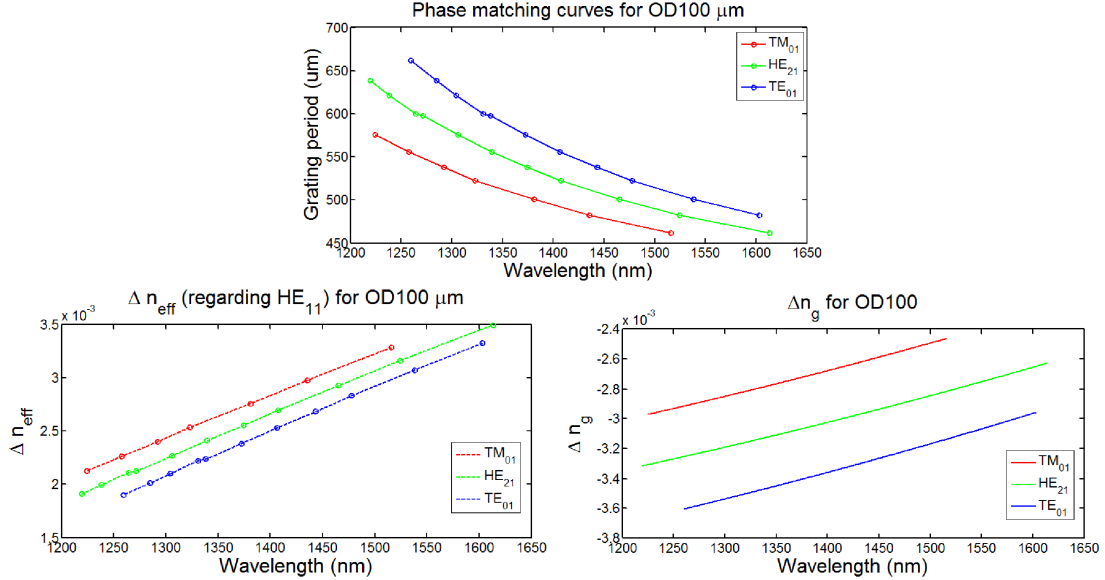


**Figure 4.6:** Phase matching curves  $\Lambda(\lambda)$  relate grating period  $\Lambda$  with resonant wavelength (particular example is for the case of dk110127OD100 fiber). Respective  $\Delta n_{eff}$  and  $\Delta n_g$  can be calculated (bottom two graphs).

several beams at the same time.

A setup built for OAM mode generation in a fiber is shown in Fig. 4.8. SMF output is collimated and reflected off the LCoS SLM (Hamamatsu, X10468-8). Here, we use an on-axis conversion using a beam-splitter (in later chapters an off-axis conversion is used to avoid 3dB loss from the beam-splitter). Care must be taken to make the SLM, and all the other optical components, stable. Also, the SLM can modulate only one polarization that is aligned with the orientation of the liquid crystals. Two mirrors and pinholes were used to align the beam onto the SLM with the spiral pattern applied. After reflection from the SLM, a donut beam carrying orbital angular momentum is observed on the camera and the spiral pattern is adjusted in order to obtain a donut shaped mode with the least variations (Fig. 4.9).

In order to couple the beam into the fiber, a telescope made of two  $f = 200\text{mm}$  lenses relayed the beam onto the objective (for larger beams this step is not necessary

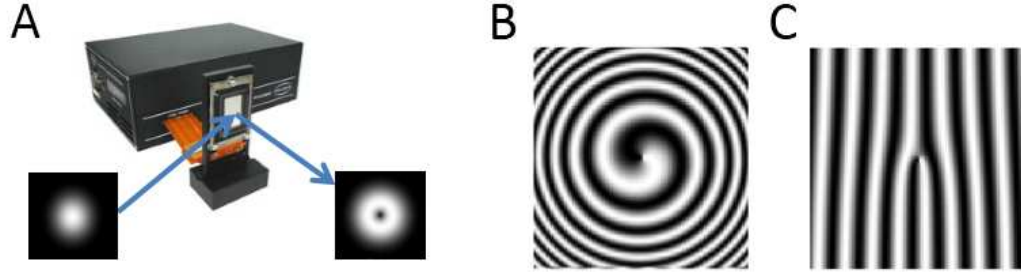


**Figure 4·7:** (A) SLM mode conversion concept. After reflection off a SLM, an OAM beam is created. (B) The spiral SLM pattern that creates the  $LG_{10}$  beam at the same reflection angle as the  $LG_{00}$  beam incident angle. (C) The fork SLM pattern that creates the  $LG_{10}$  beam at the different reflection angle from the  $LG_{00}$  beam incident angle.

as the depth of focus is large). Instead of a fiber, a mirror was first installed onto the 6D stage (Thorlabs, Nanomax 601D) and the back-reflection was imaged on a camera (VDS, NIR-300) at camera position 1 (CamPos1 in Fig. 4·8 A). We noticed that good alignment is critical to avoid spherical aberration. It is especially critical to center the beam on the objective. Testing showed that a Mitutoyo 20x objective (NA=0.4) performed well (see Fig 4·10), and significant aberrations were noticed for low-quality objectives. After ensuring good alignment of the beam with respect to the objective, fiber was installed into the 6D stage. Back reflected light from the fiber end-face can be observed at the camera position 1 (Fig. 4·11).

Finally, we observe the output of the vortex fiber after OAM mode coupling (Fig. 4·12). Precision on the order of 50nm is critical to obtain a qualitatively good OAM mode. In the next chapter, we study several methods that determine the modal purity of the generated OAM states.

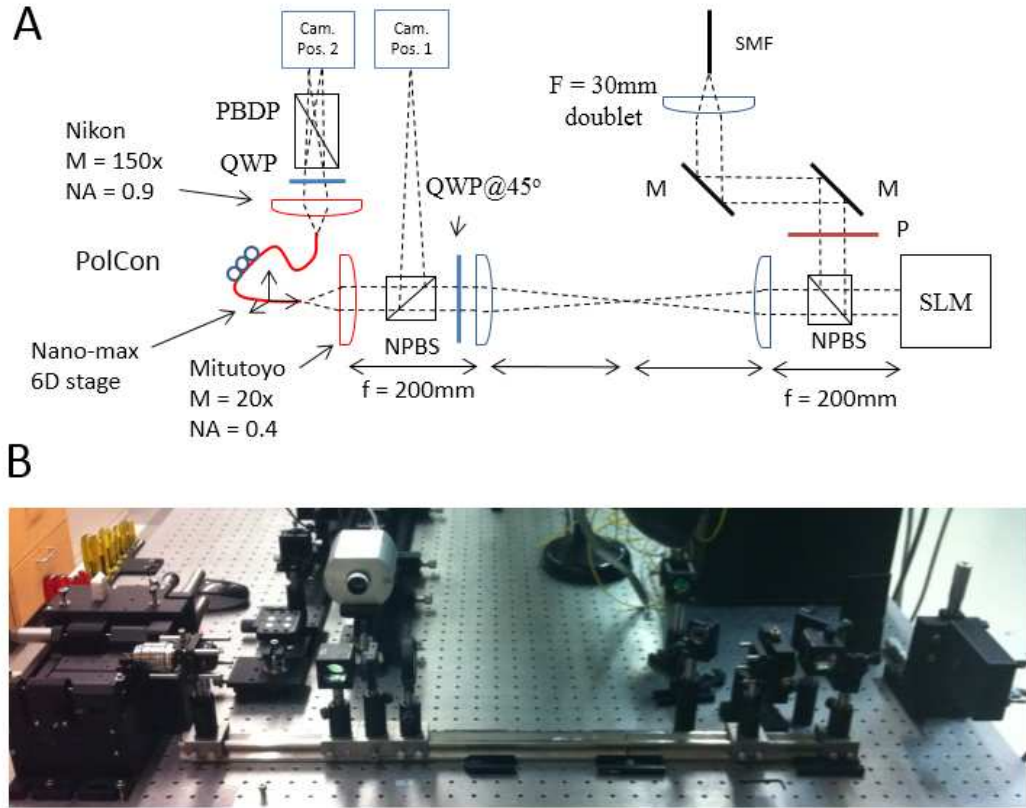


**Figure 4.8:** Spatial light modulator based mode conversion. (A) Setup. (B) Photo of the setup.

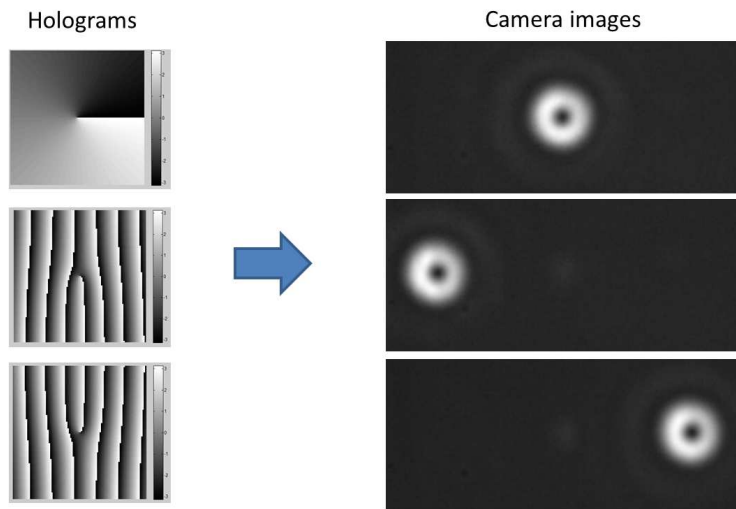


**Figure 4.9:** Spiral and fork holograms that create  $LG_{10}^*$ , showing the effect of tilt in the case of the fork hologram.

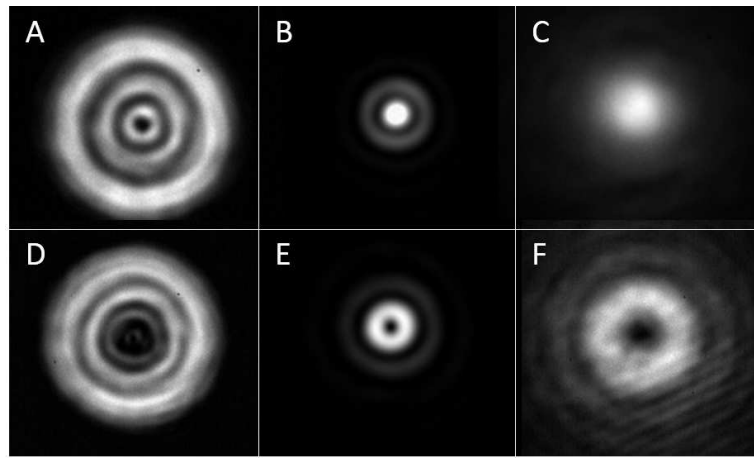


**Figure 4-10:** Back-reflection from the mirror installed instead of the fiber for three different axial positions of the coupling stage for a beam free of aberrations: (A,C) defocused  $LG_{00}$  (B) focused  $LG_{00}$  (D,F) defocused  $LG_{10}$  (OAM mode)(E) focused  $LG_{10}$ . Symmetric pattern, indicates good alignment between input beam and the fiber.

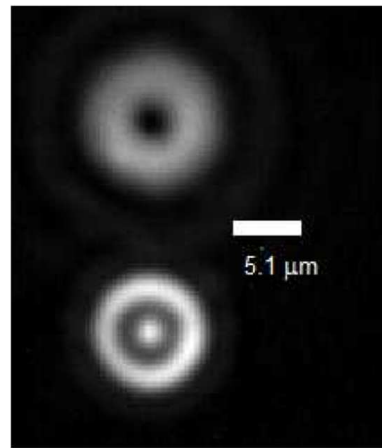


**Figure 4-11:** Camera image at the CamPos1 for the vortex fiber installed. Donut mode represents back reflection from the fiber end-face (similar to the case of the mirror in the Fig. 4-10).  $HE_{11}$  mode represents light coming out of the vortex fiber, when the other fiber end is connected to the light source. Two images here are intentionally misaligned.

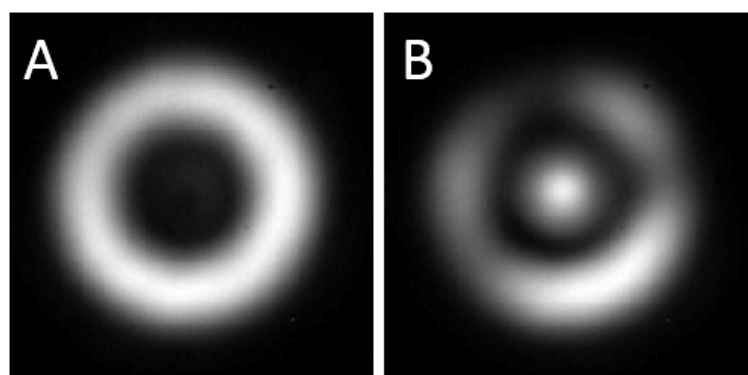


**Figure 4-12:** Output of the vortex fiber after OAM mode coupling.  
**(A)** Aligned and **(B)** misaligned case.

## Chapter 5

# OAM Purity Measurements

In previous chapter, we studied two methods for OAM mode generation in fibers and showed results that qualitatively confirm the existence of OAM states. In this chapter we quantitatively study OAM mode purity using two methods:

- Ring method (Bozinovic et al., 2012a), and
- Regression analysis (Golowich et al., 2013)

These techniques allow us to obtain measure of OAM mode power for different fiber lengths allowing us to track their evolution in vortex fibers.

### 5.1 Ring technique

In Sec. 4.1.2 we demonstrated how microbend gratings create OAM state, and observed the helical phase of these modes using interference with the expanded Gaussian reference beam. The ring technique that we introduce here is a method to quantify OAM mode purity using image analysis. In particular, the ring technique requires acquisition of the two circular polarization projections, acquired simultaneously.

An imaging setup built for this purpose is shown on Fig. 5·1, and it can be considered an extension of Fig. 4·1. A 3dB coupler is used to combine two sources: 1) a 50nm-wide 1550nm LED, and 2) a 100kHz narrowband CW tunable external cavity laser (ECL) (Agilent 8168F). One arm of the 3dB coupler is spliced to a vortex fiber using standard splicing equipment (Ericsson FSU 995). A microbend grating

(40mm length,  $475\mu\text{m}$  period), with only the LED source turned on, converts the fundamental mode of a SMF into the desired  $HE_{21}^{odd}$  mode with  $18dB$  conversion efficiency (Fig. 5·1 B). After the desired mode coupling is obtained for a desired wavelength (in this case, 1527 nm), the source is switched from LED to the ECL laser. The vortex fiber is then cleaved after the output of the microbend and placed at the fiber stage for imaging.

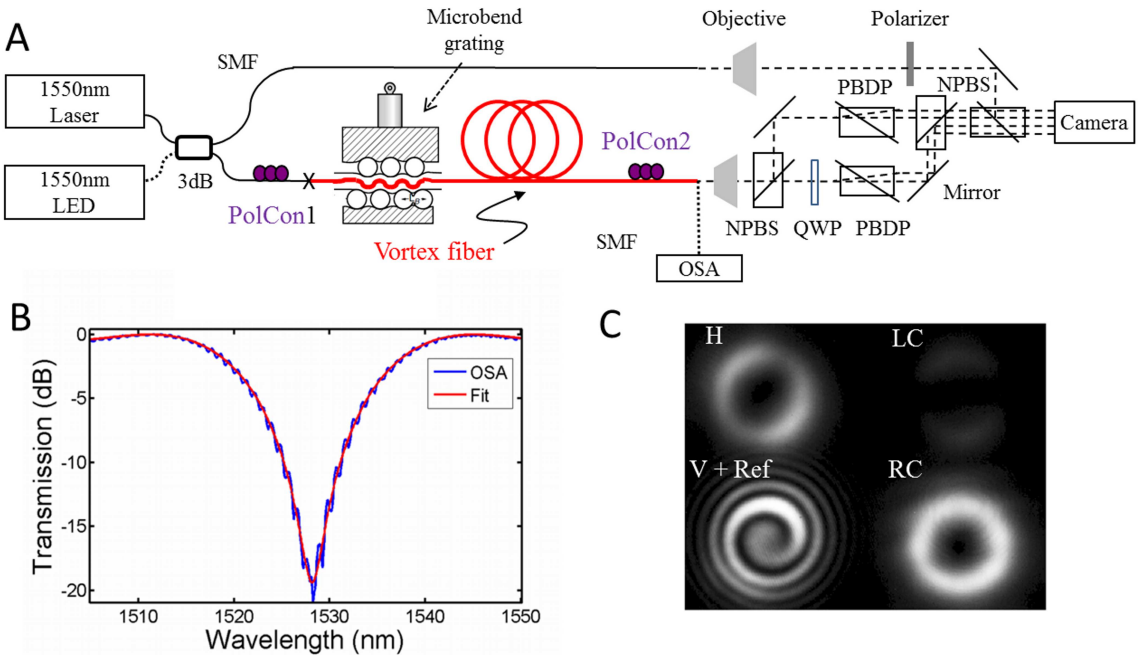


**Figure 5·1:** Setup for imaging vortex fiber output. **(A)** Experimental setup that uses grating for OAM mode generation. **(B)** Grating resonance spectrum used to deduce  $HE_{21}^o$  mode conversion level. **(C)** Camera image of the four polarization projections of the fiber output. Acronyms: left circular (LC), right circular (RC), vertical (V) and horizontal (H), non-polarizing beam splitter (NPBS), quarter wave plate (QWP), polarizing beam displacing prism (PBDP). Vertical (V) polarization projection was interfered with the reference beam (Ref.) in order to observe the phase of the vortex beam. Showed is the  $l = +1$  OAM state that is circularly polarized (spin = 1).

In order to obtain two desired polarization projections (LC and RC) as well as

ability to image a phase of a beam simultaneously, a combination of non-polarizing beam splitters (NPBS), quarter wave plates (QWP) and polarizing beam displacing prisms (PBDP), is used. In particular, left circular (LC), right circular (RC), vertical (V) and horizontal (H) projections were obtained. An example of an image acquired at the camera (VDS, NIR-300, InGaAs, FOV: 10mm X 8mm) is shown in Fig. 5·1 (C), where the vertical (V) polarization projection was interfered with the reference beam (Ref.) in order to observe the phase of the beam.

In a free-space, a linear combination of the  $l = \pm 1$  OAM modes has been shown to have a total OAM of topological charge that lies between  $-1 \leq l \leq 1$  (Schmitz et al., 2006). Similarly, one can ask how to achieve this linear combination in the case of a fiber. The answer is very simple and draws analogy from the two polarization states in the SMF, namely, a linear combination of the two OAM  $l = \pm 1$  fiber modes with arbitrary relative amplitudes can be obtained using commercial polarization controller mounted on the vortex fiber (PolCon2 on Fig. 5·1). Verification of this can be seen on Figure 5·2, where positions of the polcon2 paddles have been tuned to achieve different OAM states, in particular, the state was tuned from  $l = 1$  (Fig. 5·2 A) to  $l = -1$  (Fig. 5·2 C). The reason for this lies in the fact that bend-induced-stress of a polarization controller can couple one OAM state into other, since two OAM states are degenerate (similar effect is observed with two polarizations of a fundamental mode,  $HE_{11}^{x,y}$ ).

In the general case of the vortex fiber under study (dk110127OD100), light at the vortex fiber output can contain contributions from the six vector modes:  $\mathbf{HE}_{11}^{x,y}$ ,  $\mathbf{HE}_{21}^{even,odd}$ ,  $\mathbf{TM}_{01}$  and  $\mathbf{TE}_{01}$  (Snyder and Love, 1983). To analyze the purity of the

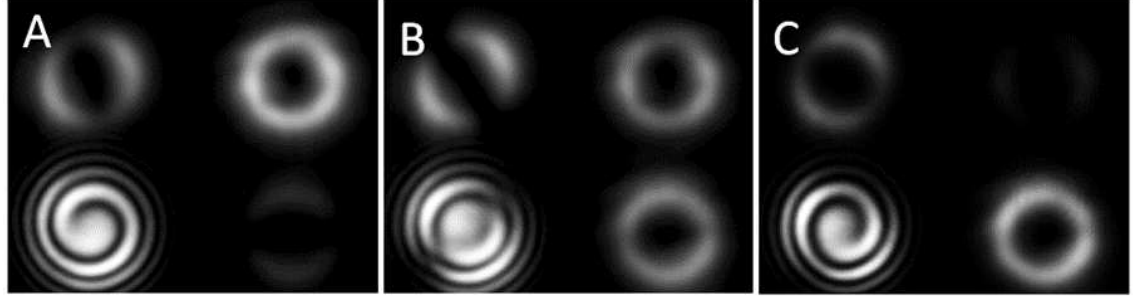


**Figure 5·2:** Camera images for the three positions of the polcon2 paddles, tuned to achieve (A)  $l = 1$ , (B)  $l = 0$  and (C)  $l = -1$  state.

OAM states it is more convenient to introduce a so-called vortex basis set:

$$\begin{aligned}
 \mathbf{V}_{11}^+(r, \theta) &\stackrel{\text{def}}{=} (\mathbf{HE}_{11}^x + i\mathbf{HE}_{11}^y) / \sqrt{2} = (\hat{\mathbf{x}} + i\hat{\mathbf{y}})F_{01}/\sqrt{2} \\
 \mathbf{V}_{11}^-(r, \theta) &\stackrel{\text{def}}{=} (\mathbf{HE}_{11}^x - i\mathbf{HE}_{11}^y) / \sqrt{2} = (\hat{\mathbf{x}} - i\hat{\mathbf{y}})F_{01}/\sqrt{2} \\
 \mathbf{V}_{21}^+(r, \theta) &\stackrel{\text{def}}{=} (\mathbf{HE}_{21}^e + i\mathbf{HE}_{21}^o) / \sqrt{2} = e^{i\theta}(\hat{\mathbf{x}} + i\hat{\mathbf{y}})F_{11}/\sqrt{2} \\
 \mathbf{V}_{21}^-(r, \theta) &\stackrel{\text{def}}{=} (\mathbf{HE}_{21}^e - i\mathbf{HE}_{21}^o) / \sqrt{2} = e^{-i\theta}(\hat{\mathbf{x}} - i\hat{\mathbf{y}})F_{11}/\sqrt{2} \\
 \mathbf{V}_T^+(r, \theta) &\stackrel{\text{def}}{=} (\mathbf{TM}_{01} - i\mathbf{TE}_{01}) / \sqrt{2} = e^{-i\theta}(\hat{\mathbf{x}} + i\hat{\mathbf{y}})F_{11}/\sqrt{2} \\
 \mathbf{V}_T^-(r, \theta) &\stackrel{\text{def}}{=} (\mathbf{TM}_{01} + i\mathbf{TE}_{01}) / \sqrt{2} = e^{i\theta}(\hat{\mathbf{x}} - i\hat{\mathbf{y}})F_{11}/\sqrt{2}
 \end{aligned}$$

where we have used the fact that, for this fiber, the vector modes may be accurately expressed as linear combinations of LP modes through the weak guidance approximation, and  $F_{lm}(r)$  denote the radial wave functions of the LP<sub>lm</sub> modes (Snyder and Love, 1983). Note that in this representation, the  $\mathbf{V}_{21}^{+,-}$  modes correspond to the desired OAM states in the fiber. The total electric field can be expressed as:

$$\mathbf{E}(r, \theta) = \sum_{l=[11,21,T]} \sum_{s=[+,-]} \gamma_l^s \mathbf{V}_l^s(r, \theta), \quad (5.1)$$

where  $\gamma_l^s$  are the mode field complex amplitudes of the normalized vortex basis vectors.

We denote mode power contributions as:

$$MPI_l^s \stackrel{def}{=} 10\log_{10}(|\gamma_l^s|^2/P_{\text{tot}}), \quad (5.2)$$

where  $P_{\text{tot}} = \sum_l \sum_s |\gamma_l^s|^2$ . To experimentally measure the mode amplitudes, we consider the intensity of the LC polarization projection:

$$|P_+ \mathbf{E}(r, \theta)|^2 = |\gamma_{11}^+ F_{01}(r) + \gamma_{21}^+ e^{i\theta} F_{11}(r) + \gamma_T^+ e^{-i\theta} F_{11}(r)|^2.$$

The key approximation in our analysis is that the  $|\gamma_{11}^+||\gamma_T^+|$  term may be neglected, which is valid when most of the power is confined to the HE<sub>21</sub> modes, as is the case in the experiments presented below. In addition, for simplicity we confine attention to the points on the radius  $r_0$ , for which  $F_{01}(r_0) \approx F_{11}(r_0)$  (we observe that  $r_0$  conveniently corresponds to the radius of the LC and RC projection ring). The LC azimuthal intensity at  $r_0$  now simplifies to:

$$\begin{aligned} |P_+ \mathbf{E}(r_0, \theta)|^2 \sim DC &+ \Delta_1 \cos(\theta + \phi_{21,11}) + \\ &+ \Delta_2 \cos(2\theta + \phi_{21,T}), \end{aligned} \quad (5.3)$$

where  $\phi_{ij}$  indicates the phase difference between the two corresponding modes and we define:

$$DC \stackrel{def}{=} |\gamma_{11}^+|^2 + |\gamma_{21}^+|^2 + |\gamma_T^+|^2, \quad (5.4)$$

$$\Delta_1 \stackrel{def}{=} 2|\gamma_{11}^+||\gamma_{21}^+|, \quad (5.5)$$

$$\Delta_2 \stackrel{def}{=} 2|\gamma_{21}^+||\gamma_T^+|. \quad (5.6)$$

By taking the Fourier series of  $|P_+ \mathbf{E}(r_0, \theta)|^2$ , the coefficients  $DC$ ,  $\Delta_1$  and  $\Delta_2$  can be determined; the mode powers ( $|\gamma_l^s|^2$ ) can then be obtained by solving Eq.s 5.4-5.6. Figure 5.3 A shows an example of a measurement of  $|P_+ \mathbf{E}(r_0, \theta)|^2$  – the azimuthal

intensity variation of the image that occurs due to interference between the  $\mathbf{V}_{21}^+$ ,  $\mathbf{V}_{11}^+$  and  $\mathbf{V}_T^+$  modes. Figure 5·3 (B) shows the example of the Fourier series analysis, and 5·3 (C) illustrates the powers of the extracted modes. An equivalent procedure was also repeated for the RC projection to calculate amplitudes of the negative helicity modes.

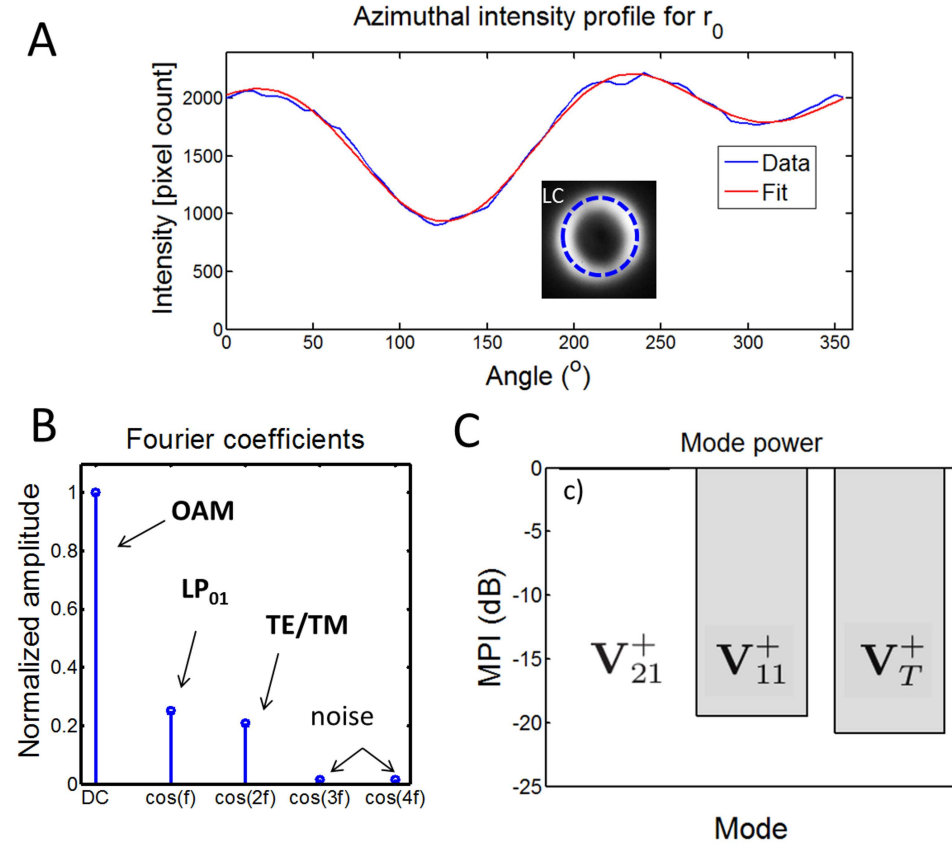


**Figure 5·3:** Ring method analysis for determining modal content of the vortex fiber. **(A)** Azimuthal intensity profile of LC projection for radius  $r_0$ . **(B)** Fourier series coefficients for profile in (A). **(C)** Extracted modal power contributions.

The high purity of the vortex states implies that only two modes – the  $\text{HE}_{21}^{even,odd}$  pair – are dominantly present in the fiber. Here, we would like to emphasize the analogy of the two  $\text{HE}_{21}$  modes with the two linearly-polarized fundamental modes –

$\text{HE}_{11}^{x,y}$ . As with the two fundamental modes, we first note that since the  $\text{HE}_{21}$  modes are degenerate, they can easily couple to each other under controlled perturbations. Second, just as a linear combination of two fundamental modes with  $\pm\pi/2$  phase shift will create a circularly polarized state, the same linear combination of the two  $\text{HE}_{21}$  modes results in an OAM state. This analogy has also been elegantly represented by a higher order Poincaré sphere by other authors studying OAM (Padgett and Courtial, 1999; Milione et al., 2011). A general linear combination of the two  $l = \pm 1$  OAM modes will have a topological charge with non-integer OAM (Schmitz et al., 2006).

In order to show the ability of the system to control OAM, camera images were observed and analyzed while the polarization controller (PolCon2 on Fig 1a) was manually tuned using adjustable paddles. Figure 5·4 (A) shows the modal power distribution as the system was tuned through the different linear combinations of the vortex states. In particular, Fig. 5·4 (B) shows observed camera images for the pure  $\mathbf{V}_{21}^+$  state (A), linear combination of the vortex states (B) and the pure  $\mathbf{V}_{21}^-$  state (C). Note that using a quarter wave plate,  $\mathbf{V}_{21}^{+,-}$  states can be converted to the conventionally constructed linearly polarized OAM states. Our calculation showed that the combined power of the undesired  $\mathbf{V}_T^{+,-}$  and  $\mathbf{V}_{11}^{+,-}$  modes mostly stayed below a level of -15 dB (3%).

To estimate the error of the method described, a simulated data set has been created with known contributions of each of the vortex basis vectors. Empirically estimated dark noise was first added, followed by adding shot noise (st.dev=  $\sqrt{N}$  where N is pixel count), finally subtracting the dark noise from the obtained image. The data set was then analyzed and the original and the recovered mode powers were compared. Estimated errors were <0.01 dB,  $\approx 0.2$  dB and  $\approx 0.2$  dB for the  $\mathbf{V}_{21}^{+,-}$ ,  $\mathbf{V}_T^{+,-}$  and  $\mathbf{V}_{11}^{+,-}$  modes respectively. With this demonstration we conclude that our system can create any linear combination of OAM states ( $-1 \leq l \leq +1$ ), in a controllable

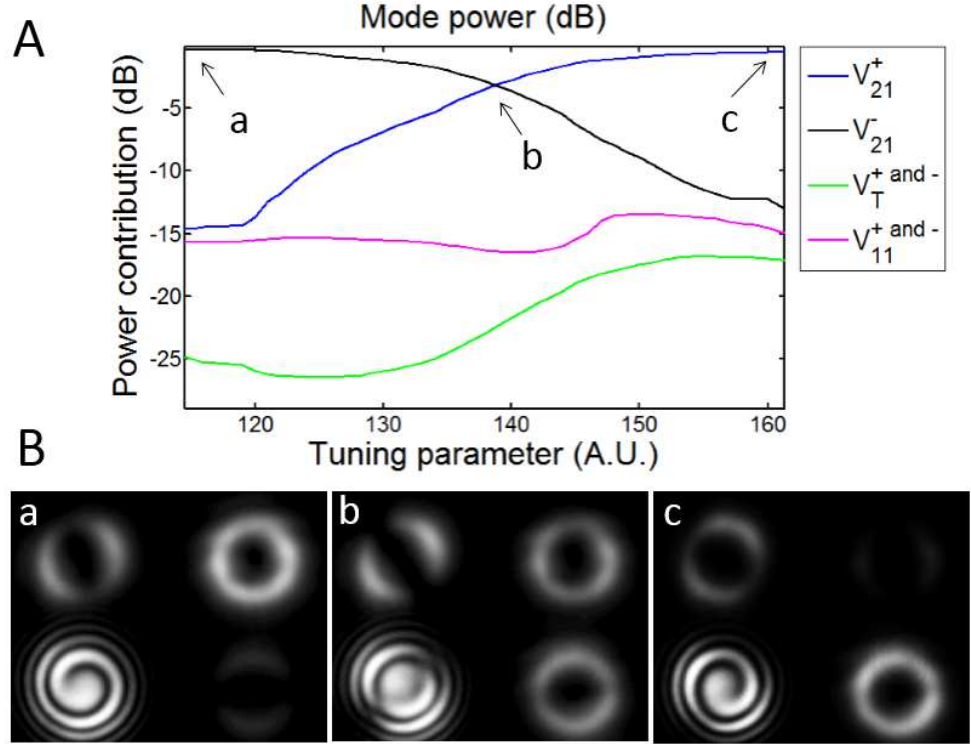


**Figure 5.4:** Ring method analysis applied in real time. **(A)** Mode powers in time during continuous adjustment of the paddles of PolCon2 (on the vortex fiber) to obtain desired OAM state superposition. **(B)** Camera images of the three positions (a-c).

fashion.

Few comments on the experimental limitations of the Ring technique need to be mentioned. In particular, we noticed that the beam-splitters we used had  $\approx 3\%$  transmission difference for s and p polarization, and were slightly birefringent. Both of these factors underestimate the measured vortex mode purity. Since the modal content can be determined using only two polarization projections, we were able to simplify the setup at the expense of not having the four projections. By doing this, we observed a 6 dB lower power for the  $V_T^{+, -}$  modes, suggesting that the use of better optical components can enable more accurate purity measurements. In addition to the optical components, we noticed that the camera dark noise level introduces a limit

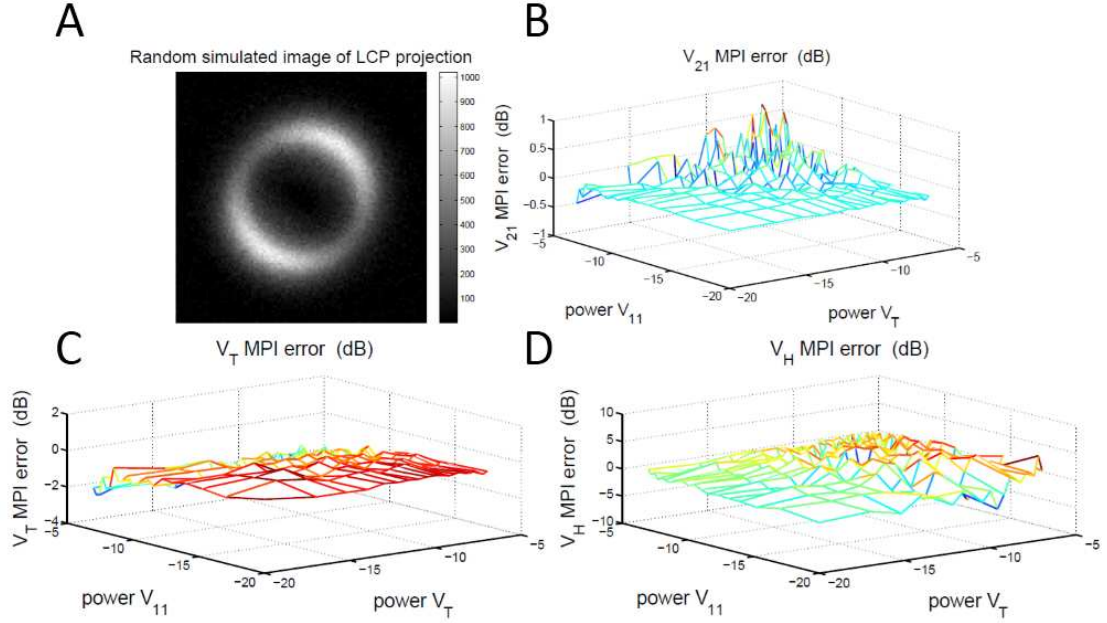


**Figure 5.5:** Ring method error estimation. (A) Random simulated image created as an weighted average of the six modes  $V_{21}^{+,-}$ ,  $V_T^{+,-}$  and  $V_{11}^{+,-}$  with randomized phases (dark and shot noise were also accounted for). (B-D) Estimated modal power error with respect to different initial modal powers for (B)  $V_{21}^+$ , (C)  $V_T^+$  and (D)  $V_{11}^+$  modes. We see that errors on average increase as input powers of spurious modes increase, indicating that the assumed 'dominant mode model' is no longer valid. For this reason calculations were only done for powers  $< -5\text{ dB}$  with respect to total power.

for the  $\mathbf{V}_{21}^{+,-}$  vortex state sensitivity of 20 dB. Note that this limit does not apply to the  $\mathbf{V}_T^{+,-}$  and  $\mathbf{V}_{11}^{+,-}$  modes, as their amplitudes are obtained from the interference effects and not the DC power measurements. We expect that a camera with lower dark-noise count will improve this sensitivity too.

In addition to the modal weights, relative phase information can also be extracted by analyzing four independent polarization projections (Berry et al., 1977). However, while we acquire four polarization projections simultaneously, only three of them are independent ( $H + V = RC + LC$ ). Therefore, in our case, only half of the Poincaré

sphere can be covered (Fig. 5·6 B).

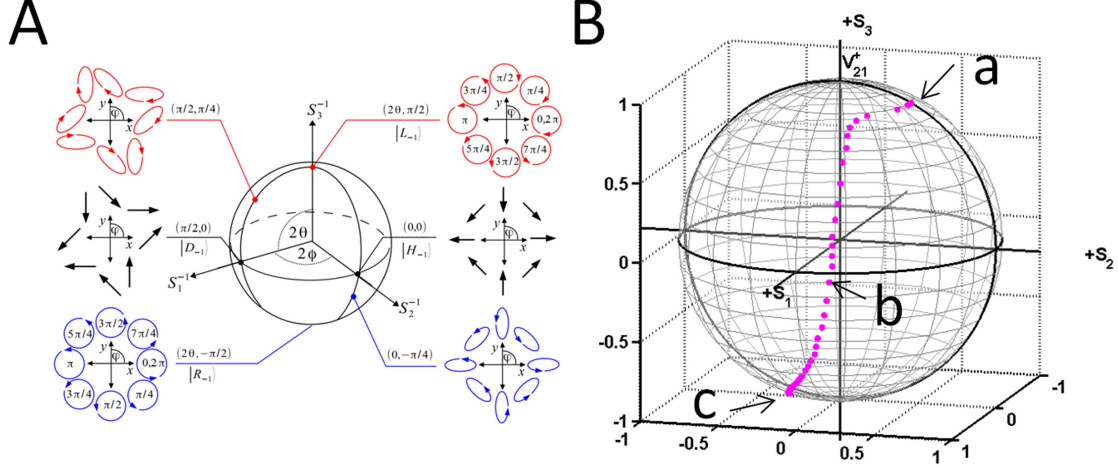


**Figure 5·6:** (A) Concept of higher-order Poincaré sphere (taken with permission from (Milione et al., 2011)). (B) Reconstruction of a relative phase between two OAM states for the same case of tuning OAM shown in Fig. 5·4.

## 5.2 Cutback measurements

In this section, we analyze the relative mode powers for different fiber lengths using the ring technique described previously (Sec. 5.1). We show that mode purity deteriorates with length, nevertheless still preserving good purity (Bozinovic et al., 2011b; Bozinovic et al., 2011a). Since mode coupling is affected by the wavelength of light as well as the fiber temperature (Marcuse, 1974), at a particular fiber length, relative modal powers were determined for 500 different wavelengths within a 0.5nm range. Figure 5·7 (A-C) shows the relative mode powers for the three dk11OD115 lengths (360m, 720m, and 1020m) in the case of high purity,  $> 20dB$ , OAM<sup>+</sup> mode excitation at 1550 nm. Note how the OAM mode power deteriorates with length and the relative mode powers of other modes increase. A stress-induced microbend grating with  $L = 40mm$  length and  $\Lambda = 475\mu m$  grating-period was used for mode generation,

and prior to the grating, the fiber was securely taped to be free of any movements that would change phase or polarization, and therefore, coupling conditions at the grating input. The results were obtained by measuring modal power ratios for a long fiber length first, which was then sequentially shortened (this procedure ensures that the same input launch conditions existed for all lengths that were measured). As we observed, different relative mode powers have been obtained for the different wavelengths due to wavelength-induced phase changes, that in turn induced different coupling conditions. We note that a larger bandwidth source would effectively perform averaging over wavelengths, but emphasize the only narrow linewidth source can be used to ensure visibility of the modal interference, necessary for power calculations.

Figure 5·7 (D) shows results of relative mode powers for the several fiber lengths, where each point denotes a mean relative mode power value with one standard deviation from the mean. After  $1.1\text{km}$  of propagation of the desired OAM modes, less than  $-10\text{dB}$  of the input power leaked into the  $LP_{01}^{\pm}$  and the  $TM_{01}$  and  $TE_{01}$  modes. we use a tunable continuous wave external cavity laser (CW-ECL, Agilent 8168F) with  $100\text{kHz}$  linewidth (coherence length  $3\text{km}$ ) to capture necessary modal interference effects between the modes after  $1.1\text{-km}$  of propagation in the vortex fiber (the maximum optical-path length delay, given by  $\Delta n_g L = 3\text{m}$ , where  $\Delta n_g$  is the difference in group index between modes, is  $\approx 3$  meters).

In addition to wavelength, the relative mode powers are also measured in time (Fig. 5·7E), indicating temporal stability on the order of hours (though additional correction adjustments were needed on a longer time scale).

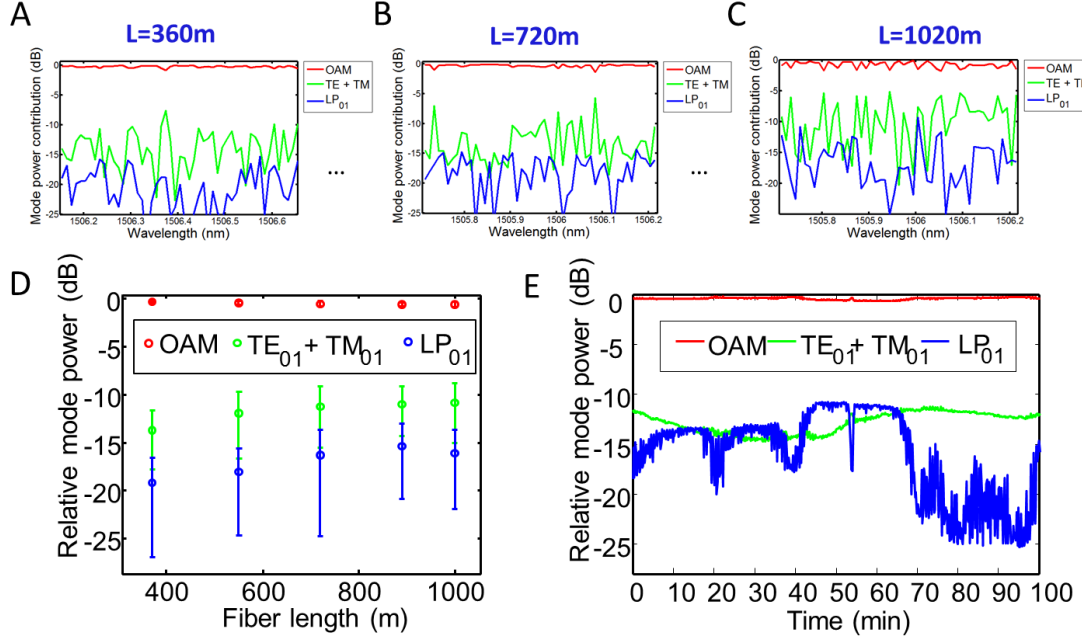


**Figure 5.7:** (A-C) Relative mode powers for three different lengths for the case of high purity ( $> 21\text{dB}$ )  $OAM^+$  mode excitation at 1550 nm (OAM power refers to combined  $OAM^+$  and  $OAM^-$  mode powers, and  $LP_{01}$  refers to combined powers of the two  $LP_{01}^\pm$  states). (D) Measured modal power ratios as a function of fiber length for the same case as in A-C. (E) Relative mode powers with respect to time, showing the temporal stability of the OAM modes.

### 5.3 Regression analysis

In addition to the Ring method that uses the dominant mode approximation, here we describe a method that applies more rigorous mathematical analysis to obtain relative mode powers without the dominant mode approximation (Golowich et al., 2013). Here we describe the idea of the method and would like to refer a reader to the mentioned paper for more details. In particular, method is based on regression analysis of four polarization projections, and includes analysis of not only azimuthal intensity distributions at one radius, but the total spatial intensity distribution of the modes. In addition, the method also relies on pure mode intensities as prior

information. An additional advantage of the regression method is that it allows the relative phases of the modes to be obtained (for example the relative phase difference between  $HE_{21}^{even,odd}$  modes), in addition to the modal powers.

Figure 5·8 (A) shows calculated modal powers after  $L = 3m$  long propagation in a dk11OD100 fiber. Power were estimated for each of the three pairs of modes  $HE_{11}$ ,  $HE_{21}$ , and  $TE_{01}/TM_{01}$ , for a range of wavelengths surrounding the microbend grating resonance for the  $HE_{21}$  mode. The  $HE_{11}$  mode power vs wavelength was also compared with the one obtained using OSA loss-spectrum measurements (Sec. 4.1.2), and a good agreement has been observed (Fig. 5·8 B). During this measurement, the two OAM states comprising  $HE_{21}$  modes were excited with roughly equal power and stable relative phase as calculations confirmed (Fig. 5·8 C-D). For more details on the technique, we would like to refer a reader to (Golowich et al., 2013).

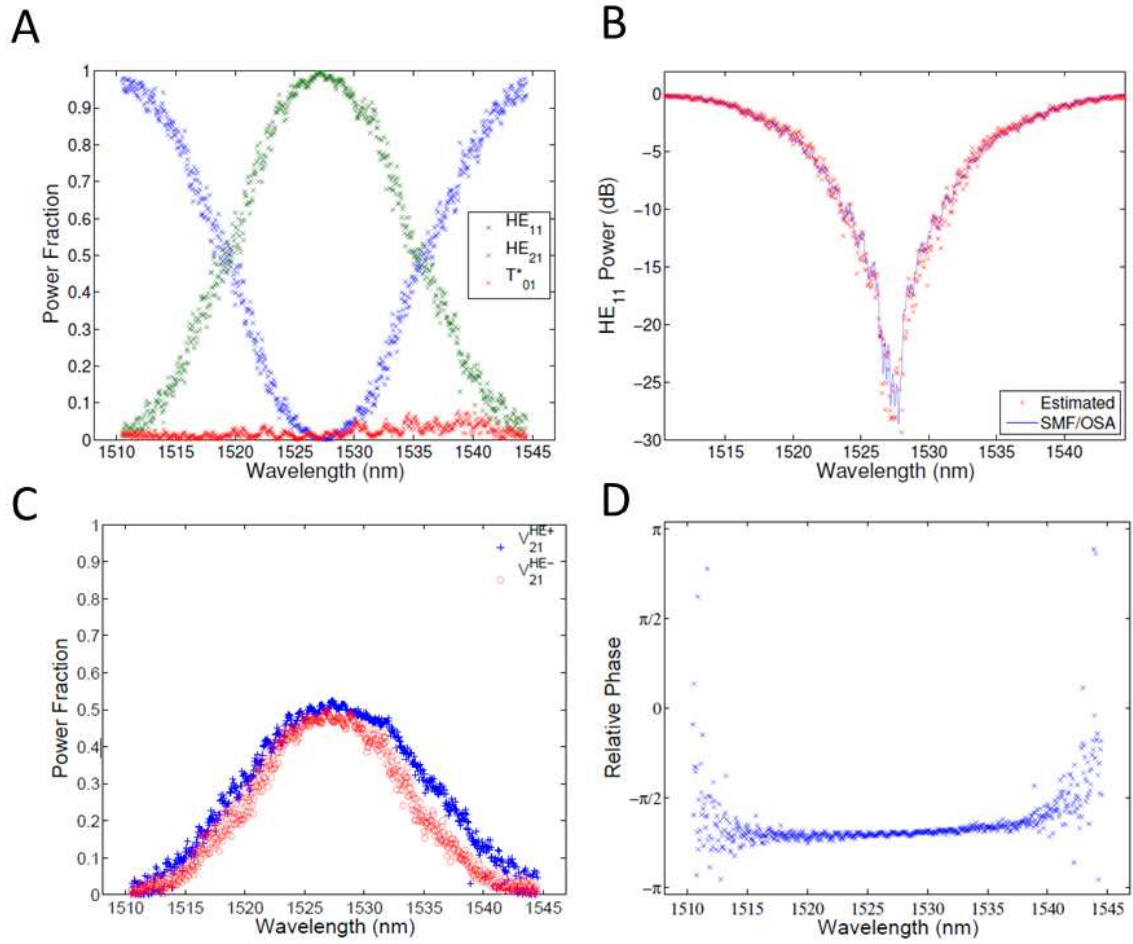


**Figure 5.8:** (A) Power fraction in the fundamental, transverse, and  $HE_{21}$  pairs; (B) Power estimated in the  $HE_{11}$  modes by regression analysis (red crosses) and by coupling into a SMF (blue curve). (C) Estimated power fraction of each of the two OAM states; (D) Estimated relative phase of the two OAM states.

## Chapter 6

# OAM Mode-Division-Multiplexing (MDM)

Having studied OAM mode propagation in vortex fibers, we now focus attention to multiplexing and demultiplexing of OAM-carrying beams. Multiplexing, in essence, represents a concept for which several data channels are combined onto a shared resource with the purpose of achieving higher capacity of the resource (in our case fiber). For example, wavelength-division-multiplexing (WDM) combines several data channels at different wavelengths in a fiber, while time-division-multiplexing (TDM) takes data that is separated in time, and arranges them serially (Agrawal, 2010). Several classical and quantum communications experiments have performed OAM-MDM in free space using free-space optics and fork/spiral holograms (Gibson et al., 2004; Gröblacher et al., 2006; Wang et al., 2012). Other free-space methods have achieved OAM-MDM using specially designed phase plates (Berkhout et al., 2010; Sullivan et al., 2012), photonic integrated circuits (Su et al., 2012; Cai et al., 2012). Here we develop fiber OAM-mode-division-multiplexing (OAM-MDM) that aims to combine two fundamental modes ( $s = \pm 1$ ) and OAM-data-carrying beams ( $l = \pm 1$ ) into a single vortex fiber (Bozinovic et al., 2012b). For this purpose we use SLM-based OAM mode generation method described previously (Sec. 4.2) and free-space optics for collinear alignments of the modes. In the next chapter, we use the system developed here for our systems experiment.

## 6.1 Multiplexing 4-mode system

The concept of the simplest OAM-MDM system, that takes into consideration only  $l = 0, \pm 1$  states, is shown in Fig. 6·1. Two  $l = \pm 1$  OAM and two fundamental circular polarized (spin of  $s = \pm 1$ ) modes, are multiplexed in one fiber. In our case, we note that  $l = \pm 1$  states also have spin of  $s = \pm 1$  (Sec. 5.1) since those are true eigenmodes. The four modes are considered to be multiplexed in both polarization and OAM, and are considered independent channels for data transmission.

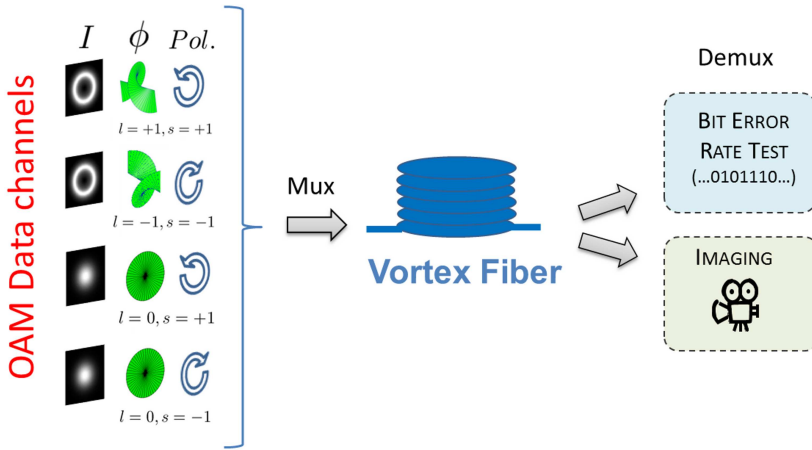


**Figure 6·1:** OAM division multiplexing principle. Four modes with distinct values of OAM ( $l$ ) and spin ( $s$ ) values are multiplexed into a specialty fiber, propagated and analyzed at the output using bit-error-rate tester (BERT) and/or imaged using near-IR camera.

One of the factors that plays an important role in transmission systems of practical interest is power consumption, and multiplexing with low loss is always preferred. Some methods for OAM beam generation that we mentioned previously are also suitable for low-loss OAM-MDM, in particular, methods that use free-space optics (Berkhout et al., 2010; Sullivan et al., 2012) and photonics integrated circuits (PIC) (Su et al., 2012). However, these methods are still at their early stages of development, and offer unsatisfactory level of OAM mode quality. For this reason, and also because

we focus here on OAM-MDM as a proof of concept at this point, we will adopt a much simpler, albeit lossy approach for OAM-MDM, of using beam-splitters to combine several OAM beams before their coupling into a single vortex fiber.

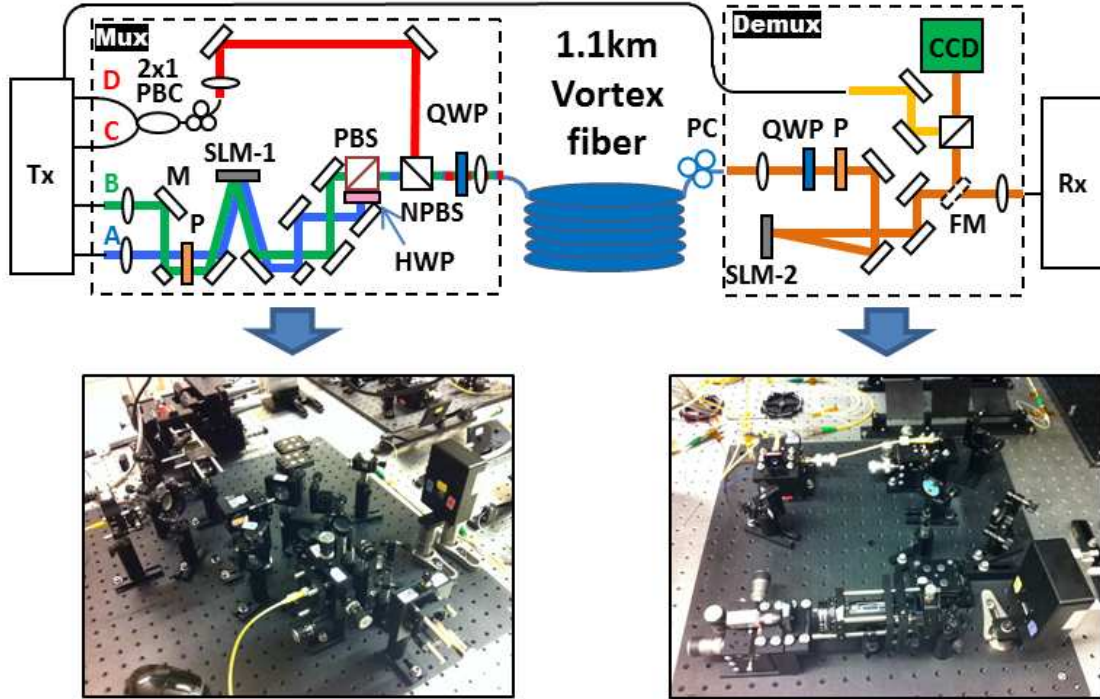


**Figure 6·2:** Detailed (de) multiplexing experimental setup: signal from the transmitter (Tx) is split into four individual fiber arms. Two of the arms were converted into OAM modes using LCoS-SLM. Two fundamental modes were added collinearly to the two OAM modes using 3dB-lossy non-polarizing beam-splitter. All four modes are then coupled into vortex fiber, and analyzed at the output after being de-multiplexed accordingly. Acronyms: flip mirror (FM), half wave plate (HWP), (non)-polarizing beam-splitter ((N)PBS), polarization beam combiner (PBC), polarization controller (PC), mirror (M), quarter wave plate (QWP).

We designed detailed experimental (de)multiplexing setup (Fig. 6·2) to perform multiplexing of four channels discussed in Fig. 6·1). Here we adopt LCoS-SLM generation method for the OAM mode (Sec. 4.2). Two of the four channels were con-

verted into the OAM modes (modes A and B) using reflection of the fork-holograms of topological charge  $\pm 1$ , created using LCOS-SLM (X10468-8, Hamamatsu). The other two,  $LP_{01}$ , modes were left unchanged (modes C and D). 6-axis fiber stage positioner (Thorlabs, MAX601D) was used for input coupling into the vortex fiber. Precise optical alignment was used to avoid any offset coupling, which can otherwise introduce strong crosstalk (offset coupling of  $< 50\text{nm}$  was achieved). Incident angle is also important for input coupling but less critical than the offset. Fiber coupling losses were 0.7dB for  $LP_{01}$  and 1.1dB for *OAM* modes. In addition to alignment, setup was optimized for low crosstalk at 1550nm using set of polarization controllers at the input and on the vortex fiber. Vortex fiber spool was also thermally isolated using custom-made fiber storage.

## 6.2 Demultiplexing and imaging

After propagation through 1.1 km of vortex fiber, demux setup was designed to sort modes according to their OAM and spin. The spin sorter was comprised of a quarter wave plate and a polarizer, while the OAM sorter was comprised of another LCOS-SLM. To demultiplex the four modes, we have used two orientations of a demultiplexing quarter-wave-plate ( $\pm 45^\circ$ ), and three SLM holograms ( $l = 0, \pm 1$ ). Being only a proof-of-concept, demultiplexing setup was created so to study only one mode at a time. The setup was designed with an option for bit-error-rate (BER) measurements, as well as an option of taking near-field images of the mode spatial intensity/phase distributions.

## 6.3 Cross-talk and multi-path-interference

Crosstalk and multipath interference (MPI) are well known impairments that increase the BER of direct-detection communication system (Ramachandran et al., 2003; Ra-

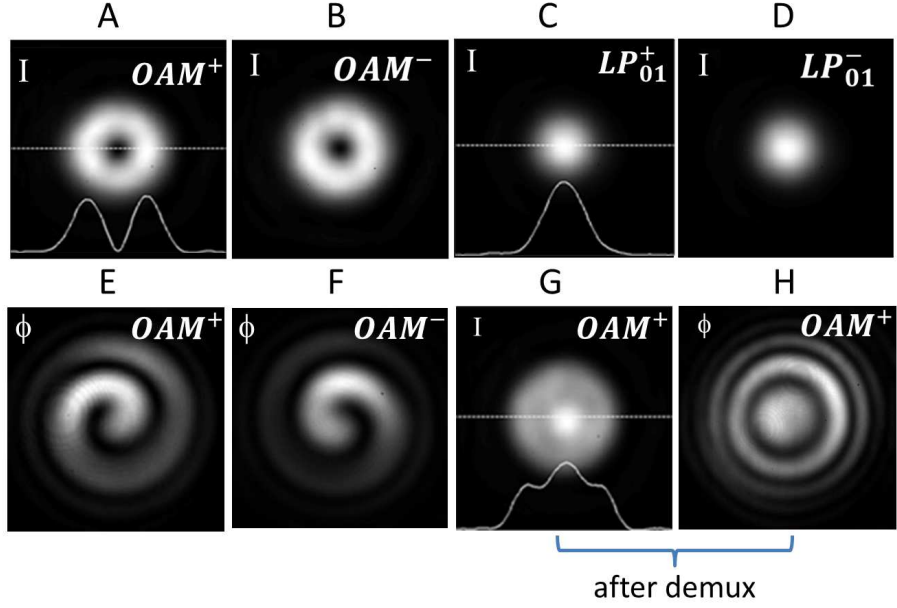


**Figure 6.3:** NIR camera images of the channel outputs after 1.1km fiber propagation using 50GBaud modulated ECL source (linewidth of 0.4nm). (A-D) Intensity images (E, F) Phase images of  $OAM^+$  and  $OAM^-$ . (G, H) Intensity and phase of the  $OAM^+$  mode after demultiplexing using inverse fork pattern.

machandran, 2005) as they introduce random power fluctuations (Fig. 6.4). While crosstalk indicates how much of the mode power leaked into the other modes, MPI measures how much power went out and back into the desired mode. Here, crosstalk and MPI were measured using following equations (given is example for mode A):

$$XT_A[dB] = P_{B+C+D}[dBm] - P_{\text{all modes}}[dBm], \quad (6.1)$$

$$MPI_A[dB] = 20\log_{10} \frac{10^{\frac{\Delta}{20}} - 1}{10^{\frac{\Delta}{20}} + 1}, \quad (6.2)$$

where  $XT$  denotes cross-talk,  $P$  power, and  $\Delta$  represents peak-to-peak power fluctuations in time, in dB (also defined in Fig. 6.4 B). Examples of cross talk and MPI measurements, as well as measured values for all the modes are given in Fig. 6.4.

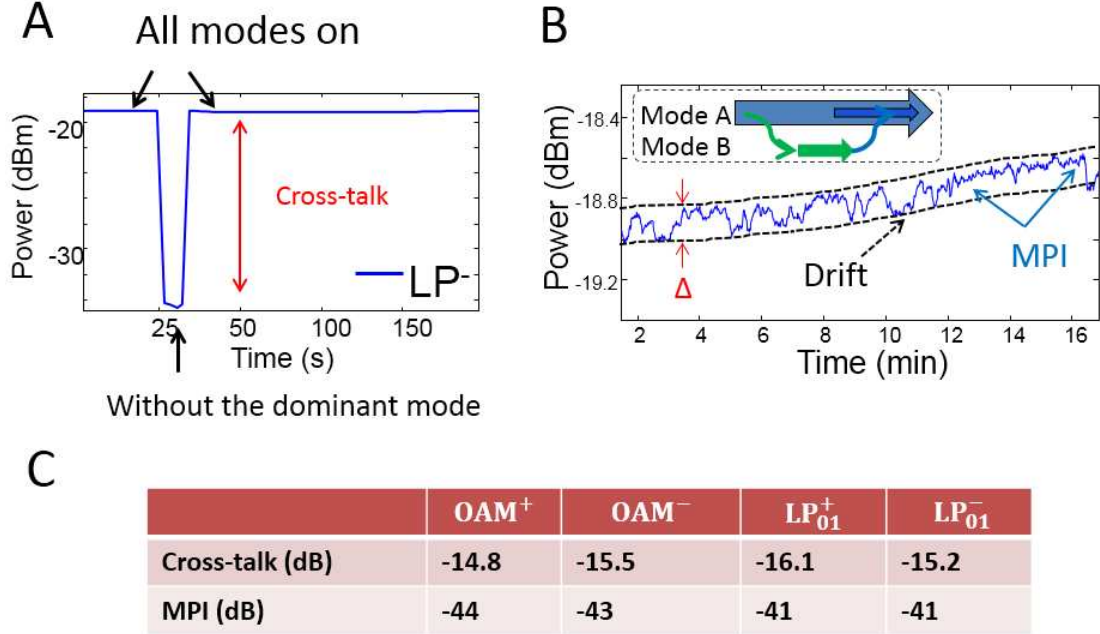


**Figure 6.4:** Cross-talk and Multipath interference. **(A)** Cross-talk measurement example **(B)** Example of the  $LP_{01}^+$  mode power drift (attributed to the cross-talk and free-space optics) and power fluctuations (due to multipath interference - MPI). (Inset) Cross talk and MPI mechanisms; mode A can couple into mode B producing cross-talk, but certain amount of the power can couple back into mode A interfering with the original signal, producing MPI. Both cross-talk and MPI cause higher BER. **(C)** Table of measured values for cross-talk and MPI for all four modes.

## 6.4 Alignment procedure for 4-mode setup

The following describes alignment procedure (concluding with 2012/08/05). Stability is absolutely critical for mode coupling and an optical table that is used should be floated.

### Multiplexing

1. A design of the setup should be made (Fig 6.2) and all the components with mounts pre-assembled. The mounts that are commonly tuned should be distributed around the edges of the optical table if possible so the tuning is not

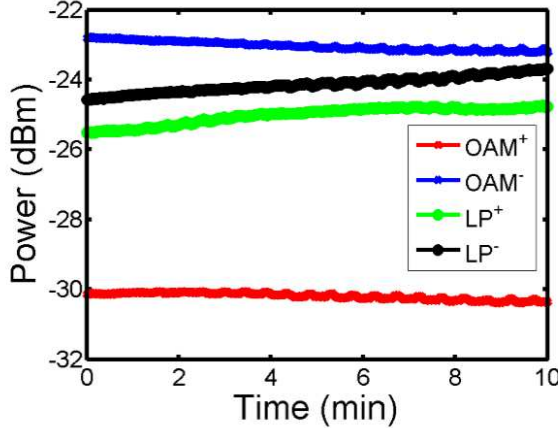


**Figure 6.5:** Drift and MPI of all four modes.

strenuous for the user. At this point, one should also think about the future packaging if needed.

2. Attach and collimate the 4 input channels (Fig 6.2) using IR cards.
3. (Course alignment) Place the mirror (M) instead of the proximal end of the coupling fiber, and image the beam onto the camera at the camera position 1 (see Fig. 4.8A). Turn on all the channels and mark ROI for each of them. Tune the channel mirrors until the channel beams more or less overlap.
4. (Fine alignment and astigmatism) Align the two mirrors of each channel to remove astigmatism. This is done by constantly scanning z-translation (focusing) back and forth and adjusting one mirror, then the other. All the beams should now overlap precisely without any astigmatism.
5. (Back-transmission) Remove mirror (M) and insert the vortex fiber. Distal end of the vortex fiber should be free-space coupled into SMF (using splicer) (note: do not splice the fibers to avoid offset coupling, even tiny amount can be detrimental). Send the light through the distal end of the vortex fiber and

observe the so-called back-transmission at the camera position 1 (see Fig. 4·8A) (note: all the mode channels should be turned off). Record the ROI. Adjust the free-space offset coupling between SMF and a vortex fiber so only  $LP_{01}$  is excited.

6. Turn off the SMF light source and turn back on the channels. Look at the back-reflection from the vortex fiber and move the translation stage until overlap with the ROI (recorded in the previous step) has been achieved.
7. Adjust pitch and x-translation of the back-transmission beam to remove astigmatism caused by the fiber end-face tilt.
8. Repeat for yaw and y-translation.
9. Remove the side of the distal end of the vortex fiber attached to the source, cleave it and image it (camera position 2, see Fig. 4·8A).
10. Adjust the zoom of the vortex fiber as well as fine tune the collimation for optimal power coupling.

### Demultiplexing

1. Prepare the optical components and mounts using the layout in Fig. 6·2.
2. Collimate the beam at the distal end of the vortex fiber (use the camera if a signal is too weak).
3. Attached the distal end of the SMF that you want to couple into and look at the back transmission on the IR card.
4. Using an IR card and a two mirrors alignment procedure, couple the light into the fibers (note: two mirrors alignment procedure requires placing the IR card

on one of the mirrors first, then adjusting yaw and pitch, repeating the procedure for the other mirror until convergence in alignment is achieved).

5. When reasonable alignment is achieved, small amount of power should be detected at the SMF output. Next, walk-in the beam by repeatedly adjusting x translation of the SMF stage and the yaw of the mirror closer to the coupling stage. Repeat for the y-translation and the pitch angle. Guiding the beam into the fiber at the proper angle is critical to achieve good coupling.

## Chapter 7

# OAM Transmission

In this chapter we present results of the systems experiments (i.e. data transmission using the 4-mode OAM-MDM setup described in the previous chapter (Ch. 6). Four modes include two  $l = \pm 1$  OAM modes multiplexed with the two fundamental polarization-multiplexed  $s = \pm 1$  modes. We first briefly describe the basics of data modulation formats and error-correction methods that we use. We then present results of the two system experiments that performed:

- 4-mode OAM-MDM at single-wavelength (Bozinovic et al., 2012b)
- 2-mode OAM-MDM using 10-channel WDM (Yue et al., 2013)

Using coherent detection and bit-error-rate (BER) measurement that, we demonstrate successful data transmission at 400Gbit/s using four OAM modes at a single wavelength, over 1.1 km of fiber. Furthermore, we achieve data transmission at 1.6Tbit/s using 10 wavelengths and two OAM modes (Bozinovic et al., 2012b).

### 7.1 Brief introduction in communication systems

From the very beginnings of communication systems, the desire for higher transmission capacities and, at the same time, the drive to reuse the existing transmission channels, have fueled the advancements of data modulation formats. First modulation formats were based of on-off keying, where bit of information was encoded in the amplitude of the electric signal ('1' when there is light and '0' for no light) (Fig. 7.1).

Later on, modulation formats started using frequency (or phase) of electric field to encode information (see frequency and phase shift keying in Fig. 7·1). Today, myriad

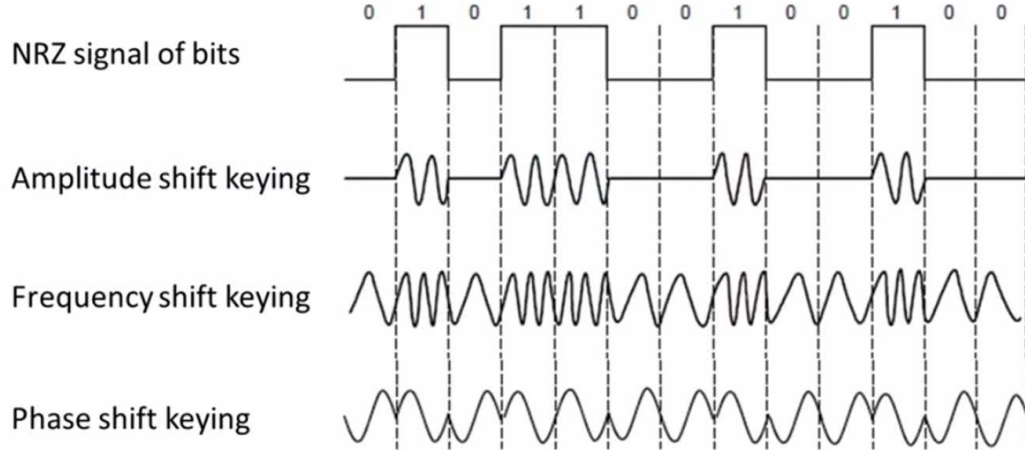


**Figure 7·1:** Basic modulation formats using amplitude and phase of the field. Non-return to zero (NRZ) denotes that signal doesn't go to zero between two bits that both carry '1'. With permission from Wikipedia, © Creative Commons.

of advanced modulation formats exists depending on capabilities of particular transmission systems, mainly separated into intensity and phase modulation groups (Fig. 7·2) (Winzer and Essiambre, 2006). While intensity modulation formats are typically detected directly Fig. 7·3 (A), the phase-modulation formats require a reference beam (also called local oscillator - LO) Fig. 7·3 (B). Not taking into account the nonlinear effects of a fiber, a capacity ( $C$ ) of any channel (with direct or coherent detection) is  $C = B \log_2(1 + SNR)$ , where  $B$  is the bandwidth  $B$  and  $SNR$  is the signal-to-noise-ratio in the channel (Shannon, 1948). In the case of direct-detection, it can be shown that the capacity is restricted with the  $SNR$  of the light source. However, in the case of coherent-detection, the  $SNR$  of the channel is predominantly determined by the  $SNR$  of the LO. In a nutshell, due to the fact that LO power does not suffer from the losses as much as the signal from the other end of the fiber, coherent-detection approach has the advantage over direct-detection, and is becoming a predominant

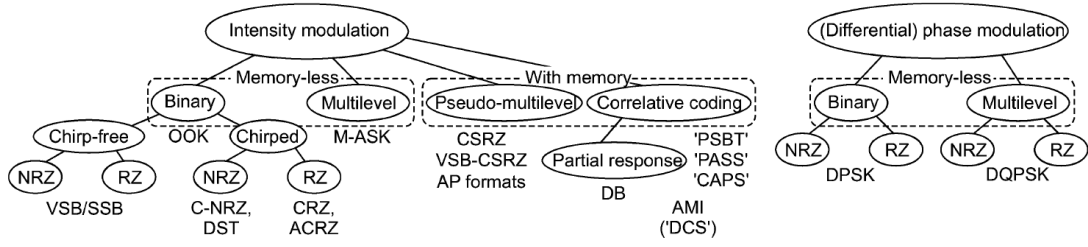
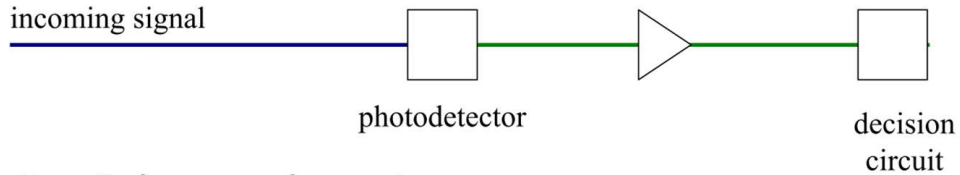


**Figure 7·2:** Advanced modulation formats (Winzer and Essiambre, 2006). For us most important formats is differential quadrature phase shift keying (DQPSK) that we use in our systems experiment. For full list of acronyms consult (Winzer and Essiambre, 2006). With permission from (Winzer and Essiambre, 2006), © IEEE.

detection method today. While the description of the modulation formats in Fig. 7·2

### A – Direct detection



### B – Coherent detection

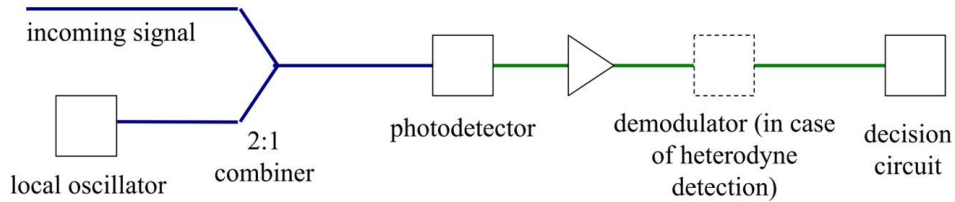


**Figure 7·3:** Direct (A) vs Coherent (B) modulation formats. With permission from Wikipedia, © Creative Commons.

is beyond the scope of this work, we focus on one that we used for our experiments, namely, quadrature phase shift keying (QPSK). In essence, QPSK is an example of a four-state system (also used terms for states are levels or symbols). What this means is that both transmitter (Tx) and receiver (Rx) can send and/or receive four possible states. For each state they agree on a bit combination, for example, '00', '01', '10'

and '11'. In an example of an intensity modulation, a laser with four levels of power use say 0W to transmit '00', 1W to '01', 2W to '10' and 3W to '00'. In the case of QPSK, four levels are in fact encoded in four different phases of a wave. For example, a wave with frequency  $f_c$ ,

$$\sin(2\pi f_c t + (2n - 1)\frac{\pi}{4}), \quad n = 1, 2, 3, 4 \quad (7.1)$$

can have four different phases  $\pi/4$ ,  $+3\pi/4$ ,  $5\pi/4$  and  $+7\pi/4$ , for  $n = 1, 2, 3, 4$ . If the receiver can detect the phase of the wave, it can recover the bit sequence. We briefly note that in addition to 4-level QPSK, 16-level modulation can be used in which case it is called 16-quadrature amplitude modulation (16-QAM). For a detailed explanation, implementation as well as different variants of the QPSK and 16-QAM method, we recommend (Ip et al., 2008).

Our QPSK concept is shown on Fig. 7.4 (A-B). A sender can encode information in a  $\pi/4$ ,  $+3\pi/4$ ,  $5\pi/4$  and  $+7\pi/4$  phase of a beam, and a receiver can decode the bits as '11', '01', '00' and '11', respectively. Due to dispersion, polarization-dependant loss and/or gain, and nonlinear effects, the detected phase can be slightly different from the one being sent. If the difference is too large, an erroneous bit can be received, and a bit-error-rate (BER) will increase. In telecommunication, an eye pattern, also known as an eye diagram, is an oscilloscope display in which a digital data signal from a receiver is repetitively sampled and shown on a vertical scale, while the data rate is used to trigger the horizontal sweep. In other words, it represents the synchronized superposition of all possible realizations of the signal of interest viewed within a particular signalling interval. It is so called because, for several types of coding, the pattern looks like a series of eyes between a pair of rails. It is an experimental tool for the evaluation of the combined effects of channel noise and intersymbol interference on the performance of a pulse-transmission system. Typical noiseless and noisy case

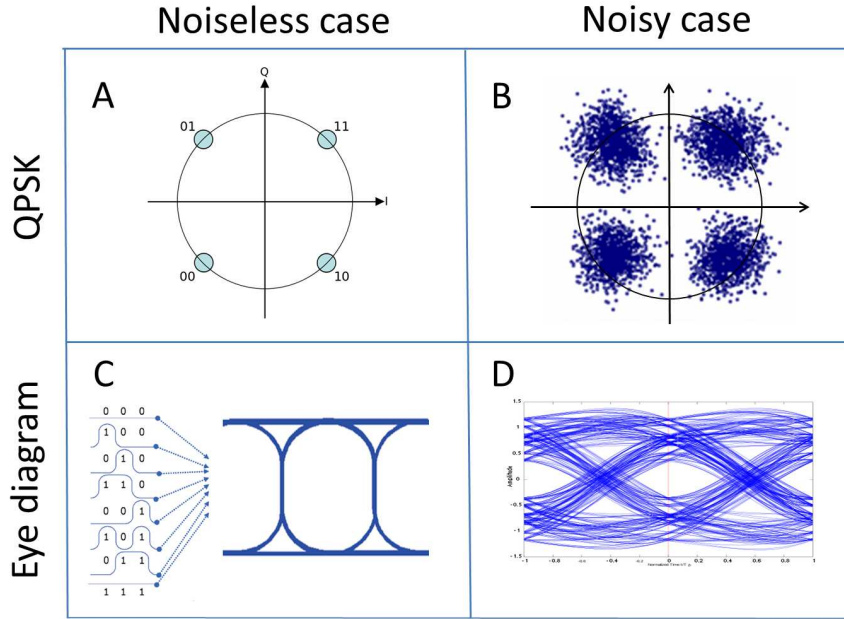


**Figure 7.4:** Concept of quadrature phase shift keying (QPSK) and eye-diagram for bit-error-rate testing. **(A)** Ideal QPSK constellation. A sender can encode information in a  $\pi/4$ ,  $+3\pi/4$ ,  $5\pi/4$  and  $+7\pi/4$  phase, corresponding to 11, 01, 00 and 11 bit combination. Therefore, a phase can carry 4 possible states. **(B)** Noisy case. A phase of light can suffer changes due to fiber impediments, and in the noisy case, wrong phase can be detected, and errors in transmission can occur. **(C)** Concept of an eye diagram in the case of intensity modulation. Train of pulses carrying bits can be overlapped to create an eye-shaped diagram. **(D)** In a noisy case, distortion can cause "eye-closing" introducing errors in transmission. Similar eye diagram can be observed in the QPSK case. C and D with permission from Wikipedia, © Creative Commons

of an eye diagram is shown in Fig. 7.4 (C-D).

Depending on a type of application, different levels of errors are allowed in the system. In a typical communication system, a BER level on the order of  $10^{-12}$  is tolerable. However, this level can be quite challenging to achieve using the methods we have explained, and in addition to the physical means of sending information, so-called forward-error-correction (FEC) codes are used. The central idea is that the sender encodes a message in a redundant way. The redundancy allows the receiver

to detect a limited number of errors that may occur anywhere in the message, and often to correct these errors without retransmission. This note that FEC gives the receiver the ability to correct errors without needing a reverse channel to request retransmission of data, but at the cost of a fixed, higher forward channel bandwidth.

An example of a FEC code is the Hamming (7,4) code (Hamming, 1950). This code encodes 4 bits of data into 7 bits by adding 3 parity bits. If the error of any one bit out of 7 would occur, the sequence can detect the error, which can be corrected. If the medium is too noisy so that 2 out of 7 bits are flipped, error will be detected. However, the likelihood for two bits to be flipped is much smaller than in the case of one. The redundancy of the code can be described with the ratio of data bits vs total number of bits (in the case of Hamming (7,4) code this rate is  $4/7 = .571$ ). Today, FEC codes with much smaller redundancy has been implemented such as: convolution code, Low-density parity-check (LDPC), and many others. In our system, we used FEC that can tolerate BER with the threshold of  $3.8 \times 10^{-4}$ . Detailed explanation of the FEC codes goes beyond the scope of this dissertation (for more details we recommend (Freeman, 2002)).

With basic knowledge of modulation formats and FEC codes we now present results of fiber-based OAM-MDM experiments in the vortex fiber.

## 7.2 4-mode OAM-MDM

Here we demonstrate OAM-MDM data transmission feasibility of the 4-mode system described in Ch. 6, by sending 50 GBaud (1 Baud = 1 symbol/s), QPSK data, at a single wavelength, and over 4 mode-channels. The detailed experimental OAM-MDM setup is shown on Fig. 7·5. For the single wavelength experiments, a CW-ECL operating at 1550 nm was first modulated using a 50 GBaud QPSK signal, and subsequently split into four arms that were delayed sufficiently to obtain four de-

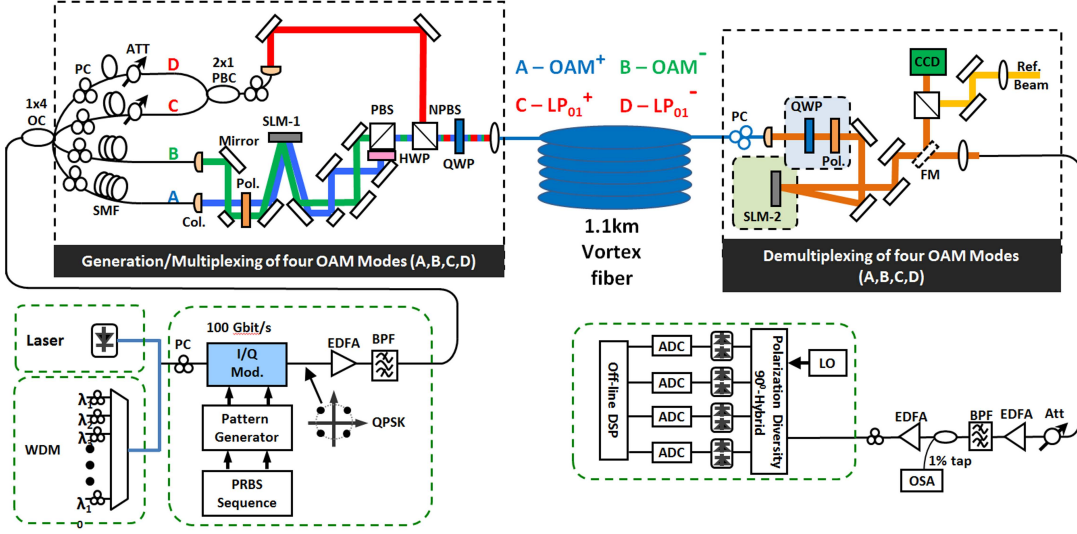


**Figure 7-5:** Systems experiment setup: signal from the laser or WDM source is modulated, amplified using an erbium doped fiber amplifier (EDFA), filtered using a band pass filter (BPF) and split into four individual fiber arms (two in the case of the WDM experiment). Two of the arms were converted into OAM modes using the input SLM. Two fundamental modes were also collinearly aligned with the two OAM modes using a beam-splitter, and all four modes were coupled into the fiber. After propagation, the modes are demultiplexed sequentially and sent for coherent detection and offline digital signal processing (DSP). Acronyms: ADC - analog digital convertor, Att - attenuator, FM - flip mirror, LO - local oscillator, OC - optical coupler, (N)PBS: (non)-polarizing beam-splitter, PBC - polarization beam combiner, PC - polarization controllers, PC-SMF - polarization controller on SMF, PC-VF - polarization controller on vortex fiber. OC: optical coupler, (N)PBS: (non)-polarizing beam-splitter, PBC: polarization beam combiner, PC: polarization controller

correlated data channels (two for the WDM experiments in the next section). Two of the four channels were converted into the  $OAM^{\pm}$  modes (modes A and B) using reflection off fork-holograms of topological charge  $\pm 1$ , created using the LCOS-SLM (X10468-8, Hamamatsu). The other two,  $LP_{01}$ , modes were left unchanged (modes C and D). A 6-axis fiber stage positioner (Thorlabs, MAX601D) was used for input coupling into the vortex fiber. Precise optical alignment enabled avoiding any offset coupling, which can otherwise introduce strong crosstalk (offset coupling of  $< 50\text{nm}$

was necessary and achieved). We found that the incident angle (of light on the fiber facet) to also be important for input coupling, but less critical than the offset. Fiber coupling losses were 0.7dB for the  $LP_{01}$  and 1.1dB for the OAM modes.

After alignment, the four polarization controllers at the channel inputs (A, B, C and D on Fig. 7·5) would be adjusted first to equalize the output channel powers. Next, the polarization controller on the vortex fiber (PC-VF in Fig. 7·5) would be adjusted to obtain  $OAM^\pm$  states at the vortex fiber with the smallest cross-talk (a minimum value of -20dB was obtained). Finally, the polarization controller on the input SMF (PC-SMF) was adjusted to obtain  $LP_{01}^\pm$  modes at the output with the smallest crosstalk ( $< -30dB$  was achieved). Note that we did not necessarily have  $LP_{01}^\pm$  states at the channel inputs (C, D) but rather states with arbitrary polarizations; however,  $OAM^\pm$  states were ensured at both input and output. The vortex fiber spool was thermally isolated using a custom-made Styrofoam box. Polarization controllers needed adjustments in roughly one-hour increments to account for components drifts and temperature fluctuations. We note that automated polarization controller feedback corrections are commonly used techniques in conventional polarization-division multiplexed (PDM) systems (Sunnerud et al., 2002).

Figure 7·6 shows constellation diagrams in the case of the 4-mode OAM-MDM experiment in the single-channel as well as all-channel case, using 50 GBaud non-return-to-zero (NRZ) QPSK at 1550 nm. BERs are measured for two cases: when only one channel is used for data transmission (single-channel case), and when all four channels are simultaneously populated with distinct (decorrelated) data-streams (all-channels case) (Fig. 7·7 B). In the single-channel case, the largest received power penalty for achieving a BER of  $3.8 \times 10^{-3}$  (the threshold BER level at which forward-error-correction (FEC) algorithms ensure error-free data transmission) is 2.5 dB, mainly due to channel MPI. In the all-channel case, this largest power penalty increased to

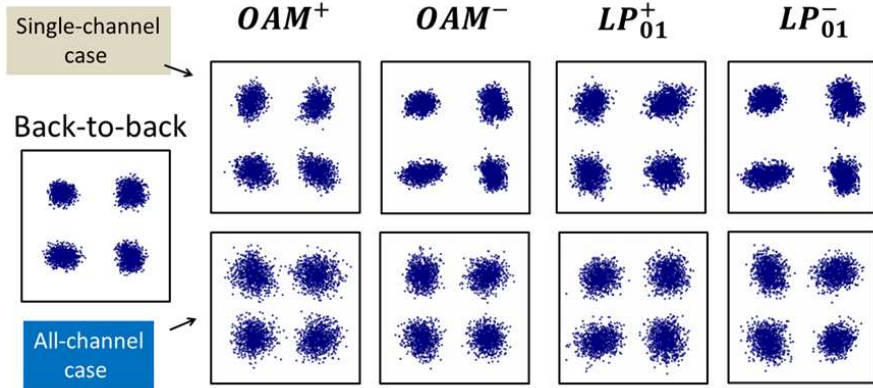


**Figure 7.6:** Constellation diagrams in the case of 4-mode OAM-MDM, with 50 GBaud NRZ-QPSK,  $\lambda = 1550\text{nm}$ , for the single-channel, and all-channel cases. Note the larger distortion of the constellations in the all-channel case.

4.1 dB, mainly due to channel cross-talk. In the latter case, a total transmission capacity at 400 Gbit/s below the FEC limit is achieved.

### 7.3 2-mode OAM-MDM

In addition to the single wavelength demonstration, we used WDM to further extend the capacity of our system (Fig. 7.8 A). According to mode coupling theory (Marcuse, 1974), cross-talk in coherent systems depends on a beam phase that, in turn, depends on the wavelength. Thus, optimizing our system to yield two orthogonal, pure  $OAM^\pm$  states at one wavelength implies that, at other wavelengths, the  $OAM^\pm$  states will, to a certain extent, couple into each other. A more advanced transmitter with individual wavelength channel polarization control could, in principle, be used to mitigate this effect. In addition, extraneous contributory factors such as the wavelength dependence of the SLM and other free-space optical components can also affect the cross-talk. For these reasons, only two OAM modes and 10 WDM channels (from 1546.64 to 1553.88 nm) are chosen for our WDM experiment. (the boxed region in Fig. 7.8 B), illustrating wavelengths at which crosstalk was low). Reduction to

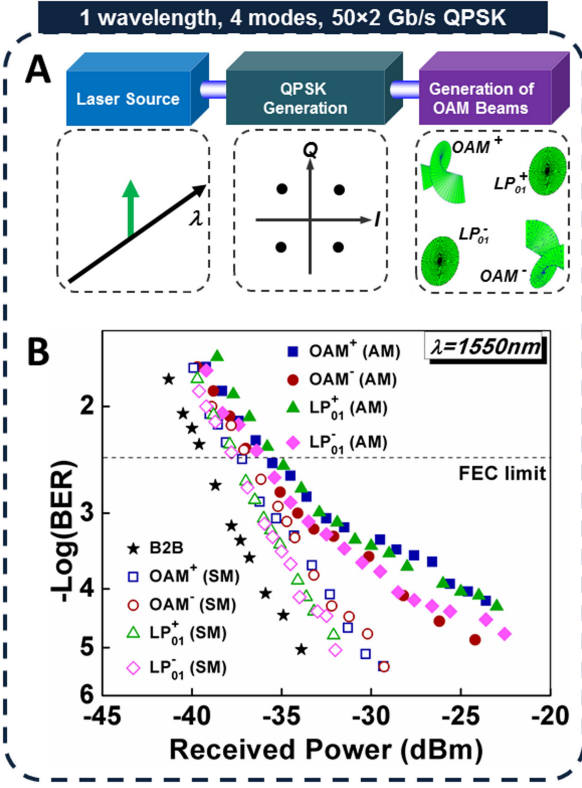


**Figure 7.7:** Data transmission experiments. (A) Block diagram of  $50 \times 2$  Gb/s QPSK signal transmission over a single wavelength carrying 4 modes in the vortex fiber. (B) Measured BER as a function of received power for the single-channel (SC) and all-channels (AC) transmission case.

two modes allowed us to choose a more complex modulation format (16-quadrature amplitude modulation) for data transmission, yielding higher spectral efficiency, albeit with a lower baud rate of 20 GBaud. While the BER of the two modes varied somewhat due to crosstalk (Fig. 7.8 C), transmission of 20 channels (OAM-MDM and WDM), resulted in a total transmission capacity of 1.6 Tb/s under the FEC limit.

Figure 7.9 shows additional results of the system experiment with 2-OAM modes, 10 wavelengths and 16-QAM signal modulation. The optical spectra of the modulated signal just before the input at the fiber, and after transmission in the  $OAM^+$  mode followed by the demux are plotted in Fig. 7.9 (A). We can see that all WDM channels

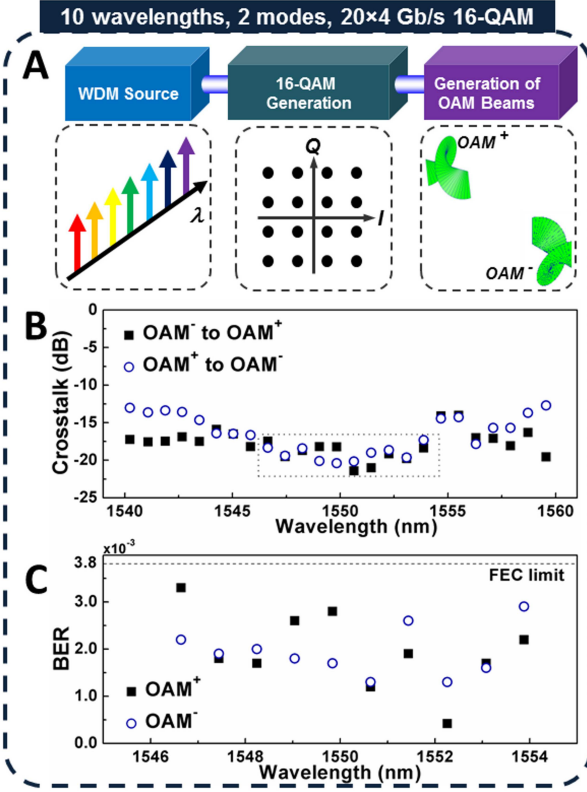


**Figure 7.8:** (A) Block diagram of 20x4 Gb/s 16-QAM signal transmission over 10 wavelengths carrying 2 modes in the vortex fiber. (B) Measured crosstalk between  $OAM^{\pm}$  modes as a function of wavelength. (C) BER as a function of wavelength for  $OAM^{\pm}$  modes in the WDM system.

have a 25dB OSNR after demultiplexing. Figure 7.9 (B) shows constellations for a) 16-QAM back-to-back (B2B) data transmission, b)  $OAM^+$  mode at 1550.64 nm w/o crosstalk (XT) (one wavelength is on, one mode is on), c)  $OAM^+$  mode at 1550.64 nm w/ WDM XT (10 wavelengths are on, one mode is on), and d)  $OAM^+$  mode for WDM source w/ all XT (10 wavelengths are on, two mode are on). Note the gradual increase in distortion of the constellations as wavelengths and modes are added to the fiber. Figure 7.9 (C) shows measured BER curves for the OAM modes at 1550.64 nm, in the WDM case, as a function of received power. At the optimal wavelength, crosstalk for the two OAM modes was -21.4 dB and -20.2 dB, respectively. We can see

that the BER for the mode  $OAM^+$  is slightly better than that for the mode  $OAM^-$  mode, mainly due to differences in alignment of the optical components. At the FEC limit ( $3.8 \times 10^{-3}$  according to the ITU-T Recommendation G.975.1, Appendix I.9, 2004), the average power penalty of mode  $OAM^+$  and  $OAM^-$  for the cases w/o XT, w/ WDM XT and w/ all XT are 1.8 dB, 2.4 dB and 4.55 dB, respectively.

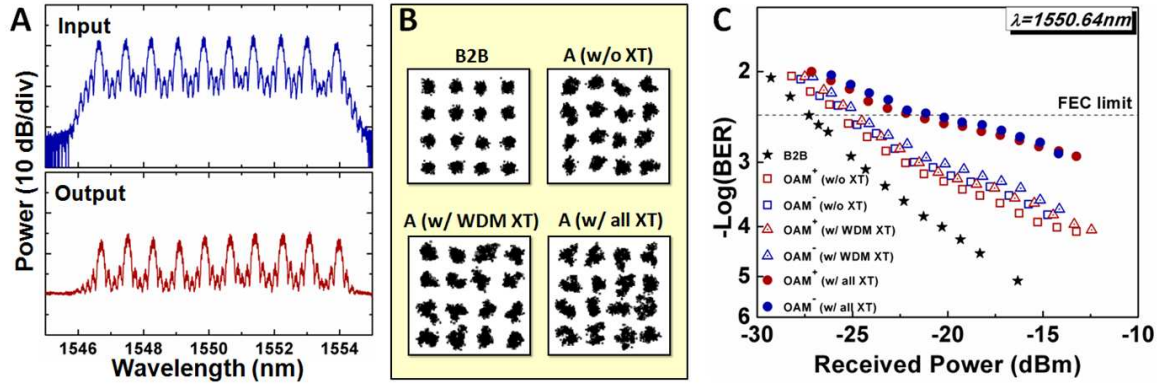


**Figure 7.9:** Additional experimental results of the 2-OAM modes, 10 wavelengths, 16-QAM systems experiments. (A) Spectrum of the modulated signal at the output of the WDM 16-QAM Tx, and spectrum of the  $OAM^+$  mode at the receiver after demultiplexing. (B) Constellations of 16-QAM modulation for the demultiplexed  $OAM^+$  mode at 1550.64 nm, for several cases (without and with crosstalk). (C) BER as a function of received power at 1550.64 nm, for B2B, and OAM modes without and with XT from WDM channels or the other OAM mode.

Despite the higher cross-talk between the two  $OAM^\pm$  modes as we move away from the optimal wavelength, spiral interference patterns were observed throughout the 1540 – 1570 nm wavelength range. Figure 7.10 demonstrates this for the  $OAM^+$  case; for brevity, only a few wavelengths, spaced in 10 pm, 100 pm, 1000 pm and 10 nm steps are shown (as before, a CW-ECL with 100 kHz linewidth and a 60  $\mu$ s camera exposure time was used for this measurement). The  $OAM^+$  mode purity (and hence spiral quality) degrades for some intermediate wavelengths, but the fact that it generally maintains a spiral pattern is indicative of a substantially pure OAM mode over a

30-nm spectral range.

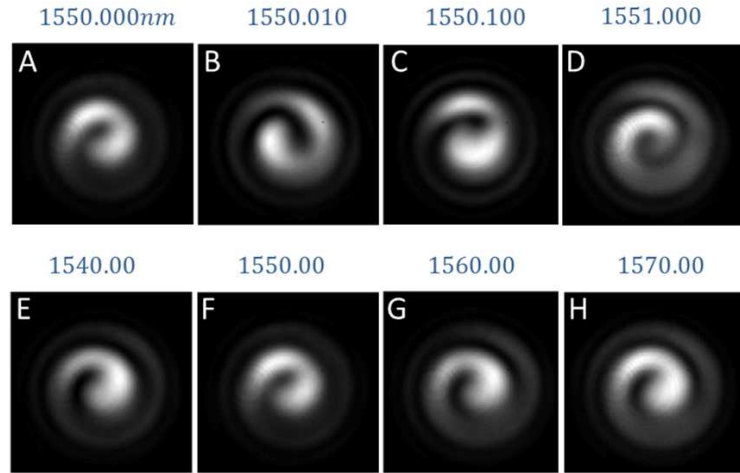


**Figure 7·10:** Spiral interference patterns, showing helical phase, of the  $OAM^+$  mode at different wavelengths for the same vortex fiber conditions (no polarization controller adjustments). **(A-D)** Spiral patterns for the wavelengths spaced in 10pm, 100pm, and 1000pm. **(E-H)** Spirals for the wavelengths spaced in 10nm.

## Chapter 8

# Conclusion

In this dissertation we have studied in detail a new type of fiber, called vortex fibers, that has a potential to increase the capacity of future communication links. We first theoretically studied modes of a MMF with an arbitrary index profile, and proved that a linear combination of vector modes  $HE_{l+1,m}^{even}$  and  $HE_{l+1,m}^{odd}$ , with  $\pi/2$  phase shift among them, poses an OAM of topological charge  $l$ . We identified small effective index separation as the reason for instability of OAM modes in conventional fibers. Numerical methods were used to investigate the mode properties in vortex fibers, showing increase in separation of the effective and group indices in vortex fibers. We have then build a setup using stress-induced microbend gratings to experimentally verify the numerical findings and observed good agreement. Using imaging methods we then qualitatively confirmed that OAM modes are indeed created in vortex fibers by recording their characteristic doughnut-shaped intensity profiles, and spiral-shaped phase profiles.

Next we studied in details three methods for OAM mode generation: one based on stress-induced microbend gratings, second one based on a carbon-dioxide ( $CO_2$ )-laser induced fiber gratings, and the third one based on free-space coupling using liquid-crystal on silicon spatial-light-modulator (LCoS SLM). We have shown that the microbend gratings are significantly polarization sensitive due to stress-induced birefringence but can create OAM modes that are 25dB strong (without tapers) and 35dB strong (with tapers). Setup capable of making  $CO_2$  gratings was built and

results have shown less polarization sensitivity than in the case of microbend gratings. However the generation technique has a limit of creating only 12dB strong OAM modes (without tapers). We also built a setup using SLM as a generation method which is capable of creating 20dB strong OAM modes over tens of nanometers range.

In order to quantitatively measure fiber modal content and hence purity of OAM modes in vortex fibers two methods were developed: the ring method and regression analysis method. Both methods are based on imaging and spatial Fourier analysis of the intensity images. We showed that the OAM states with  $\approx 97\%$  purity can be generated after 20m of vortex fiber, and  $\approx 90\%$  purity after 1km.

To demonstrate that OAM modes supported in vortex fiber can be used for MDM, we have built a 4-mode multiplexing setup based on the SLM mode generation. We have tested the setup for the cross-talk and MPI of the mode-channels as well as sensitivity to alignment, polarization and wavelength.

Finally, we demonstrated a 4-mode OAM-MDM by sending data over the 4-modes of vortex fiber at a single wavelength and at 400Gbit/s, with bit-error-rates below the FEC limit of  $3.8 \times 10^{-3}$ . We used WDM to expand the capacity of the system to 1.6Tbit/s data transmission speed (SE of 1.6 bit/s/Hz). Our results indicate that simple, low-complexity DSP coherent detection methods can be used to achieve 4-mode OAM-MDM. These demonstrations show the potential of OAM-MDM in special types of fibers, and support further investigations of specialty MMFs for future transmission systems.

## 8.1 Observations

In this section we address some of the limitations of the OAM-MDM technique presented in this dissertation, as well as offer some of the ideas for the future investigations regarding vortex fiber and OAM-MDM in general.

*Multiplexing:* Our single wavelength demonstrations on vortex fiber was conducted on 1.1km long fiber using QPSK modulation and 50 GBaud rate. The very first result that was obtained was achieving only 10 GBaud rates, with higher rates resulting in transmission above FEC threshold. This indicates that multiplexing crosstalk is critical in our non-MIMO-based coherent detection. Hence, it is our belief that the multiplexing setup has certain room for improvement.

*Long length:* Experiments on longer lengths could be done though in linear systems, the figure of merit is the bandwidth-distance product, not just one or the other quantity (in our current systems this product was  $1.45\text{Tbit/s/km}$ ).

*Polarization controllers:* In our systems experiment demonstrations, polarization controllers' adjustments were done every hour in order to minimize the cross-talk. This adjustments process is standard in today's advanced digital coherent systems, where the electric fields at the input and the output of the channel are available to DSPs at both transmitter and receiver, which enables the use of arbitrary impairment precompensation and postcompensation algorithms.

*SE:* In our case we have used  $100\text{GHz}$  spectral grid which led to SE of 1.6 bit/s/Hz after 1.1km. A close inspection of Fig. 7.9A, shows that  $50\text{GHz}$  spacing could be potentially used, to double the higher SE. Using more advanced transmitters with individual wavelength channel polarization controls would allow cross-talk to be minimized for each wavelength channel independently, enabling potentially higher bandwidth utilization. However, increase in capacity obtained this way does not increase the SE of our system.

*MIMO:* Because of intensive DSP requirements, no MIMO-based data transmission demonstrations so far have been demonstrated in real time. While large processing power would in principle be possible to enable real time processing, power consumption of such a system would be largely inefficient for today's standards. Just

as a comparison, an estimate of 80W is used for the simplest 2x2 MIMO processing in a commercial, polarization division multiplexed systems (PDM) (Frankel, 2013)<sup>1</sup>. In addition, complexity of MIMO doesn't scale linearly with number of modes. Using simulations Arik et al. have predicted that, per mode, MIMO complexity is a factor 1.4, 1.7, 2.2, 2.8 times higher for number of modes being 6, 12, 20, 30 then for PDM in standard SMF (Arik et al., 2013). Hence, this complexity is additional to the  $N^2$  complexity increase, where N is the number of modes. Another drawback of MIMO could be that it requires very low differential group delay (Ryf et al., 2012), indicating that nonlinear effects might be increased due to increased cross-phase modulation ((Esiambre and Tkach, 2012) p.1050). Nevertheless, MIMO DSP systems are the only MMFs systems, capable of performing high-speed transmission at metro- ( $\sim 10km$ ) and long-haul ( $45 - 70km$ ) lengths today. In order to achieve scaling required in the future, vortex fibers would have to support higher number of modes than 4, and at least 4x4 MIMO within a family of modes need to be considered (Ryf et al., 2012). New generation of fibers that, similarly to the vortex fiber, aim to reduce cross-talk among mode groups is currently active area of research (Gregg et al., 2013).

*Adaptive optics feedback (AOF) methods:* We find the adaptive optics methods (Carpenter et al., 2012) very interesting. One downside of this method is the requirement for a two-dimensional intensity distribution at the fiber output, necessary for feedback. Though not impossible, this approach might require significant atypical requirements from the future systems for it to be deployed (for example a signal would need to be tapped and image onto high speed camera). Though computationally intensive, it would be interesting to quantify how this correction affect the reach. According to (Carpenter et al., 2012), timescale of  $50 \mu m$ , graded index, conventional MMF change is on the order of minute and we expect vortex fiber to be more stable

---

<sup>1</sup>Due to processor cooling, all data centers in the world combined contribute to roughly 0.4% of world's power consumption (Vuckovic, 2013).

in the respect. In addition, MMF used is graded index. Similar results have been obtained for 2km and 8km, promising longer lengths would be possible (Carpenter et al., 2013).

*Reduce slope dispersion:* In Ch. 3, we have found total dispersion (material + waveguide dispersion) to be low in the C-band, however, with the relatively large slope (Fig. 3·7B). A modified version of vortex fiber that will have reduce the slope should be considered for WDM systems to mitigate the dispersion (typical dispersion-shifted fibers are engineered to have total dispersion around 2 to 6 ps/nm/km in the C-band, the zero dispersion being avoided due to enhanced nonlinear effects such as FWM). In addition, we note that the modal dispersion is slightly different and design that will equalize their dispersion should be investigated.

*Loss:* Loss in the vortex fiber of 1.3dB for  $LP_{01}$  is relatively high with respect to conventional fibers, and could affect the SNR of the signal after long length propagation, however, The loss in fibers can be caused by material absorbtion, linear and nonlinear scattering, as well as macrobends and microbends (Smink et al., 2007). In addition, anomalous loss was observed due to high refractive index difference ( $\Delta$ ) in core/cladding regions, and was attributed to draw-induced fluctuations of core radius (Lines et al., 1999). Under certain assumptions, this anomalous loss was theoretically predicted to scale with  $\Delta^2$ . The fact that  $\Delta$  of 0.03 in the vortex fiber is quite large, an order of magnitude larger then in SMFs, supports anomalous loss claim. Nevertheless, it is possible that the current manufacturing vortex fiber method is not optimized.

*Mode dependant loss:* Modal dependant loss (i.e. excess loss) causes impediment in the PDM and MDM systems (Sunnerud et al., 2002). This effect is predicted theoretically and can be explained by mode coupling theory where perturbations have longitudinal spatial frequencies below the range required for mode coupling

(Olshansky and Nolan, 1976). In our case, measured value of 0.3dB (Fig. 3-10) could affect longer fiber length systems. The strategy for loss equalization would need to be addressed in the future, whether through a mode dependant gain or novel fiber design that would reduce the excess loss.

*Spatially and spectrally resolved imaging:* For modal content measurements, we have noticed that interference effects can reveal modes with high sensitivity ( $< -20dB$ ). Our preliminary results using spatially and spectrally resolved technique agree with the cutback measurements, and further data analysis should be done on this front.

*Local area networks and fiber-to-the-home:* It would be interesting to pursue a possible applications of OAM-MDM on a shorter range ( $< 100m$ ) and investigate the bend-sensitivity effects. The potential applications include data centers ethernet cables, where fiber optics cable are becoming dominant due to reduced electromagnetic-interference, higher bandwidth, smaller cost and lightweight in comparison to established twisted pair copper cables.

*Stimulated emission depletion microscopy:* In addition to telecom applications, vortex fiber can find important applications remote delivery of OAM beams such is for stimulated emission depletion microscopy (Hell and Wichmann, 1994), or optical tweezers.

While every technique mentioned here (MCF, MIMO-DSP-MMF, AOF, OAM-MDM) have its pros and cons, the intensive studies are happening on all fronts and future of fiber optical communications is certainly unpredictable.

## Appendix

### A1. Polarization dependence of beamsplitters and mirrors

Polarization dependance of mirrors and beamsplitters can affect the Ring analysis and give erroneous results of mode purity. In this section, we wanted to study polarization dependence of three devices:  $45^\circ$  angled mirror (Thorlabs, BB1-E04), and two beamsplitters (Thorlabs BS015 and Newport 10BC17MB.1).

The setup is shown on Figure 8·1. Light from a single mode fiber is sent through a polarizer and then through the device under test. The polarization is then measured using polarimeter (comprised of a polarizer and a quarter wave plate, and a camera). To determine polarization, four images with certain orientation of a polarimeter are acquired (Berry et al., 1977).

Polarization of the three devices was measured for three different positions of a polarizer: horizontal, vertical and  $45^\circ$  degrees linearly polarized states (results are in the 04/18/2012 folder). Polarization ellipses for certain points clearly indicate that beamsplitters affect the polarization state after reflection (Fig. 8·2).

In particular, a phase delay is introduced between two polarizations in the case of a  $45^\circ$  degrees linearly polarized state ( $\hat{x} + \hat{y}$  state becomes  $\hat{x} + e^{i\Gamma}\hat{y}$ ). Mirror performance was better (Fig. 8·3).

Note that if a polarizer is placed after the beamsplitter, the effect of phase delay won't play such a big role, as the phase delay of a single polarization will not be

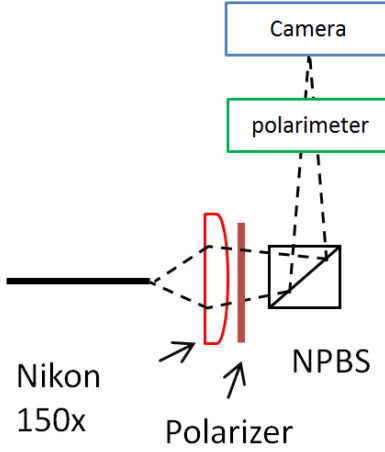


**Figure 8·1:** Setup to measure polarization dependence of a beamsplitter.

detected with the camera. This is to certain extent the case of the Ring analysis setup, hence, I expect that the effect of the polarization dependence play the role only to the certain extent. The results of the Fig. 8·2 could be quantified in needed in the future.

Conclusion is therefore, that for the purposes of the Ring technique, the results of the Ring setup can be trusted.

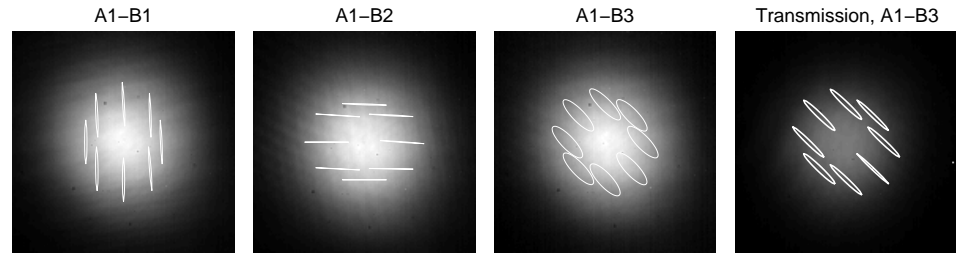


**Figure 8·2:** Sample Newport 10BC17MB.1. Measured polarization after reflection for three different positions of a polarizer: a) horizontal, b) vertical and c)  $45^\circ$  degrees linearly polarized states, as well as after transmission of a  $45^\circ$  degrees linearly polarized state (d). Clearly, phase delay between polarizations is introduced in the case of a  $45^\circ$  degrees linearly polarized state, especially in the reflection case.

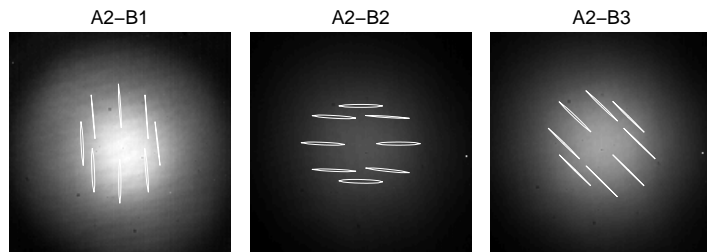


**Figure 8·3:** Polarization after reflection of a  $45^\circ$  angled mirror (Thor-labs, BB1 – E04).

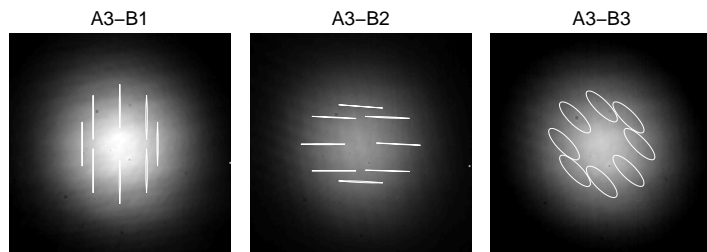


**Figure 8·4:** Polarization after reflection from a beam-splitter (Thor-labs BS015)

## A2. Transmission of OAM-entangled photons

Polarization and time-bin entanglements are well established ways for transmission of the entanglement over long distances (Jennewein et al., 2000; Poppe et al., 2004; Meyer-Scott et al., 2010). We developed a setup to test the hypothesis of whether OAM entangled photon pair can preserve entanglement after kilometer fiber length propagation (Bozinovic et al., 2011c).

Schematic of the entanglement transmission system is shown in Fig. 8.5. To probe the reach of successful entanglement transport when one photon propagates in OAM modes, one channel was replaced with dk11OD100 few-mode vortex fiber. Two polarization-entangled photon pulses were produced (1550nm and 1558nm, 50MHz repetition rate) and launched in the two different channels, (channel A: 1.1 km vortex fiber, channel B: 5km single mode fiber). At the receiving end a complete quantum state tomography is performed.

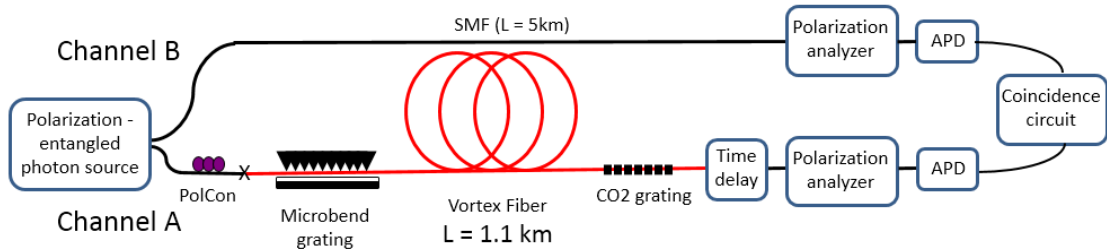


**Figure 8.5:** Schematic of experimental setup. Polarization-entangled photons (1550-nm and 1558-nm) are sent in two different channels A and B. 1.1km long channel A used two gratings to convert between fundamental and OAM mode with > 80% efficiency. Channel B consisted of 5km long single mode fiber (SMF); Time delay was tuned to target coincidence of channel A photons (traveled in a fundamental mode) and channel B photons (traveled in the OAM mode). Full quantum tomography measurement was applied at the receivers' end and density matrix of photon pair was measured.

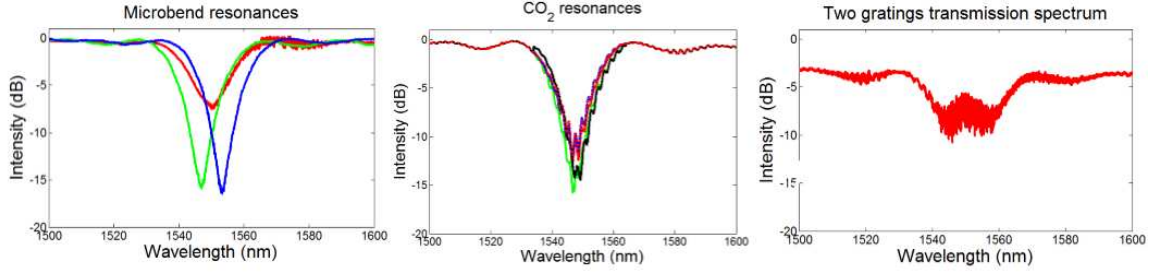


**Figure 8.6:** Resonances for the case of microbend only (right),  $CO_2$  only (center) and both (left).

By measuring the density matrix of the photon pair at the output (Antonelli et al., 2011), we extracted the concurrence of  $C = 0.76$  and the maximally possible S-parameter of  $S = 2.47$ . Since S-parameter satisfies Bell inequality (Gröblacher et al., 2006) (Fig. 8.7), this clearly shows that the photon pair preserves entanglement even after one of the photons has been converted to, a back from, an OAM carrying state.

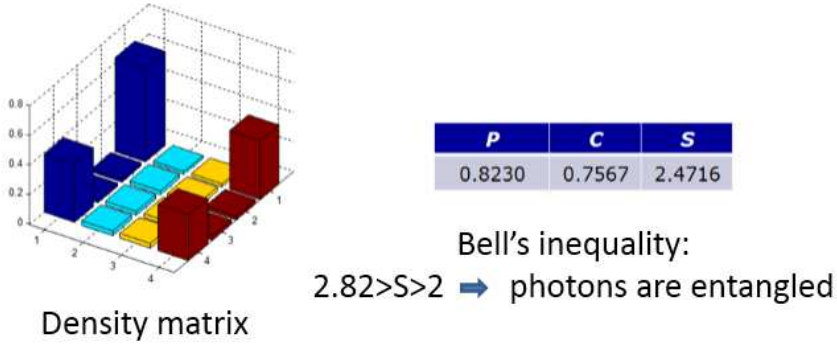


**Figure 8.7:** Measured density matrix, P-parameter, concurrence (C) and S-parameter.

### A3. Publication list

- [1] N. Bozinovic, S. Golowich, P. Kristensen, and S. Ramachandran, "Control of orbital angular momentum of light with optical fibers," *Opt. Lett.* 37, 2451-2453 (2012).
- [2] N. Bozinovic, Y. Yue, Y. Ren, M. Tur, P. Kristensen, A. Willner, and S. Ramachandran, "Orbital Angular Momentum (OAM) Based Mode Division Multiplexing (MDM) over a Km-length Fiber," in European Conference and Exhibition on Optical Communication, OSA Technical Digest (online) (Optical Society of America, 2012), paper Th.3.C.6.
- [3] N. Bozinovic, P. Kristensen, and S. Ramachandran, "Are Orbital Angular Momentum (OAM/Vortex) States of Light Long-Lived in Fibers?," in Frontiers in Optics 2011/Laser Science XXVII, OSA Technical Digest (Optical Society of America, 2011), paper LWL3.
- [4] N. Bozinovic, S. Ramachandran, M. Brodsky, and P. Kristensen, "Record-length transmission of entangled photons with orbital angular momentum (vortices)," in Frontiers in Optics 2011/Laser Science XXVII, OSA Technical Digest (Optical Society of America, 2011), paper PDPB1.
- [5] N. Bozinovic, P. Kristensen, and S. Ramachandran, "Long-range fiber transmission of photons with orbital angular momentum," in CLEO:2011 - Laser Applications to Photonic Applications, OSA Technical Digest (CD) (Optical Society of America, 2011), paper CTuB1.
- [6] N. Bozinovic, C. Ventalon, T. Ford, and J. Mertz, "Fluorescence endomicroscopy with structured illumination," *Opt. Express* 16, 8016-8025 (2008).
- [7] N. Bozinovic, C. Ventalon, T. Ford, and J. Mertz, "Fluorescence Endomi-

croscopy with Out-of-Focus Background Rejection,” in Biomedical Optics, OSA Technical Digest (CD) (Optical Society of America, 2008), paper BTuF57.

[8] Y. Yue, N. Bozinovic, Y. Ren, H. Huang, M. Tur, P. Kristensen, S. Ramachandran, and A. Willner, ”1.6-Tbit/s Muxing, Transmission and Demuxing through 1.1-km of Vortex Fiber Carrying 2 OAM Beams Each with 10 Wavelength Channels,” in Optical Fiber Communication Conference/National Fiber Optic Engineers Conference 2013, OSA Technical Digest (online) (Optical Society of America, 2013), paper OTh4G.2.

[9] S. Golowich, N. Bozinovic, P. Kristensen, and S. Ramachandran, ”Complex mode amplitude measurement for a six-mode optical fiber,” *Opt. Express* 21, 4931-4944 (2013).

[10] S. Golowich, P. Kristensen, N. Bozinovic, P. Gregg, and S. Ramachandran, ”Fibers Supporting Orbital Angular Momentum States for Information Capacity Scaling,” in Frontiers in Optics 2012/Laser Science XXVIII, OSA Technical Digest (online) (Optical Society of America, 2012), paper FW2D.2.

[11] S. Golowich, N. Bozinovic, P. Kristensen, and S. Ramachandran, ”Vortex Fiber Mode Amplitude Estimation,” in Conference on Lasers and Electro-Optics 2012, OSA Technical Digest (online) (Optical Society of America, 2012), paper JTu2K.2.

[12] S. Ramachandran, N. Bozinovic, P. Gregg, S. Golowich, and P. Kristensen, ”Optical vortices in fibres: A new degree of freedom for mode multiplexing,” in European Conference and Exhibition on Optical Communication, OSA Technical Digest (online) (Optical Society of America, 2012), paper Tu.3.F.3.

[13] S. Santos, K. Chu, D. Lim, N. Bozinovic, T. Ford, C. Hourtoule, A. Bartoo, S. Singh, and J. Mertz, ”Optically Sectioned Fluorescence Endomicroscopy with Hybrid-Illumination Imaging through a Flexible Fiber Bundle,” in Advances in Imaging, OSA Technical Digest (CD) (Optical Society of America, 2009), paper NWC3.

## References

- Abrishamian, F., Dragomir, N., and Morishita, K. (2012). Refractive index profile changes caused by arc discharge in long-period fiber gratings fabricated by a point-by-point method. *Applied optics*, 51(34):8271–6.
- Agrawal, G. P. (2010). *Fiber-optic communication systems*. Wiley, 4th edition.
- Allen, L., Beijersbergen, M., Spreeuw, R., and Woerdman, J. (1992). Orbital angular momentum of light and the transformation of Laguerre-Gaussian laser modes. *Physical Review*, 45(11):8185–89.
- Andrews, D. (2008). *Structured Light and Its Applications*. Academic Press.
- Antonelli, C., Shtaif, M., and Brodsky, M. (2011). Sudden Death of Entanglement Induced by Polarization Mode Dispersion. *Physical Review Letters*, 106(8):080404.
- Arik, S., Askarov, D., and Kahn, J. (2013). Effect of mode coupling on signal processing complexity in mode-division multiplexing. *Journal of Lightwave Technology*, 31(3):423–431.
- Barnett, S. M. (2010). Resolution of the Abraham-Minkowski Dilemma. *Physical Review Letters*, 104(7):070401.
- Berdagué, S. and Facq, P. (1982). Mode division multiplexing in optical fibers. *Applied optics*, 21(11):1950–1955.
- Berkhout, G., Lavery, M., Courtial, J., Beijersbergen, M., and Padgett, M. (2010). Efficient Sorting of Orbital Angular Momentum States of Light. *Physical Review Letters*, 105(15):153601.
- Berry, H. G., Gabrielse, G., and Livingston, A. E. (1977). Measurement of the Stokes parameters of light. *Applied optics*, 16(12):3200–3205.
- Beth, R. A. (1936). Mechanical Detection and Measurement of the Angular Momentum of Light. *Physical Review*, 50:115–125.
- Birks, T. and Li, Y. (1992). The shape of fiber tapers. *Journal of Lightwave Technology*, 10(4):432–438.
- Blake, J., Kim, B., and Shaw, H. (1986). Fiber-optic modal coupler using periodic microbending. *Optics letters*, 11(3):177–179.

- Blake, J. N., Kim, B. Y., Engan, H. E., and Shaw, H. J. (1987). Analysis of intermodal coupling in a two-mode fiber with periodic microbends. *Optics letters*, 12(4):281–3.
- Bozinovic, N., Golowich, S., Kristensen, P., and Ramachandran, S. (2012a). Control of orbital angular momentum of light with optical fibers. *Optics Letters*, 37(13):2451–3.
- Bozinovic, N., Kristensen, P., and Ramachandran, S. (2011a). Are Orbital Angular Momentum ( OAM / Vortex ) States of Light Long-Lived in Fibers? In *Frontiers in Optics 2011/Laser Science XXVII, OSA Technical Digest, paper LWL3*.
- Bozinovic, N., Kristensen, P., and Ramachandran, S. (2011b). Long-range fiber-transmission of photons with orbital angular momentum. In *CLEO:2011 - Laser Applications to Photonic Applications, OSA Technical Digest (CD), paper CTuB1*.
- Bozinovic, N., Ramachandran, S., Brodsky, M., and Kristensen, P. (2011c). Record-length transmission of photons entangled in orbital angular momentum ( OAM ). In *Frontiers in Optics 2011/Laser Science XXVII, OSA Technical Digest, paper PDPB1*.
- Bozinovic, N., Yue, Y., Ren, Y., Tur, M., Kristensen, P., Willner, A. E., and Ramachandran, S. (2012b). Orbital Angular Momentum ( OAM ) based Mode Division Multiplexing ( MDM ) over a Km-length Fiber. In *European Conference and Exhibition on Optical Communication, OSA Technical Digest (online), paper Th.3.C.6*.
- Cai, X., Wang, J., Strain, M. J., Johnson-Morris, B., Zhu, J., Sorel, M., O'Brien, J. L., Thompson, M. G., and Yu, S. (2012). Integrated Compact Optical Vortex Beam Emitters. *Science*, 338(6105):363–366.
- Carpenter, J., Thomsen, B. C., and Wilkinson, T. D. (2012). Degenerate Mode-Group Division Multiplexing. *Journal of Lightwave Technology*, 30(24):3946–3952.
- Carpenter, J., Thomsen, B. C., and Wilkinson, T. D. (2013). Optical vortex based Mode Division Multiplexing over graded-index multimode fibre. In *Optical Fiber Communication Conference/National Fiber Optic Engineers Conference 2013, OSA Technical Digest (online), paper OTh4G.3*.
- Carpenter, J. and Wilkinson, T. D. (2012a). All Optical Mode-Multiplexing Using Holography and Multimode Fiber Couplers. *Journal of Lightwave Technology*, 30(12):1978–1984.
- Carpenter, J. and Wilkinson, T. D. (2012b). Holographic Offset Launch for Dynamic Optimization and Characterization of Multimode Fiber Bandwidth. *Journal of Lightwave Technology*, 30(10):1437–1443.

- Chen, H. S., Van Den Boom, H. P. A., and Koonen, A. M. J. (2011). 30-Gb / s 3 x 3 Optical Mode Group-Division- Multiplexing System With Optimized Joint Detection. *IEEE Photonics Technology Letters*, 23(18):1283–1285.
- Curtis, J. E. and Grier, D. G. (2003). Modulated optical vortices. *Optics letters*, 28(11):872–4.
- Dashti, P., Alhassen, F., and Lee, H. (2006). Observation of orbital angular momentum transfer between acoustic and optical vortices in optical fiber. *Physical review letters*, 96(4):043604.
- Davis, D., Gaylord, T., Glytsis, E., Kosinski, S., Mettler, S. C., and Vengsarkar, A. M. (1998). Long-period fibre grating fabrication with focused CO<sub>2</sub> laser pulses. *Electronics Letters*, 34(3):302–303.
- Ebihara, T., Kato, N., Sekura, R., Yamamoto, S., and Yamanaka, J. (1992). Liquid crystal spatial light modulator, US Patent EP0525424B1.
- Erdogan, T. (1997a). Cladding-mode resonances in short- and long-period fiber grating filters. *Journal of the Optical Society of America A*, 14(8):1760–1773.
- Erdogan, T. (1997b). Fiber grating spectra. *Journal of Lightwave Technology*, 15(8):1277–1294.
- Essiambre, R. and Tkach, R. (2012). Capacity Trends and Limits of Optical Communication Networks. *Proceedings of the IEEE*, 100(5):1035–55.
- Essiambre, R.-j., Kramer, G., Winzer, P., Foschini, G. J., and Goebel, B. (2010). Capacity Limits of Optical Fiber Networks. *Journal of Lightwave Technology*, 28(4):662–701.
- Fan, S. and Kahn, J. M. (2005). Principal modes in multimode waveguides. *Optics letters*, 30(2):135–7.
- Foschini, G. J. and Gans, M. J. (1998). On Limits of Wireless Communications in a Fading Environment when Using Multiple Antennas. *Wireless Personal Communications*, 6:311–335.
- Frankel, M. (2013). Technologies That Change the Way Fiber-optic Networks Are Built, talk at Massachusetts Institute of Technology Seminar Series on Optics and Quantum Electronics.
- Freeman, R. L. (2002). *Forward Error Correction*. John Wiley & Sons, Inc., Hoboken, NJ, USA.

- Freund, R., Bunge, C., Ledentsov, N., Molin, D., and Caspar, C. (2010). High-Speed Transmission in Multimode Fibers. *Journal of Lightwave Technology*, 28(4):569–586.
- Friberg, A. T. and Dandliker, R., editors (2008). *Advances in Information Optics and Photonics*. SPIE Press.
- Galtarossa, A., Palmieri, L., Pizzinat, A., Schiano, M., and Tambosso, T. (2000). Measurement of local beat length and differential group delay in installed single-mode fibers. *Journal of Lightwave Technology*, 18(10):1389–1394.
- Garito, A. F., Wang, J., and Gao, R. (1998). Effects of Random Perturbations in Plastic Optical Fibers. *Science*, 281(5379):962–967.
- Gibson, G., Courtial, J., Padgett, M., Vasnetsov, M., Pas'ko, V., Barnett, S., and Franke-Arnold, S. (2004). Free-space information transfer using light beams carrying orbital angular momentum. *Optics Express*, 12(22):5448–56.
- Gloge, D. (1972). Optical Power Flow in Multimode Fibers. *The Bell System Technical Journal*, 51(8):1767–1783.
- Gloge, D. and Marcatili, E. (1973). Multimode Theory of Graded-Core Fibers. *The Bell System Technical Journal*, 52(9):1563–1578.
- Golowich, S., Bozinovic, N., Kristensen, P., and Ramachandran, S. (2013). Complex mode amplitude measurement for a six-mode optical fiber. *Optics Express*, 21(4):4931–4944.
- Golowich, S. and Ramachandran, S. (2005). Impact of fiber design on polarization dependence in microbend gratings. *Optics Express*, 13(18):6870–7.
- Gordon, J. P. and Kogelnik, H. (2000). PMD fundamentals: polarization mode dispersion in optical fibers. *Proceedings of the National Academy of Sciences of the United States of America*, 97(9):4541–50.
- Gregg, P., Kristensen, P., Golowich, S. E., Olsen, J. O., Steinvurzel, P., and Ramachandran, S. (2013). Stable Transmission of 12 OAM States in Air-Core Fiber. *to appear in CLEO:2013 - Laser Applications to Photonic Applications*.
- Gröblacher, S., Jennewein, T., Vaziri, A., Weihs, G., and Zeilinger, A. (2006). Experimental quantum cryptography with qutrits. *New Journal of Physics*, 8(5):75.
- Hamming, R. (1950). Error detecting and error correcting codes. *Bell System technical journal*, XXIX(2):147–160.

- He, H., Heckenberg, N. R., and Rubinsztein-Dunlop, H. (1995). Optical Particle Trapping with Higher-order Doughnut Beams Produced Using High Efficiency Computer Generated Holograms. *Journal of Modern Optics*, 42(1):217–223.
- Hell, S. W. and Wichmann, J. (1994). Breaking the diffraction resolution limit by stimulated emission: stimulated-emission-depletion fluorescence microscopy. *Optics Letters*, 19(11):780–2.
- Hill, K. O., Fujii, Y., Johnson, D. C., and Kawasaki, B. S. (1978). Photosensitivity in optical fiber waveguides: Application to reflection filter fabrication. *Applied Physics Letters*, 32(10):647–649.
- Hill, K. O., Malo, B., Vinberg, K. A., Bilodeau, F., Johnson, D. C., and Skinner, I. (1990). Efficient mode conversion in telecommunication fibre using externally written gratings. *Electronics letters*, 26(16):1270–1272.
- Ho, K.-P. and Kahn, J. M. (2011). Statistics of Group Delays in Multimode Fiber With Strong Mode Coupling. *Journal of Lightwave Technology*, 29(21):3119–3128.
- Ho, K.-P. and Kahn, J. M. (2012). Delay-Spread Distribution for Multimode Fiber With Strong Mode Coupling. *IEEE Photonics Technology Letters*, 24(21):1906–1909.
- Ho, K.-P. and Kahn, J. M. (2013). Mode Coupling and its Impact on Spatially Multiplexed Systems. In Kaminow, I. P., Li, T., and Willner, A. E., editors, *Optical Fiber Telecommunications VI*. Elsevier, Amsterdam.
- Hwang, I. K., Yun, S. H., and Kim, B. Y. (1999). Long-period fiber gratings based on periodic microbends. *Optics Letters*, 24(18):1263–1265.
- Iizuka, K. (2002). *Elements of Photonics Vol II*. Wiley-Interscience.
- Ip, E., Lau, A. P. T., Barros, D. J. F., and Kahn, J. M. (2008). Coherent detection in optical fiber systems. *Optics express*, 16(2):753–91.
- Jackson, J. (1962). *Classical Electrodynamics*. John Wiley & Sons., New York.
- Jennewein, T., Simon, C., Weihs, G., Weinfurter, H., and Zeilinger, A. (2000). Quantum cryptography with entangled photons. *Physical Review Letters*, 84(20):4729–32.
- Kao, K. and Hockham, G. (1966). Dielectric-fibre surface waveguides for optical frequencies. *Electrical Engineers, Proceedings of IEE*, 113(7):1151–1158.
- Karimi, E., Marrucci, L., de Lisio, C., and Santamato, E. (2012). Time-division multiplexing of the orbital angular momentum of light. *Optics letters*, 37(2):127–9.

- Kashyap, R. (2008). *Fiber Bragg Gratings*. Academic Press, 2nd edition.
- Khonina, S. N., Kotlyar, V. V., Shinkaryev, M. V., Soifer, V. A., and Uspleniev, G. V. (1992). The phase rotor filter. *Journal of Modern Optics*, 39(5):1147–1154.
- Kogelnik, H. and Shank, C. V. (1972). Coupled-Wave Theory of Distributed Feed-back Lasers. *Journal of Applied Physics*, 43(5):2327–35.
- Kreysing, M. K., Kießling, T., Fritsch, A., Guck, J. R., and Josef, A. K. (2008). The optical cell rotator. *Optics Express*, 16(21):912–914.
- Ladavac, K. and Grier, D. (2004). Microoptomechanical pumps assembled and driven by holographic optical vortex arrays. *Optics Express*, 12(6):1144–9.
- Lee, B. G., Baks, C., Doany, F. E., Kuchta, D. M., Pepeljugoski, P., and Schow, C. L. (2012). Multicore Fiber Link Demonstrating Large Bandwidth Density for Future Multimode Optical Interconnects. *Proceedings of SPIE, Optoelectronic Integrated Circuits XIV*, 8265:826503.
- Li, Y., Froggatt, M., and Erdogan, T. (2001). Volume current method for analysis of tilted fiber gratings. *Journal of Lightwave Technology*, 21(10):1580–1591.
- Lines, M. E., Reed, W. A., Giovanni, D. J. D., and Hamblin, J. R. (1999). Explanation of anomalous loss in high delta singlemode fibres. *Electronics Letters*, 35(12):1009–1010.
- Mandel, L. and Wolf, E. (1995). *Optical Coherence and Quantum Optics*. Cambridge University Press.
- Marcuse, D. (1974). *Theory of Dielectric Optical Waveguides*. Academic Press.
- Marcuse, D., Chraplyvy, A., and Tkach, R. (1991). Effect of fiber nonlinearity on long-distance transmission. *Journal of Lightwave Technology*, 9(1):121–128.
- Matsumoto, N., Ando, T., Inoue, T., Ohtake, Y., Fukuchi, N., and Hara, T. (2008). Generation of high-quality higher-order Laguerre-Gaussian beams using liquid-crystal-on-silicon spatial light modulators. *Journal of the Optical Society of America. A, Optics, image science, and vision*, 25(7):1642–51.
- McGloin, D., Simpson, N. B., and Padgett, M. J. (1998). Transfer of orbital angular momentum from a stressed fiber-optic waveguide to a light beam. *Applied optics*, 37(3):469–72.
- Meltz, G., Morey, W. W., and Glenn, W. H. (1989). Formation of Bragg gratings in optical fibers by a transverse holographic method. *Optics letters*, 14(15):823–5.

- Meyer-Scott, E., Hubel, H., Fedrizzi, a., Erven, C., Weihs, G., and Jennewein, T. (2010). Quantum entanglement distribution with 810 nm photons through telecom fibers. *Applied Physics Letters*, 97(3):031117.
- Milione, G., Sztul, H., Nolan, D., and Alfano, R. (2011). Higher-Order Poincaré Sphere, Stokes Parameters, and the Angular Momentum of Light. *Physical Review Letters*, 107(5):053601.
- Mizrahi, V. and Sipe, J. (1993). Optical properties of photosensitive fiber phase gratings. *Journal of Lightwave Technology*, 11(10):1513–1517.
- Noe, R., Sandel, D., Hinz, S., Mirvoda, V., Sch, A., Glingener, C., Gottwald, E., Scheerer, C., Fischer, G., Weyrauch, T., Haase, W., Yoshida-Dierolf, M., Schopflin, A., and Gungener, C. (1999). Polarization Mode Dispersion Compensation at 10, 20, and 40 Gb / s with Various Optical Equalizers. *Journal of Lightwave Technology*, 17(9):1602–1616.
- Olshansky, R. (1975). Mode Coupling Effects in Graded-index Optical Fibers. *Applied optics*, 14(4):935–45.
- Olshansky, R. and Nolan, D. A. (1976). Mode-dependent attenuation of optical fibers: excess loss. *Applied optics*, 15(4):1045–1047.
- Padgett, M., J. A., Simpson, N., and Allen, L. (1996). An experiment to observe the intensity and phase structure of LaguerreGaussian laser modes. *American Journal of Physics*, 64(1):77–82.
- Padgett, M. J. and Courtial, J. (1999). Poincaré-sphere equivalent for light beams containing orbital angular momentum. *Optics letters*, 24(7):430–2.
- Panicker, R. A. and Kahn, J. M. (2009). Algorithms for Compensation of Multi-mode Fiber Dispersion Using Adaptive Optics. *Journal of Lightwave Technology*, 27(24):5790–5799.
- Patel, K. M. and Ralph, S. E. (2002). Enhanced Multimode Fiber Link Performance Using a Spatially Resolved Receiver. *IEEE Photonics Technology Letters*, 14(3):393–395.
- Pedersen, E. M., Kristensen, P., Grüner-nielsen, L., and Rottwitt, K. (2011). Impact of the Scalar Approximation on the Prediction of the Group Velocity Dispersion. *Journal of Lightwave Technology*, 29(21):3129–3134.
- Pepeljugoski, P., Golowich, S. E., Ritger, A. J., Kolesar, P., and Risteski, A. (2003). Modeling and Simulation of Next-Generation Multimode Fiber Links. *Journal of Lightwave Technology*, 21(5):1242–1255.

- Petrovich, M. N., Poletti, F., Wooler, J. P., Heidt, A. M., Baddela, N. K., Li, Z., Gray, D. R., Slavík, R., Parmigiani, F., Wheeler, N. V., Hayes, J. R., Numkam, E., Grner-Nielsen, L., Pálsdóttir, B., Phelan, R., Kelly, B., Becker, M., MacSuibhne, N., Zhao, J., Gunning, F. G., Ellis, A. D., Petropoulos, P., Alam, S. U., and Richardson, D. J. (2012). First Demonstration of 2um Data Transmission in a Low-Loss Hollow Core Photonic Bandgap Fiber. In *European Conference and Exhibition on Optical Communication, OSA Technical Digest (online)*, paper Th.3.A.5.
- Poole, C. and Presby, H. (1995). Optical fiber spatial mode converter using periodic core deformation, US Patent 5411566.
- Poole, C. and Wagner, R. (1986). Phenomenological approach to polarisation dispersion in long single-mode fibres. *Electronics Letters*, 22(19):1029–30.
- Poole, C. D., Townsend, C. D., and Nelson, K. (1990). Resonant-helix two-mode fiber notch filter. In *Optical Fiber Communication Conference, OSA Technical Digest*, paper TUG2. Optical Society of America.
- Poppe, A., Fedrizzi, A., Ursin, R., Böhm, H., Lörunser, T., Maurhardt, O., Peev, M., Suda, M., Kurtsiefer, C., Weinfurter, H., Jennewein, T., and Zeilinger, A. (2004). Practical quantum key distribution with polarization entangled photons. *Optics Express*, 12(16):3865–71.
- Poynting, J. (1909). The wave motion of a revolving shaft, and a suggestion as to the angular momentum in a beam of circularly polarised light. *Proceedings of the Royal Society of London, Series A*(82):560–567.
- Raddatz, L., White, I., Cunningham, D., and Nowell, M. (1998). An experimental and theoretical study of the offset launch technique for the enhancement of the bandwidth of multimode fiber links. *Journal of Lightwave Technology*, 16(3):324–331.
- Ramachandran, S. (2005). Dispersion-tailored few-mode fibers: a versatile platform for in-fiber photonic devices. *Journal of Lightwave Technology*, 23(11):3426–3443.
- Ramachandran, S., Fini, J., Mermelstein, M., Nicholson, J., Ghalmi, S., and Yan, M. (2008). Ultra-large effective-area, higher-order mode fibers: a new strategy for high-power lasers. *Laser & Photonics Review*, 2(6):429–448.
- Ramachandran, S., Kristensen, P., and Yan, M. F. (2009). Generation and propagation of radially polarized beams in optical fibers. *Optics Letters*, 34(16):2525–7.
- Ramachandran, S., Nicholson, J., Ghalmi, S., and Yan, M. (2003). Measurement of multipath interference in the coherent crosstalk regime. *IEEE Photonics Technology Letters*, 15(8):1171–1173.

- Randel, S., Ryf, R., Sierra, A., Winzer, P. J., Gnauck, A. H., Bolle, C. A., Peckham, D. W., Mccurdy, A., and Lingle, R. J. (2011). 6x56-Gb/s mode-division multiplexed transmission over 33-km few-mode fiber enabled by 6x6 MIMO equalization. *Optics Express*, 19(17):16697–16707.
- Richardson, D. J. (2010). Filling the Light Pipe. *Science*, 330(6002):327–328.
- Rogers, A. (2008). *Polarization in Optical Fibers*. Artech House, Inc., Boston; London.
- Ryf, R., Randel, S., Gnauck, A. H., Bolle, C., Sierra, A., Member, S., Mumtaz, S., Esmaeelpour, M., Burrows, E. C., Essiambre, R.-j., Winzer, P. J., Peckham, D. W., Mccurdy, A. H., and Lingle, R. (2012). Mode-Division Multiplexing Over 96 km of Few-Mode Fiber Using Coherent 6x6 MIMO Processing. *Journal of Lightwave Technology*, 30(4):521–531.
- Sakaguchi, J., Awaji, Y., Wada, N., Kanno, A., Kawanishi, T., Hayashi, T., Taru, T., Kobayashi, T., and Watanabe, M. (2012). Space Division Multiplexed Transmission of 109-Tb/s Data Signals Using Homogeneous Seven-Core Fiber. *Journal of Lightwave Technology*, 30(4):658–665.
- Saleh, B. and Teich, M. (2007). *Fundamentals of Photonics*. Wiley-Interscience, Hoboken, N.J., 2nd edition.
- Salsi, M., Koebele, C., Sperti, D., Tran, P., Mardoyan, H., Brindel, P., Bigo, S., Boutin, A., Verluise, F., Sillard, P., Bigot-astruc, M., Provost, L., and Charlet, G. (2012). Mode-Division Multiplexing of 2x100 Gb / s Channels Using an LCOS-Based Spatial Modulator. *Journal of Lightwave Technology*, 30(4):618–623.
- Savin, S., Digonnet, M. J., Kino, G. S., and Shaw, H. J. (2000). Tunable mechanically induced long-period fiber gratings. *Optics letters*, 25(10):710–2.
- Schmitz, C. H. J., Uhrig, K., Spatz, J. P., and Curtis, J. E. (2006). Tuning the orbital angular momentum in optical vortex beams. *Optics express*, 14(15):6604–12.
- Shannon, C. (1948). A mathematical theory of communication. *The Bell System Technical Journal*, 27(July, October):379–423, 623–656.
- Shemirani, M. and Kahn, J. (2009). Higher-Order Modal Dispersion in Graded-Index Multimode Fiber. *Journal of Lightwave Technology*, 27(23):5461–5468.
- Shemirani, M. B., Mao, W., Panicker, R. A., and Kahn, J. M. (2009). Principal Modes in Graded-Index Multimode Fiber in Presence of Spatial- and Polarization-Mode Coupling. *Journal of Lightwave Technology*, 27(10):1248–1261.

- Sleiffer, V. A. J. M., Jung, Y., Veljanovski, V., Uden, R. G. H. V., Kuschnerov, M., Inan, B., Nielsen, L. G., Sun, Y., Richardson, D. J., Alam, S. U., Poletti, F., Sahu, J. K., Dhar, A., Koonen, A. M. J., Corbett, B., Winfield, R., Ellis, A. D., and Waardt, H. D. (2012). 73.7 Tb/s (96x3x256-Gb/s) moe-division-multiplexed DP-16QAM transmission with inline MM-EDFA. *Optics Express*, 20(26):B428–B438.
- Smink, R., de Hon, B., and Tijhuis, A. (2007). Bending loss in optical fibers a full-wave approach. *Journal Of The Optical Society Of America B Optical Physics*, 24(10):2610–2618.
- Smith, A. M. (1980). Birefringence induced by bends and twists in single-mode optical fiber. *Applied optics*, 19(15):2606–11.
- Snyder, A. and Love, J. (1983). *Optical Waveguide Theory*. Chapman and Hall, London; New York.
- Stuart, H. R. (2000). Dispersive Multiplexing in Multimode Optical Fiber. *Science*, 289(5477):281–283.
- Su, T., Scott, R. P., Djordjevic, S. S., Fontaine, N. K., Geisler, D. J., Cai, X., and Yoo, S. J. B. (2012). Demonstration of free space coherent optical communication using integrated silicon photonic orbital angular momentum devices. *Optics Express*, 20(9):9396–402.
- Sullivan, M. N. O., Mirhosseini, M., Malik, M., and Boyd, R. W. (2012). Near-perfect sorting of orbital angular momentum and angular position states of light. *Optics Express*, 20(22):24444–24449.
- Sunnerud, H., Xie, C., Karlsson, M., Samuelsson, R., and Andrekson, P. A. (2002). A Comparison Between Different PMD Compensation Techniques. *Journal of Lightwave Technology*, 20(3):368–378.
- Tabosa, J. and Petrov, D. (1999). Optical Pumping of Orbital Angular Momentum of Light in Cold Cesium Atoms. *Physical Review Letters*, 83(24):4967–4970.
- Takara, H., Sano, A., Kobayashi, T., Kubota, H., Kawakami, H., Matsuura, A., Miyamoto, Y., Abe, Y., Ono, H., Shikama, K., Goto, Y., Tsujikawa, K., Sasaki, Y., Ishida, I., Takenaga, K., Matsuo, S., Saitoh, K., Koshiba, M., and Morioka, T. (2012). 1.01-Pb/s (12 SDM/222 WDM/456 Gb/s) Crosstalk-managed Transmission with 91.4-b/s/Hz Aggregate Spectral Efficiency. In *in European Conference and Exhibition on Optical Communication, OSA Technical Digest (online)*, paper Th.3.C.1.
- Vengsarkar, A. M., Lemaire, P. J., Judkins, J. B., Bhatia, V., Erdogan, T., and Sipe, J. E. (1996). Long-Period Fiber Gratings as Band Rejection Filters. *Journal of Lightwave Technology*, 14(1):58–65.

- Volpe, G. and Petrov, D. (2004). Generation of cylindrical vector beams with few-mode fibers excited by Laguerre-Gaussian beams. *Optics Communications*, 237(1-3):89–95.
- Vuckovic, J. (2013). ”Optical Nanocavities with Quantum Dots: From Nano-lasers to Bio-probes” seminar, Massachusetts Institute of Technology Seminar Series on Optics and Quantum Electronics.
- Wang, J., Yang, J.-y., Fazal, I. M., Ahmed, N., Yan, Y., Huang, H., Ren, Y., Yue, Y., Dolinar, S., Tur, M., and Willner, A. E. (2012). Terabit free-space data transmission employing orbital angular momentum multiplexing. *Nature Photonics*, 6:488–496.
- Wang, X., Nie, Q., Xu, T., and Liu, L. (2006). A Review of the Fabrication of Optic Fiber. *Proceedings of SPIE, International Commission for Optics ICO20: Optical Design and Fabrication*, 6034:60341D.
- Watson, G. (1995). *A Treatise on the Theory of Bessel Functions*. Cambridge University Press, Cambridge.
- Winzer, P. (2010). Beyond 100G Ethernet. *IEEE Communications Magazine*, 48(July):26–30.
- Winzer, P. and Essiambre, R. (2006). Advanced optical modulation formats. *Proceedings of the IEEE*, 94(5):952–985.
- Wong, G. K. L., Kang, M. S., Lee, H. W., Biancalana, F., Conti, C., Weiss, T., and Russell, P. S. J. (2012). Excitation of Orbital Angular Momentum Resonances in Helically Twisted Photonic Crystal Fiber. *Science*, 337(6093):446–449.
- Yao, A. M. and Padgett, M. J. (2011). Orbital angular momentum: origins, behavior and applications. *Advances in Optics and Photonics*, 3(2):161–204.
- Yue, Y., Bozinovic, N., Ren, Y., Huang, H., Tur, M., Kristensen, P., Ramachandran, S., and Willner, A. E. (2013). 1.6-Tbit/s Muxing, Transmission and Demuxing through 1.1-km of Vortex Fiber Carrying 2 OAM Beams Each with 10 Wavelength Channels. In *Optical Fiber Communication Conference/National Fiber Optic Engineers Conference 2013, OSA Technical Digest (online)*, paper OTh4G.2.

# CURRICULUM VITAE

**Nenad Božinović**

20 Chestnut St Apt 404, Cambridge, MA, 02139,  
+1-650-391-6600,  
nesa@bu.edu, www.nenadbozinovic.com

## EDUCATION

- May 2013 Ph.D. in Electrical and Computer Engineering, Boston University
- May 2007 M.Sc. in Electrical and Computer Engineering, Boston University, GPA: 3.61/4.0
- July 2004 B.Sc. in Physics, Belgrade University, Serbia, GPA: 9.6/10.0

## AWARDS AND HONORS

- 2012 Top 20 downloaded paper of major optics journals (Advances in Optics and Photonics, JOSA B and Optics Letters) over the past two years.
- 2011 Boston University President's award for a top project among 100+ graduate-level projects
- 2006 - 2010 Studenica Foundation Fellowship
- 1998 - 2004 Serbian Ministry of Education Fellowship

## RESEARCH AND WORK EXPERIENCE

03/2010 - Present **Research Assistant**, Boston University, Nanostructured Fibers and Nonlinear Optics Lab, Prof. Ramachandran Group

- Designed and developed system with potential for 400% throughput gain over existing commercial fibers (collaboration with OFS Labs and USC)
- Developed modal characterization method for few-mode fibers (collaboration with MIT Lincoln Laboratories)
- Demonstrated transmission of orbital angular momentum entangled photon pair over kilometer length fiber (collaboration with AT&T Labs)

05/2006 - 03/2010      **Research Assistant**, Boston University, Biomicroscopy Lab

- Developed novel real-time, GPU-enabled, high-resolution microscopy technique that eliminates need for biopsies (prototype is currently used at Boston Medical Center)

05/2008 - 09/2008      **Internship**, Cambridge Research and Instrumentation Inc. (now PerkinElmer)

- Identified new mouse brain imaging feature for DyCE Maestro, a company's flagship product for cancer research, by improving core image processing algorithms.

## SKILLS

- Fiber optics: Design, simulation, development and characterization of specialty fibers and fiber devices
- Optics: Design and development of large (100+ components) opto-mechanical-imaging systems
- Imaging: CCD cameras, LCoS SLMs, MEMS, microscopy, image processing, visualization
- Optical Networks: Bit-error-rate testing; proficiency in optical components and modulation formats
- Computer Networks: Ethernet, TCP/IP, HTTP protocols
- Programming: MATLAB, LabVIEW, C++/CUDA, COMSOL
- Hardware: LabVIEW automation: GPIB, USB, RS232 protocols
- Team-work: Coordinated research collaborations with MIT Lincoln Labs, AT&T Labs and USC
- Writing and presentation: Published 12 refereed papers; maximum presentation attendance 400+

## PROFESSIONAL AND SOCIAL ACTIVITIES

- Reviewer for Optics Letters, Optics Express and IEEE Photonics Technology Letters journals
- Teaching assistant for "Introduction to Semiconductor Physics" and "Introduction to Software Engineering"
- Boston University Waterpolo Team, 2008 and 2009
- Intramural sports: BU Tennis semi-finalist (2011); BU Soccer, Softball and Football team member